THE DEVELOPMENT OF SUPERRESOLUTION SPECTROSCOPIC TECHNIQUES AND CHARACTERIZATION OF MICROSCALE EXCITON DIFFUSION IN ORGANIC SEMICONDUCTING POLYMERS

by

Eric Stephen Massaro

A dissertation submitted in partial fulfillment
of the requirements for the degree

of

Doctor of Philosophy

in

Chemistry

MONTANA STATE UNIVERSITY
Bozeman, Montana

July 2018

DEDICATION

This dissertation is dedicated to:

God: You have lead me to this point: “A man’s heart plans his way, But the Lord directs his steps.” (Proverbs 16:9). You have made this all possible: “With men this is impossible, but with God all things are possible.” (Matthew 19:26). You have called me to far greater things than this document or anything else in this world:“I press toward the goal for the prize of the upward call of God in Christ Jesus.” (Philippians 3:14). Thank you for saving me from my sin even while I wallow in it all too often: “God demonstrates His own love toward us, in that while we were still sinners, Christ died for us. (Romans 5:8).

Camille: You perfectly complement me in every way that you were designed to. You consistently give me reason to be the man that you and our children deserve. Thank you for always believing in me, challenging me, and supporting me with selfless, Christ-like love.

Eliza: You will only remember these days through the stories we tell you. Little do you know, your smile, laugh, and presence raised my spirits more times than I can count.

My Son: Your soon arrival spurs me on to become a man worthy of a son.

My Parents: Always encouraging me and pushing me to be my best brought me to where I am today. Thank you for demonstrating your faith, instilling your personal convictions, and selflessly raising me.

ACKNOWLEDGEMENTS

I am enormously grateful to so many individuals in my life. Above all, my Lord and Savior Jesus Christ who makes this all possible. Secondly, my beautiful wife Camille and our incredible children who have been constant sources of support and perspective throughout the last 4 years. Finally, my parents, immediate and extended family, as well as my family through marriage, who have all played a hand in molding me into the person I am today.

Throughout the years countless individuals have given of their time, energy, and patience in the pursuit of my education. From elementary school to college and beyond, talented educators have poured into me knowledge from their lifetime of learning. Most importantly, Erik Grumstrup has provided invaluable support and guidance toward the advancement of my professional development, technical knowledge, and scientific intuition. I also owe a significant amount of gratitude to my committee members: Rob Walker, Aleks Rebane, and Rufus Cone for teaching and challenging me along the way. Finally, thank you to all the members of the Grumstrup Group.

TABLE OF CONTENTS

TABLE OF CONTENTS CONTINUED

TABLE OF CONTENTS CONTINUED

LIST OF FIGURES

Figure Page

LIST OF FIGURES CONTINUED

Figure Page

LIST OF FIGURES CONTINUED

Figure Page

ABSTRACT

Disordered semiconducting materials offer cost effective, solution processable alternatives to highly crystalline semiconducting materials for utilization in a variety of optoelectronic devices. However, characterization of these complex materials systems using bulk spectroscopic methods is heavily influenced by chemical and morphological heterogeneity inherent to the material. The experiments described in this thesis are designed to improve the fundamental understanding of the photophysical processes in disordered solution processed semiconducting materials by developing and utilizing high spatial resolution spectroscopic methods.

Chapters 2-4 will outline the experimental and theoretical development of two superresolution spectroscopic techniques. First (chapters 2 & 3), structured pump-probe microscopy (SPPM) utilizes a structured excitation profile along with a diffraction limited probe pulse to achieve ~100 nm spatial resolution. Using SPPM it is also possible to collect time resolved spectroscopic data from a sub-diffraction limited volume. Second (chapter 4), label-free saturated structured excitation microscopy (LF-SSEM) is theoretically developed. LF-SSEM is experimentally similar to SPPM but exploits the saturation of the absorption process to achieve even greater resolution enhancement. Here, simulated LF-SSEM is shown to achieve ~33 nm spatial resolution.

Chapter 5 demonstrates the utilization of PPM to investigate exciton transport in the organic semiconducting polymer (OSP), poly [N-9’’-hepta-decanyl-2,7-carbazole-alt-5,5-(4’,7’-di-2-thienyl-2’,1’,3’-benzothiadiazole)] (PCDTBT). Although OSPs have shown great promise for use in a variety of optoelectronic applications, much remains unknown about their excited state dynamics. The data reported here represents a significant contribution to the rapidly growing wealth of knowledge pertaining to OSP systems. Specifically, the microscale exciton diffusivity observed in PCDTBT thin films using PPM is found to reach 3.2 cm^2/s.

Chapter 6 examines a technique in the early stages of development and optimization that is able to detect excited state carrier diffusion with increased sensitivity and accuracy compared to PPM. Differential detection pump-probe microscopy (DDPPM) uses two probe pulses to selectively eliminate the signal of carriers that have not diffused beyond the boundaries of the initial excitation.

The experiments described within this dissertation are diverse, yet the common goal is to increase and improve the knowledge of photophysical properties in disordered semiconducting materials. This goal takes two forms in the development of novel spectroscopic methodology and the characterization of complex materials using PPM. The singular result is the advancement of basic science pertaining to complex semiconducting materials systems.

CHAPTER ONE

INTRODUCTION

1.1 Motivation

The integration of semiconducting materials into every day devices such as cell phones, computers, cameras, etc. has pushed the limits of basic research and development to meet industrial, research, and consumer demands. Traditionally, high quality, single crystal inorganic semiconductors have been used for these applications despite the high cost of fabrication [1]. However, a separate class of semiconductors termed disordered semiconductors, shows great promise as low-cost alternatives to current technology. Examples of disordered semiconductors include polycrystalline inorganic/organic materials, as well as amorphous organic materials, both of which are often solution processed [2-4]. While promising from the standpoint of low fabrication cost, the complex physical and chemical morphology of disordered semiconductors, as suggested by their name, complicates the characterization of their electronic properties when using spectroscopic techniques that average over a large surface area. Therefore, the performance of disordered semiconductor-based devices is often limited by the incomplete understanding of the materials photophysical parameters. This thesis outlines work toward understanding the role of morphology on the transport properties in organic polymer thin films, a type of disordered semiconductor, and the development of novel superresolution spectroscopic methods that can be used to deconvolve the effects of physical and chemical morphology from photophysical dynamics.

The types of spatial heterogeneities that complicate disordered semiconductors include point defects and grain boundaries, as well as morphological and chemical variations [5]. These heterogeneities can occur on the same nanometer length scales as excited state diffusion, trapping mechanisms, and scattering. As a result, bulk spectroscopic data will convolve together the effects of both sample heterogeneity and the inherent photophysics of the material. Therefore, as the demand for nanoscale semiconductor-based devices increases, it becomes necessary to develop and utilize spectroscopic techniques capable of accurately characterizing excited state dynamics across length scales free (or with reduced effects) of spatial heterogeneity.

The technique primarily used in this thesis is pump-probe microscopy (PPM). PPM is an ultrafast, label-free spectroscopic method capable of directly observing excited state dynamics on length scales restricted by the diffraction limit of light [6-9]. This thesis outlines efforts designed to develop spectroscopic techniques that can go beyond the capabilities of PPM by surpassing the diffraction limit of light (chapters 2 - 4) [10-16]. The techniques developed here are strongly influenced by fluorescence based superresolution techniques that earned the Nobel Prize in Chemistry (2014), but are modified to allow imaging of non-fluorescent materials with ultrafast temporal resolution [17-22]. Similarly, chapter 6 describes the development of a technique that provides increased sensitivity to excited state diffusion compared with current PPM technology. The three novel techniques described within this thesis (chapters 2-4, 6) represent significant contributions to the nanoscale research community and provide unique methodologies that are well suited to study complex, nanoscale, heterogeneous materials systems.

Optoelectronic devices, specifically photovoltaics, are traditionally designed around high quality, crystalline, inorganic semiconductors such as silicon, gallium arsenide, or cadmium telluride [23]. Polycrystalline and organic semiconductors represent viable alternatives to inorganic semiconductors and are also solution processable, cost effective, and environmentally friendly [24]. Specifically, organic semiconducting polymers (OSPs) show promising potential for applications including organic field-effect transistors, light emitting diodes, and photovoltaics [2, 25-29]. However, the fundamental photophysical processes that determine the effectiveness of OSPs are not well understood. In chapter 5 PPM is used to characterize the excited state dynamics of poly [N-9’’-hepta-decanyl-2,7-carbazole-alt-5,5-(4’,7’-di-2-thienyl-2’,1’,3’-benzothiadiazole)] (PCDTBT). As a result, exceptionally high rates of exciton diffusivity are reported that can be attributed, in part, to microscale regions of self-organized polymer chains. These microscale regions consist of highly conjugated networks that result in long range delocalization and increased transport of photoexcited species. The diffraction limited spatial resolution (~200 nm) of PPM reduces the spatial heterogeneity of the amorphous polymer region that is probed, consequently revealing photophysical phenomena that are typically averaged over in ensemble measurements.

The work described in this dissertation has yielded both novel spectroscopic methodology and a description of the excited state dynamics in complex organic semiconducting polymers to the nanoscale research community. The remainder of chapter 1 will describe the experimental details of PPM, as well as necessary background information with

respect to superresolution spectroscopy and organic semiconductor photophysics to support the content of subsequent chapters.

1.2 Pump-Probe Microscopy

PPM is a vital spectroscopic tool for the characterization of complex materials systems. The combination of femtosecond temporal resolution and diffraction limited spatial resolution allows for the direct correlation of material morphology and excited state dynamics while reducing the contributions of microscale chemical and morphological heterogeneities that are averaged over with traditional bulk spectroscopic techniques [7-9]. PPM utilizes two laser pulses; the pump pulse, which creates an excited state population and the probe pulse which is used to observe the temporal and spatial evolution of the excited state population. In a transmissive geometry, the nonlinear material response manifests as a pump dependent transient change in the transmitted probe light. Depending on the transient spectrum of the material at specific pump and probe wavelengths, three transient responses may contribute to the observed signal; Stimulated Emission (SE), Ground State Bleach (GSB), and Transient Absorption (TA) [30]. Figure 1.1 shows the energy level diagram descriptions of these three responses. Most notably, SE and GSB result in increased transmission of the probe pulse due to photoexcitation while TA results in reduced transmission of the probe pulse following photoexcitation.

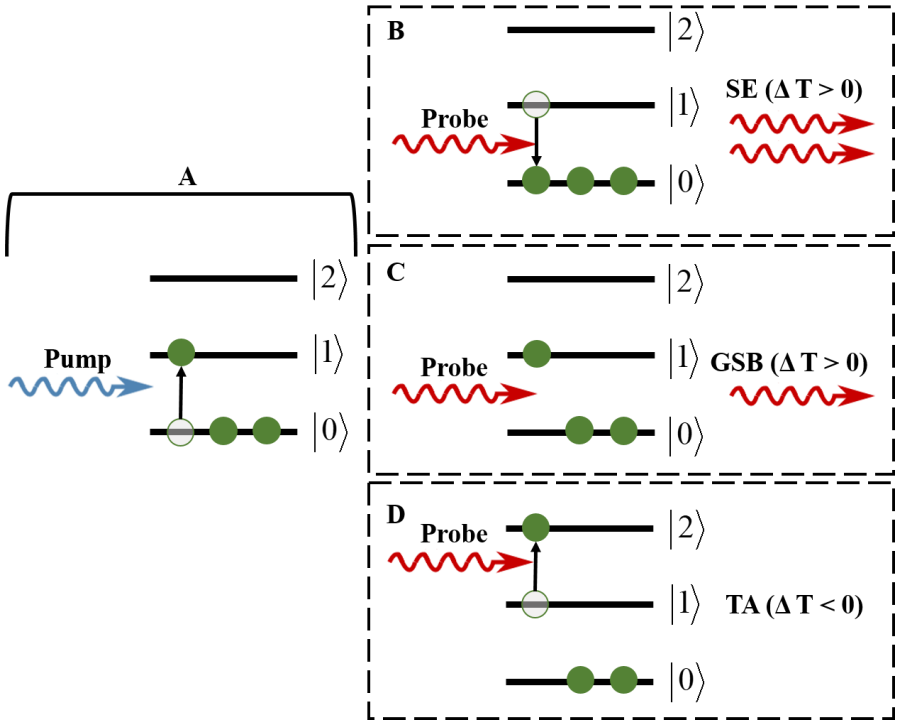

Figure 1.1. Three level description of the transient response in transmissive PPM experiments. (A) The pump pulse initially promotes an excited state population. (B) SE is a result of the excited state returning to the ground state by emitting a photon coherent with the incident probe pulse. (C) GSB is due to the reduced ground state absorption of the probe pulse. Both SE and GSB represent an increase in the transmitted probe pulse ($\Delta T > 0$) and are therefore indistinguishable without further spectroscopic knowledge of the system. (D) TA is the absorption of the probe pulse by the excited state population resulting in decreased transmission of the probe pulse ($\Delta T < 0$).

Panel A of Fig. 1.2 shows the basic schematic of the home-built pump-probe microscope used in the experiments described in this thesis. A Ti:Sapphire laser is used in coordination with various optomechanical components to spatially and temporally vary the pump and probe pulses. Leveraging the material dependent transient responses described in Fig. 1.1, PPM provides three methods of data collection. These three methods, termed spatially correlated imaging, excited state kinetics, and spatially separated imaging, are

discussed below and shown in panels B, C, and D of Fig. 1.2. Each of these three methods provides unique information regarding the excited state dynamics in diffraction limited volumes of complex materials systems.

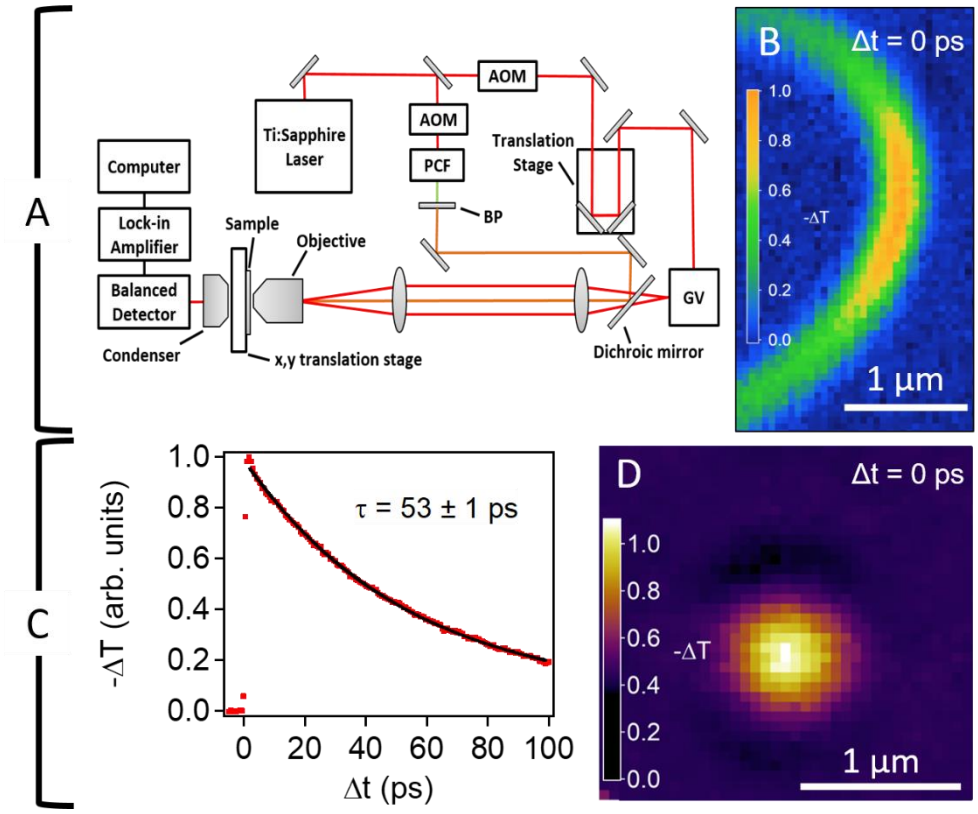

Figure 1.2. Overview of PPM. (A) Schematic of the PPM experiment. The output of a Ti:Sapphire laser (80 MHz, 800 nm, 100 fs) produces both pump and probe pulses. Both pump and probe arms are directed toward acoustooptic modulators (AOM). The probe beam is directed to both a computer controllable delay stage and a set of galvanometer (GV) mirrors in order to control the spatial and temporal position relative to the pump. The pump is directed to a photonic crystal fiber (PCF to vary the excitation wavelength. The pump and probe pulses are then recombined prior to a 4-f lens system and collinearly directed into the back aperture of a microscope objective (100x, 0.9 NA). (B) Spatially overlapped image of a silicon nanowire. (C) Excited state kinetics of free carriers in a silicon nanowire. (D) Spatially separated image of charge carrier density (Δt = 0 ps) following photoexcitation of a silicon nanowire.

1.2.1 Spatially Overlapped Imaging

PPM can be used to collect wide field images of a material's transient response by spatially overlapping the pump and probe pulses on the sample surface. The sample can then be raster scanned behind this pump-probe field to produce an image of the material's transient response at specific pump-probe delay times (Δt). The transient signal can manifest as any of the three processes described in Fig. 1.1, while the signal magnitude is proportional to the number of photoexcited states [31]. Panel B of Fig. 1.2 shows an example of the spatially overlapped imaging performed on a silicon nanowire when Δt = 0 ps. Due to the nanoscale dimensions of the silicon nanowire (100 nm diameter), the image in panel B also provides information about the spatial resolution of the imaging system. When the imaged object is well below the diffraction limit of light (<< 200 nm) it can be treated as a delta function. As a result, the horizontal cross section at the maximum pump-probe signal in panel B is representative of the optical system point spread function (PSF). The specifics of image resolution will be discussed in more detail within chapters 2-4.

1.2.2 Excited State Kinetics

Characterizing the relaxation mechanisms of the excited state using PPM is performed by spatially overlapping the pump and probe beams while varying the pump-probe delay time. The time dependent decrease in excited state population can be fit with various decay functions (sum of exponentials, power law, etc…) to identify potential relaxation pathways [32]. An example of excited state kinetics is shown in panel C of Fig. 1.2 where the excited state decay of free carriers in a silicon nanowire is fit with a single exponential and the excited state lifetime is 53 ps. As discussed above, the spatial resolution of this

experiment is defined by the PSF of the optical system which remains diffraction limited. However, experiments and modeling results presented in chapters 2 and 3 will demonstrate the possibility of collecting time dependent spectroscopic information from a sub-diffraction limited volume of the sample.

1.2.3 Spatially Separated Imaging

Spatially separated imaging is performed by holding the pump pulse in a constant location on the sample and scanning the probe pulse over the localized excitation at a series of increasing pump-probe delay times (Δt). An example of a spatially separated image is shown in panel D of Fig. 1.2 where Δt = 0 ps. The purpose of spatially separated imaging is to extract the rate with which excited state species diffuse through the material. Diffusive motion can be described by

$$\frac{dN}{dt} = D_c \nabla^2 N - \frac{N}{\tau} \tag{1.1}$$

where N is the concentration of excited states, D_c is the diffusion constant of the material, ∇ is the Laplace operator, and τ is the excited state lifetime [33]. The photoexcited species will diffuse from areas of high concentration to regions of lower excited state concentration. Therefore, the spatially separated image distributions will broaden as Δt increases. The time dependent distribution of the excited state population can be described by the double convolution of the pump and probe beam spatial coordinates and the linear diffusion equation [34]. Under the assumption that both the pump and probe beam profiles are Gaussian and that there is no excited state decay, the one-dimensional time dependent spatially separated image ($G(t)$) can be defined by

$$G(t) = Exp\left[\frac{-4(x)^2 \ln(2)}{\gamma_1}\right] \otimes Exp\left[\frac{-4(x)^2 \ln(2)}{\gamma_2}\right] \otimes Exp\left[\frac{-(x)^2}{4\pi D_c t}\right] = Exp\left[\frac{-4(x)^2 \ln(2)}{\gamma_1^2 + \gamma_2^2 + 16\ln(2)\pi D_c t}\right] \quad (1.2)$$

where γ_1 and γ_2 are the full width at half maximums (fwhms) of the pump and probe beams, respectively, and D_c is the local diffusion constant. Integrating multiple spatially separated images collected at increasing pump-probe delay times along either the x or y axes produces a series of time dependent excited state distribution profiles. Each profile can be fit with a Gaussian function whose time dependent fwhm, $\beta(\Delta t)$, is given by,

$$\beta(\Delta t) = \left[\beta(t_0)^2 + 16\ln(2) D_c \left(\Delta t - t_0\right)\right]^{1/2}. \quad (1.3)$$

Here $\beta(t_0)^2$ is the square of the fwhm when $\Delta t = t_0 =$ 0 ps (the maximum of the transient signal where $\beta(t_0) = \gamma_1 + \gamma_2$) which eliminates the contribution of γ_1 and γ_2 from Eq. 1.2 [35, 36]. This technique will be described in more detail in chapter 5 pertaining to the characterization of exciton diffusion in organic semiconducting polymers as well as in chapter 6 where work has begun on developing a novel approach to increase the sensitivity of PPM to diffusive motion.

1.3 Superresolution Microscopy

Characterization of complex materials by visible light is limited to length scales greater than the diffraction limit of light (~200 nm) [37]. Both Abbe and Rayleigh similarly define the resolution of diffraction limited optical systems as

$$\begin{aligned} Abbe \rightarrow d_{Abbe} &= \frac{\lambda}{2NA} = fwhm_{\min} \\ Rayleigh \rightarrow d_{Rayleigh} &= \frac{1.22\lambda}{2NA} \end{aligned} \tag{1.4}$$

where $fwhm_{\min}$ is the PSF of the optical system at the diffraction limit, λ is the imaging wavelength, and NA is the numerical aperture of the optical system. Equation 1.4 also defines the minimum distance (d) at which two point emitters can be resolved from one another according the respective description [38]. The Abbe diffraction limit and the Rayleigh criterion are presented in Fig. 1.3 where the detected PSF is simulated consistent with coherent light microscopy and homodyne detection. Panel A shows the profiles of individual PSFs (dashed profiles) of two point emitters (red vertical lines) separated by d_{Abbe}, while panel B shows final image profile. Panels C and D show a similar comparison for point emitters separated by $d_{Rayleigh}$. In subsequent chapters the superresolution techniques developed within this thesis will be demonstrated to both reduce the PSF dimension of the imaging system and successfully resolve two closely spaced objects with respect to both the Abbe and Rayleigh criterion. [12, 13].

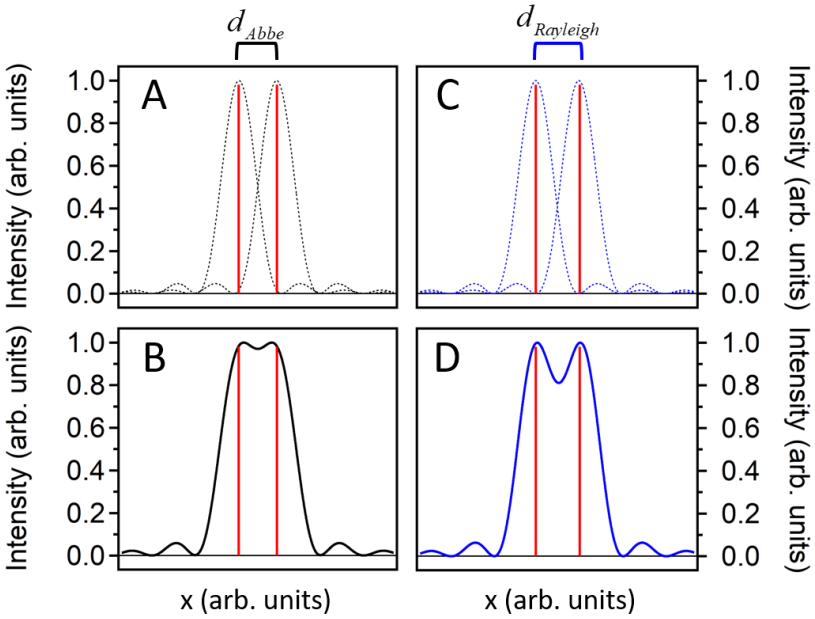

Figure 1.3. (A, B) Depiction of Abbe's diffraction limit and the (C, D) Rayleigh criterion. The point emitters being imaged are represented by delta functions (red).

The accuracy with which nanoscale materials systems can be characterized by visible light, far field spectroscopic methods is restricted by the diffraction limit (~200 nm). Therefore, development of optical techniques capable of surpassing the diffraction limit has been the focus of intense research over the past two decades [17-19, 22, 39]. Current and commonly used superresolution techniques include stimulated emission depletion (STED), (saturated) structured illumination microscopy ((S)SIM), photoactivated localization microscopy (PALM), and stochastic optical reconstruction microscopy (STORM) [40, 41]. Each of these techniques relies on the fluorescent nature of the material being characterized. Therefore, despite the improvement in spatial resolution, ultrafast photophysical processes and non-fluorescent species are not easily characterized by these methods.

Fig. 1.4 shows a general comparison of the temporal and spatial resolution of fluorescence based superresolution techniques and the label-free ultrafast methods described later in this section. SIM utilizes patterned excitation profiles, multiple images, and Fourier domain processing to achieve a two-fold improvement over the diffraction limit. Further, by exploiting saturated excitation, SSIM can theoretically provide limitless resolution restricted only by the signal-to-noise ratio (SNR) of the experiment [22, 39]. STED also exploits nonlinear processes to reduce the volume of the optical system PSF by depleting the contribution of emitted light beyond the center of a donut shaped pulse [17]. PALM and STORM can be considered methods of super-localization. Both methods rely on photoswitching of fluorescent chromophores which can be tracked over the course of multiple images to determine the exact location of emission sites. The spatial resolution is then defined by the certainty of that localization [18, 19].

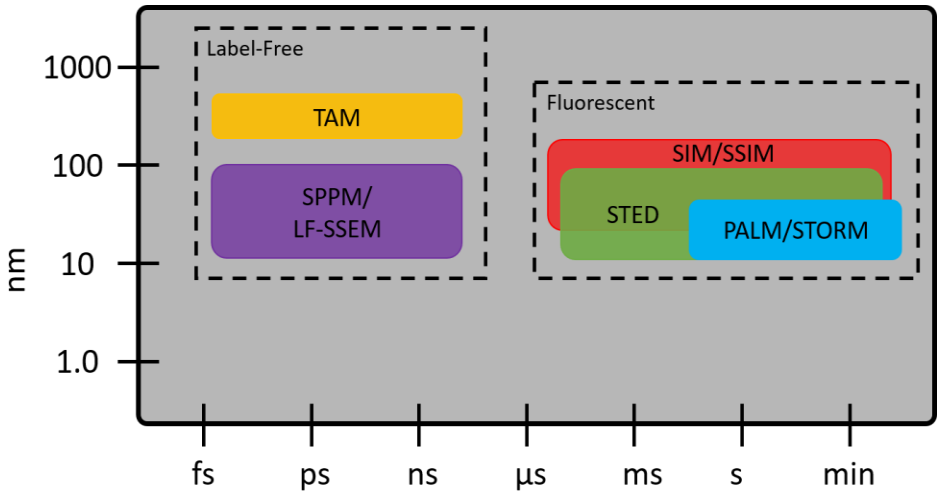

Figure 1.4. General comparison of previously developed fluorescence superresolution techniques and the label-free techniques described in this work [10, 12, 13, 40].

While the fluorescence based superresolution techniques described above are capable of characterizing fluorescent materials, many materials of interest are non-fluorescent, or cannot be labeled with fluorescent markers. Therefore, it is necessary to develop label-free superresolution techniques that are capable of characterizing non-fluorescent materials and reduce the need to utilize fluorescent markers that may alter the excited state environment of non-fluorescent materials [11, 14, 15]. In the work described below, a technique inspired by SIM is developed that uses a structured excitation profile to collect additional high spatial frequency information typically filtered by the optical system. Structured pump-probe microscopy (SPPM) not only surpasses the diffraction limit of light by a factor of 2, it also maintains the temporal resolution of conventional PPM (Fig. 1.4) which enables the spectroscopic characterization of sub diffraction limited volumes within complex materials systems. Further, label-free saturated structured excitation microscopy (LF-SSEM) provides ~30 nm spatial resolution. The comparison of the spatial and temporal capabilities of SPPM, LF-SSEM and fluorescent superresolution techniques is depicted in Fig. 1.4. Figure 1.4 shows that although utilizing fluorescent superresolution techniques allows for $\leq$10 nm spatial resolution, the temporal resolution is limited to microsecond or greater time scales. However, the ultrafast techniques described here enable both increased spatial resolution and sub-ps time resolution.

1.4 The Impact of Superresolution on Complex Material Characterization

The implementation of spectroscopic characterization techniques that can surpass the diffraction limit is crucial to the accurate understanding of disordered semiconductors,

polycrystalline thin films, and nanoscale optoelectronic devices. The techniques developed within this thesis (SPPM, LF-SSEM) represent a significant advancement in the capabilities of PPM to characterize complex nanoscale material systems. One class of materials that challenges traditional spectroscopic tools are thin films of semiconducting polymers. Specifically, the organic semiconducting polymer (OSP) poly [N-9’’-hepta-decanyl-2,7-carbazole-alt-5,5-(4’,7’-di-2-thienyl-2’,1’,3’-benzothiadiazole)] (PCDTBT) [42]. The heterogeneous nature of PCDTBT and many other organic semiconductors confounds traditional bulk spectroscopic measurements. Therefore, the development of superresolution techniques and further development of PPM is vital for the accurate characterization of complex materials systems photophysics. The remainder of chapter 1 will provide relevant background of photophysical processes in OSPs. Specifically, within the context of organic photovoltaic applications and the utilization of PPM to characterize material properties.

1.5 Organic Photovoltaics

Organic photovoltaics (OPVs) are of particular interest for producing renewable energy due to their low cost and ease of manufacturing [43]. Calculations show that solar cells operating at 12% efficiency and covering only 2% of the world’s total land area, would provide 67 terawatts (TW) of clean energy; two times the projected energy demands by the year 2050 (30 TW) [2]. With the most recent power conversion efficiency records of OPVs reaching a record 13.2 % [44], OPV technology is on the verge of producing the necessary amount of renewable energy for international sustainability and continued eco-

nomic growth. However, much remains unknown regarding the nano- and micro scale photophysical parameters that largely determine the photoconversion efficiencies (PCEs) of OPVs [24]. The inherent heterogeneity of organic semiconducting materials, specifically amorphous OSPs, complicates spectroscopic characterization leading to variations in reported photophysical parameters such as excited state lifetime and diffusivity. Using PPM it is possible to reduce the contributions of spatial heterogeneity, gain a more accurate understanding of the excited state dynamics, and provide vital knowledge toward the development of next generation OSPs. In the remainder of this section, the current understanding of OSP photophysics will be discussed in the context of light harvesting applications. Attention will then be directed toward the specific material, PCDTBT, studied in chapter 5 of this dissertation.

Following photoexcitation, the primary excited state species in organic semiconducting materials is a coulombically bound electron-hole pair called an exciton [29, 45]. Specific to most OSPs is the generation of Frenkel type excitons which are tightly bound and largely localized to a single chromophore, as opposed to a Wannier type excitons that are more weakly bound and extend across multiple chromophores [46, 47]. In contrast, photoexcitation of inorganic semiconductors results in the generation of free electrons and holes [48, 49]. Governing the formation of excitons in organic materials vs. inorganic materials is the difference between the dielectric constant of the two classes of materials [50, 51]. The dielectric constant of a semiconducting material denotes to what extent the Coulombic interaction between the electrons and holes is screened [52]. In materials with lower dielectric constants the dissociation of excitons is less energetically favorable. Dissociation

of excitons into free carriers is a prerequisite for a functioning photovoltaic cell. Therefore, understanding the mechanism of exciton dissociation in OSPs is crucial for increasing next generation OPV PCE.

In an attempt to overcome the energetic barrier associated with exciton dissociation, organic semiconductors are often utilized in donor-acceptor (D-A) blends. The application of D-A blends is in direct response to the discovery of the ultrafast charge transfer phenomena that occurs between donor and acceptor materials, first observed in the early 1990's [53]. In a D-A morphology, donor materials are typically strong optical absorbers such as OSPs and other organic semiconductors. While acceptor materials have complementary energy levels to the donor material (often a fullerene derivative or other small organic molecule) such that charge transfer at the interface results in the preferential transfer of the electron to the acceptor material leaving the hole in the donor material [29, 54].

A spatial depiction of exciton generation, transport, and dissociation in a D-A blend is provided in Fig. 1.5 where the donor material is depicted as an OSP (black lines) and the electron accepting material is a fullerene derivative (red circles). Initial excitation of the OSP produces mobile carriers (electrons and holes). However, due to the low dielectric constant of the OSP the free carriers self-localize within 100 fs to form tightly bound Frenkel-type excitons [46, 55, 56]. These excitons then migrate through the polymer networks to lower energy states that are present due to varying conjugation lengths within the polymer network [57]. If exciton diffusion intersects with a D-A interface, the energetic landscape promotes efficient exciton dissociation [53]. Once separated, the electron and hole

are then able to travel along channels in the fullerene and polymer, respectively, towards the anode and cathode of a working solar cell.

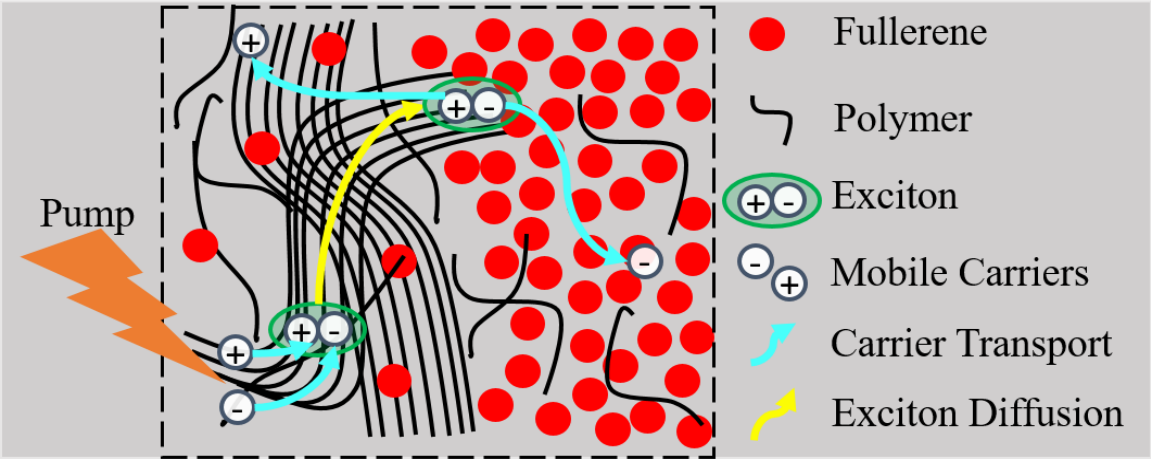

Figure 1.5. Free charge generation mechanism for organic D-A blends. The polymer and fullerene microstructure is represented by black lines and red circles, respectively. The initial excitation produces free electron and holes which rapidly self-localize to form a tightly bound singlet exciton which will only efficiently dissociate at the donor-acceptor interface.

1.5.1 PCDTBT

To further improve the exciton dissociation efficiency in D-A blends, a new class of OSPs was developed which have both an electron donating and accepting fragment within the repeat unit of the polymer. These copolymers have proven to enhance exciton transport and dissociation due to the inherent energetic landscape caused by the alternating fragments [42, 58-60]. One copolymer that has been significantly studied as the donor material in photovoltaic applications is poly [N-9’’-hepta-decanyl-2,7-carbazole-alt-5,5-(4’,7’-di-2-thienyl-2’,1’,3’-benzothiadiazole)] (PCDTBT). When blended with [6,6]-phenyl-C 70 butyric acid methyl ester ($PC_{70}BM$) as the accepting molecule, PCDTBT based photovoltaic devices have reached efficiencies approaching 12% [24, 56, 61]. Figure 1.6

shows the energy level diagram of the bulk heterojunction formed between PCDTBT and $PC_{70}BM$. PCDTBT is a highly conjugated copolymer with a relatively low bandgap (1.9 eV) making it an ideal material for absorbing a significant fraction of the visible solar spectrum. PCDTBT can also be utilized in a variety of optoelectronic applications [26, 62] and has also been shown to have sufficient operating lifetimes for OPV applications, theoretically extending to 15 years [25]. In Chapter 5 a complete analysis of exciton transport dynamics in neat PCDTBT is described, including the measurement of micron scale exciton diffusivity in amorphous and aligned polymer chains. Exciton diffusion is a crucial parameter with respect to the OSP based photovoltaics and other optoelectronic devices. Understanding the role morphology dependent exciton diffusivity plays in the excited state dynamics of OSPs will provide vital knowledge to guide the fabrication of next generation OPVs, synthesis of novel OSPs, and effective use of OSPs in other optoelectronic devices.

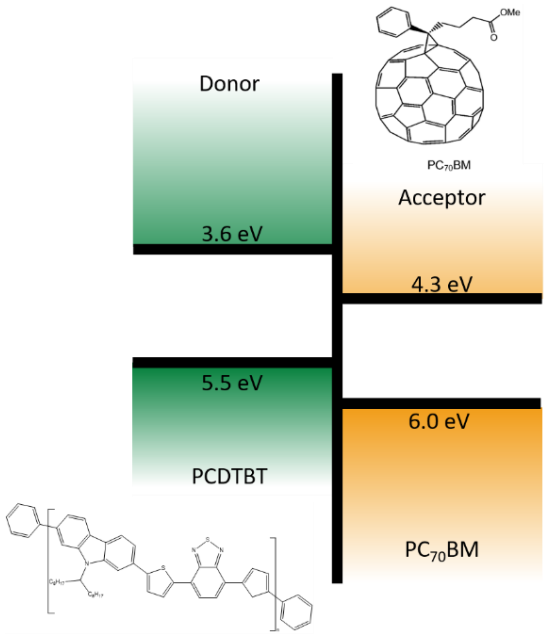

Figure 1.6. Energy levels of a bulk heterojunction formed between PCDTBT and $PC_{70}BM$.

1.6 Thesis Organization

The remainder of this dissertation is organized as follows:

Chapter 2 reports the experimental development of SPPM. SPPM is demonstrated to be a valid superresolution technique capable of achieving a two-fold increase in spatial resolution beyond the diffraction limit while maintaining the femtosecond temporal resolution of traditional PPM.

Chapter 3 describes the theoretical background associated with SPPM and provides a detailed description of the necessary mathematical formulation and experimental modifications to achieve a two-fold increase in resolution relative to the diffraction limit in two dimensions. Further, the chapter explores how varying pump and probe wavelengths, and instrument noise affect resolution enhancement.

Chapter 4 describes the theoretical development of LF-SSEM where structured excitation can theoretically produce ~30 nm spatial resolution by exploiting the saturation of the absorption process. This chapter will describe the necessary experimental requirements and the image reconstruction process to produce superresolution images under saturated excitation conditions.

Chapter 5 reports novel findings of exciton diffusion in PCDTBT thin films. Utilizing PPM, unexpected rates of exciton diffusion have been observed and proposed as being due to localized self-organization of polymer chains. These results are supported by the macroscopic alignment of polymer chains as well as the development of a coarse grain Monte Carlo simulation.

Chapter 6 is a description of ongoing work toward direct imaging and quantification of sub-10 nm carrier diffusion lengths. Differential detection pump-probe microscopy (DDPPM) uses two temporally separated pump-probe signals to preferentially increase the sensitivity of the optical system to the presence of diffusive excited states. Preliminary results and modeling show that the technique remains limited by the noise of the optical system but that continued development will result in a useful spectroscopic tool that has greater sensitivity to diffusive motion than current PPM technology.

Chapter 7 serves to address the broader impacts of the work described in this dissertation by presenting ways to utilize and improve the developed techniques and to continue investigation of OSP photophysics.

CHAPTER TWO

SUPERRESOLUTION STRUCTURED PUMP-PROBE MICROSCOPY

Contribution of Authors and Co-Authors

Manuscript in Chapter 2

Author: Eric S. Massaro

Contributions: Performed the superresolution imaging experiment on Silicon nanowires. Generated figures and co-wrote the manuscript.

Co-Author: Andrew H. Hill

Contributions: Aided in experimental development and manuscript editing.

Co-Author: Erik M. Grumstrup

Contributions: Developed theoretical framework for superresolution imaging and co-wrote manuscript

Manuscript Information Page

Eric S. Massaro, Andrew H. Hill, and Erik M. Grumstrup

ACS Photonics

Status of Manuscript:
____ Prepared for submission to a peer-reviewed journal
____ Officially submitted to a peer-review journal
____ Accepted by a peer-reviewed journal
_X_ Published in a peer-reviewed journal

Published by the American Chemical Society
Superresolution Structured Pump-Probe Microscopy, *ACS Photonics* 2016, 3, 501-506

SUPERRESOLUTION STRUCTURED PUMP-PROBE MICROSCOPY

The following (adapted) work has been published in ACS Photonics

*Eric S. Massaro[1], Andrew H. Hill[2], and Erik M. Grumstrup[1, 2]**

1. Department of Chemistry and Biochemistry, Montana State University, Bozeman, Montana 59717, United States
2. Montana Materials Science Program, Montana State University, Bozeman, Montana 59717, United States

2.1 Introduction

PPM is a powerful tool for studying nonequilibrium dynamics in a variety of complex materials systems including nanostructures, low dimensional semiconductors, and material interfaces. The simultaneous sub-micron spatial resolution and femtosecond temporal resolution enabled by the technique provides detailed, structurally-correlated insights into intraparticle heterogeneity [63-65], free carrier transport [35, 66, 67], surface plasmon propagation [68], and unique interfacial states [69-72], that are inaccessible with conventional spectroscopies or microscopies. However, like all diffraction-limited optical techniques, the spatial resolution of PPM is restricted to probe areas greater than ~ 200 nm as defined by the Abbe limit [37]*:*

$$fwhm_{\min} = \frac{\lambda}{2NA}. \tag{2.1}$$

where λ is the wavelength of the imaging light, NA is the numerical aperture of the objective, and $fwhm_{\min}$ is the characteristic dimension of the optical system's point spread function (PSF).

Imaging at length scales smaller than 200 nm requires approaches that circumvent the limits of lens-based diffractive microscopes. While a number of fluorescence-based microscopies [19, 73-78], electron microscopies (SEM and TEM [79]), and Atomic Force Microscopy (AFM [80]) substantially improve spatial resolution, these techniques provide little or no dynamical information. To interrogate transient dynamics on sub-diffraction-limited length scales, several approaches have been employed. Tip-enhanced techniques that couple ultrafast laser pulses together with a sub-wavelength scanning probe can resolve ultrafast dynamics on length scales far below the diffraction limit [81, 82]. While highly promising, these measurements are complicated by a large far-field background that must be discriminated from the desired tip-localized signal and by perturbations introduced by system-probe tip coupling which can affect the observed material dynamics. Far-field approaches are experimentally simpler and can provide insight into electronic environments isolated from the surface [83]. A pump-probe analog to STED was recently reported, in which a third shaped laser pulse temporally spaced between the pump and probe pulses saturates an annular region surrounding the central excitation spot [84]. While this approach narrows the effective point spread function of the microscope, the third intense saturation pulse can cause photobleaching and highly-nonlinear light-matter interactions which may be problematic for both imaging and spectroscopic applications. A similar approach utilizes differential transient absorption in place of saturable absorption, retaining the use of a third pump pulse in order to confine the dimensions of the pump-probe response in both linear and nonlinear regimes [85].

In this chapter, a technique termed Structured Pump-Probe Microscopy (SPPM) will be described experimentally. SPPM employs a modulated pump excitation field to provide ultrafast spectroscopic measurements of sub-diffraction-limited sample areas. SPPM is theoretically related to SIM, a fluorescence imaging technique that utilizes a structured excitation field to improve spatial resolution [15, 20, 22, 86]. Here, the SIM approach is adapted to PPM by implementing a structured pump excitation field along with a diffraction-limited probe field. Structuring the excitation field expands the optical system's optical transfer function (OTF), and improves spatial resolution by nearly a factor of two. In section 2.2 of this chapter, SPPM is used to characterize free carrier dynamics in silicon nanowires (NWs) and show the technique can achieve an effective point spread function (PSF) with a ~114 nm fwhm while maintaining the temporal resolution of PPM. These results suggest conventional far-field optics, in conjunction with spatial pulse shaping, may provide an experimentally accessible approach for interrogating dynamics of complex materials systems with sub-100 nm spatial resolution. Section 2.3 of this chapter will provide a description of the experimental methodology required for SPPM. However, a comprehensive discussion of imaging theory and reconstruction will be provided in chapters 3 and 4.

2.2 Structured Pump-Probe Imaging and Spectroscopy

To achieve the improved PSF of SPPM, a computer-programmable digital micromirror device (DMD) encoded with a fringe pattern is used to create a sinusoidally modulated pump field at the focus of the microscope objective (0.9 NA). A diffraction-limited

probe pulse is spatially overlapped with the pump field and the NW sample is raster scanned to produce a pump-probe image at a well-defined delay time, Δt. Because the induced polarization of the sample depends on the product of the pump intensity and the probe field, the effective pump-probe excitation field is spatially modulated. By combining images collected with three different pump pattern phases (details below), the spatial modulation in the images provides access to additional high (spatial) frequency information that is inaccessible with conventional approaches.

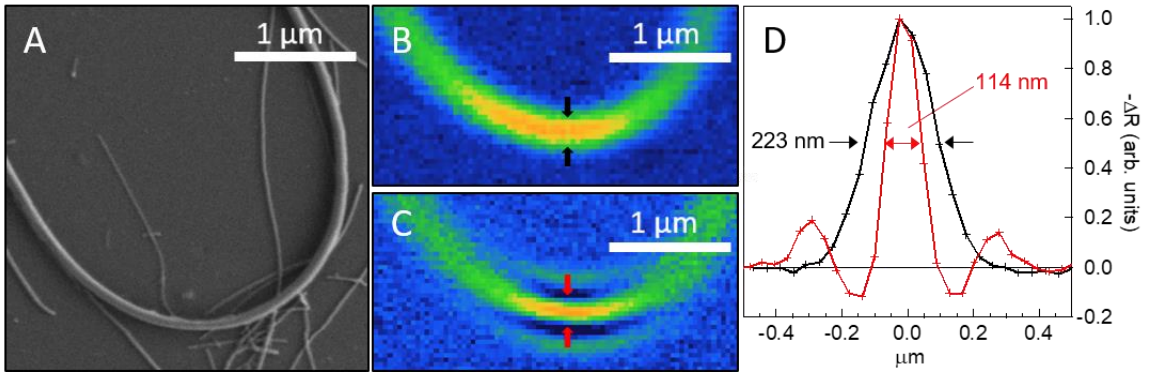

Figure 2.1. Comparison of diffraction limited and structured pump-probe microscopy. A) Field emission micrograph of a 100 nm diameter silicon nanowire. B) Diffraction limited pump-probe image of the NW in panel A at Δt = 0 ps. C) SPPM image achieved through reconstruction D) Linewidth comparison at positions indicated by the arrows in the two pump-probe images. Black – diffraction limited; red – SPPM.

Figure 2.1 presents the enhanced imaging capability provided by SPPM. Panel A shows a field emission micrograph of a 100 nm diameter silicon NW deposited on a quartz substrate. A diffraction-limited pump-probe image of the same NW is shown in panel B. To collect the image, the λ = 400 nm pump and λ = 585 nm probe beams were spatially overlapped at the sample plane and the NW was raster scanned with a piezoelectric translation stage. The fwhm of the PSF of the optical system in this modality is determined by

the product of overlapping pump and probe spot sizes. Panel C shows the SPPM image of the same NW. In this image, the PSF is improved by nearly a factor of two relative to conventional pump-probe imaging. The improvement can be more clearly seen in a comparison of the diffraction-limited and SPPM profiles plotted in panel D - whereas the conventional approach produces a fwhm of 223 nm, the SPPM image has a linewidth of 114 nm. Note that due to the low diffraction efficiency of the DMD at 400 nm, the resolution enhancement is limited to the y-axis only. However, two-dimensional resolution enhancement can be readily achieved by implementing a two-dimensional pump modulation scheme and performing a multidimensional image reconstruction (Chapter 3).

A frequency domain representation of the enhanced resolution enabled by SPPM is shown in Fig. 2.2 where panels A and B show the image spectra of the diffraction limited (DL: panel A) and SPPM (panel B) images of Fig. 2.1, respectively. The image spectrum is obtained by performing a Fourier Transform of the real space image. Performing SPPM effectively amplifies the contribution of high spatial frequency components that would typically be attenuated by the optical system. A profile comparison of the two frequency space images is shown in panel C of Fig. 2.2 showing clear amplification of high frequency spatial information by utilization of SPPM.

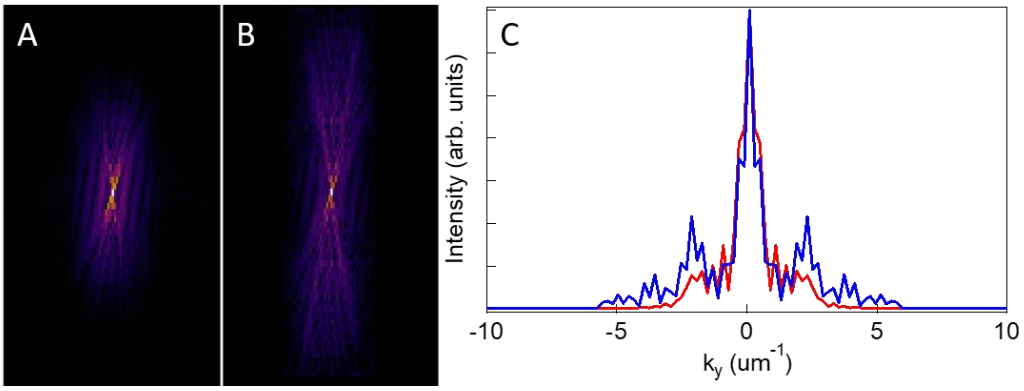

Figure 2.2 (A) Diffraction-limited and (B) SPPM Fourier space power spectra of images shown in Figure 2B and 2C, respectively. (C) Profiles taken from the center column of panel A (red), and panel B (blue) to show the greater width of the OTF in SPPM.

Figure 2.3 presents a second comparison of diffraction-limited and SPPM approaches. Panels A, B, and C of Figure 2.3 show field emission microscope (FEM), SPPM, and diffraction limited images, respectively, of a single Si NW that is bent in a hairpin geometry. Comparison of the images in panels B and C shows that in contrast to conventional pump-probe microscopy, SPPM is capable of resolving the two regions of the NW in close proximity. The increase in spatial resolution can be more clearly seen in Panel D, where profiles of the two images taken from the locations indicated by the dashed lines are shown together with a profile taken from the FEM. Interestingly, both diffraction limited pump-probe and SPPM imaging show anomalous behavior when the NW is within ~200 nm of itself (see region to the left of the dashed line in panels B and C). These effects, which manifest as a change in signal sign, likely arise from optical system aberrations and interference of the field radiating from two image regions, however a detailed understanding requires further investigation.

While the increased imaging resolution represents an improvement over the diffraction limit, it is the ability to acquire ultrafast spectroscopic information from a sub-diffraction limited volume that makes SPPM particularly valuable for characterizing complex materials systems. Panel E shows a comparison of the kinetics collected with the enhanced resolution and diffraction-limited approaches. Within the context of the imaging modality discussed above, an SPPM kinetics trace can be understood as a single pixel image, collected at multiple delay times. Three individual kinetics traces are collected with shifted pump field patterns and combined to produce the SPPM kinetics trace that reports on the dynamics of a sub-diffraction limited sample volume. Photoexcitation of silicon nanowires at 400 nm is known to produce free charge carriers, which primarily decay through surface recombination [34]. The SPPM kinetics traces in panel E of Fig. 2.3 are consistent with this mechanism and show the two regions of the NW have slightly different surface recombination velocities of 3.8×10^4 cm/s (red) and 8.8×10^4 cm/s (green) [87]. In contrast, the diffraction limited measurement shows a surface recombination velocity of 6.5×10^4 cm/s (black), a value that reflects a weighted average of the individual NW recombination velocities.

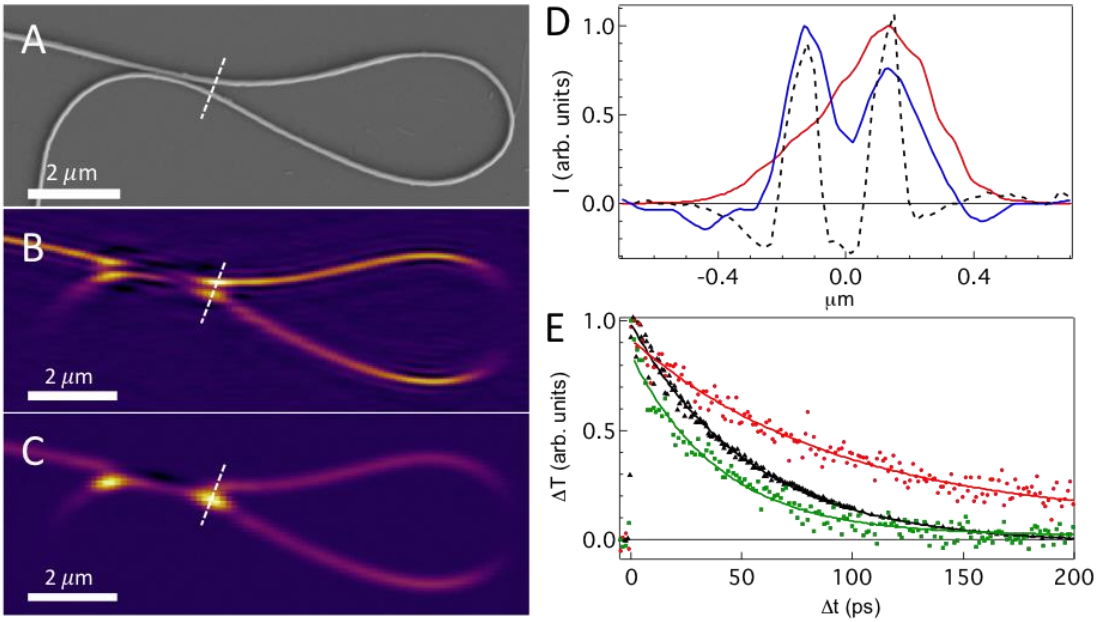

Figure 2.3. SPPM spatial resolution enhancement and sub-diffraction limit spectroscopic characterization. (A) Field Emission micrograph of a single 140 nm silicon nanowire. (B) SPPM image with enhanced resolution along the y-axis. (C) Diffraction limited pump-probe image of the nanowire in panel A taken at Δt = 0 ps. (D) Lineshape comparisons of diffraction-limited pump-probe (red) and SPPM images (blue) of panels B and C taken from location indicated by dashed line in each panel. Also shown is the profile taken from the SEM (black, dashed). (E) Transient kinetics collected from image region spanned by the dashed lines in panels B and C. Traces 1 (red) and 2 (green) were collected with enhanced spatial resolution and show the NW has different recombination kinetics along its length. Trace 3 (black) represents kinetics collected using standard diffraction-limited pump-probe microscopy. The diffraction-limited kinetics average over the dynamics of both NW regions.

So far, SPPM has been shown to surpass the diffraction limit as defined by Abbe (Fig. 2.1), and that objects in close proximity to each other can be spatially and spectroscopically resolved (Fig. 2.3). However, to further confirm that SPPM meets the Rayleigh criterion, as demonstrated in Fig. 2.3, a simulation of the experimental conditions is performed. In Fig. 2.4, pump-probe lineshapes were calculated for two features chosen to reproduce the nanowire geometry found in Fig. 2.3. Nanowires with a width of 140 nm,

placed 250 nm apart, were modeled as hemispherical features. The pump-probe signal intensity was assumed to be proportional to the physical cross section of the nanowires. The relative intensity of the two 'nanowires' was varied between 1.0 (equal intensity, panel A) and 0.25 (panel D), providing a range of values that can be compared with the experimental images in Fig. 2.3. The mathematical calculation of the DL and the SPPM lineshapes will be discussed in chapter 3 (DL: Eq. 3.3, SPPM: Eqs. 3.5 and 3.6). As demonstrated by the simulations in Fig. 2.4, the DL lineshape for the simulated imaging system never meets the Rayleigh criterion (>19% modulation between peaks) for resolving two features [38]. On the other hand, SPPM clearly resolves the two features in all cases thus fulfilling the Rayleigh criterion.

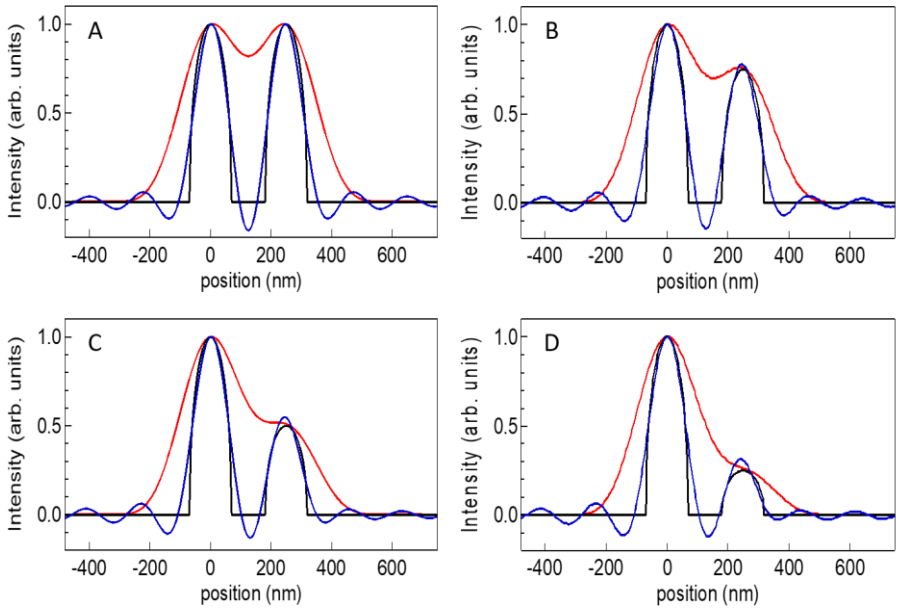

Figure 2.4 Theoretical comparison between ideal (black), diffraction-limited (red), and SPPM (blue) images. The simulated lineshapes are shown for two 'nanowires' whose relative signal intensity is 1.0 (panel A), 0.75 (panel B), 0.50 (panel C), and 0.25 (panel D). Simulated nanowires are 140 nm in diameter and separated by 250 nm. At the diffraction limit, the Raleigh criterion is not met in any of the panels, whereas the two features are resolvable in all cases for SPPM.

2.3 Methods

A schematic of the home-built pump-probe microscope used to perform the experiments described in this chapter is presented in Fig. 2.5. A portion of the output from a femtosecond Ti:Sapphire oscillator (Spectra Physics MaiTai: 800nm, 79 MHz, 90 fs fwhm) is split to produce pump and probe paths. The pump line is coupled into an acoustooptic modulator (AOM) before frequency doubling in a β-Barium borate (BBO) crystal to produce 400 nm excitation pulses (23 pJ/pulse). The pump beam is directed toward the DMD (Texas Instruments DLP Lightcrafter) to produce +/- 1 diffraction orders which are collected with a tube lens (L1). The DMD produces many diffraction orders which must be optically masked before the desired orders are coupled into the objective near the edge of the back aperture. Interference of the +/- 1 diffraction orders at the sample plane produces the necessary sinusoidal excitation profile. The probe is derived from a photonic crystal fiber (PCF), which produces a broadband supercontinuum spanning 500 nm to 1200 nm. The continuum is passed through an interference filter (585 nm +/- 5 nm), directed onto a computer controlled delay stage, and coupled onto GV mounted mirrors and a 4-f lens (200 mm) system to direct the beam to the objective. Pump and probe beams are coupled collinearly into the back aperture of a 100X apochromatic microscope objective (0.9 NA) with a dichroic beamsplitter. The focused probe spot is 340 nm fwhm at the sample position with a fluence of 0.9 mJ/cm^2. The sample is held on a piezoelectric X-Y stage at the focal point of the objective. The retroreflected probe is picked off with a 50/50 beamsplitter and directed onto one channel of a balanced photodetector. The delay dependent change in probe reflectivity is measured with a digital lock-in amplifier (Stanford Research SR-844)

phase locked to the pump modulation frequency (100 kHz). While acquisition time varies with the number of pixels in the image, the diffraction-limited pump-probe images shown in Figs. 2.1 and 2.3 of this manuscript required approximately 1 minute each to collect. SPPM images require acquisition times that are approximately three times longer as multiple pump phases are required to reconstruct the image.

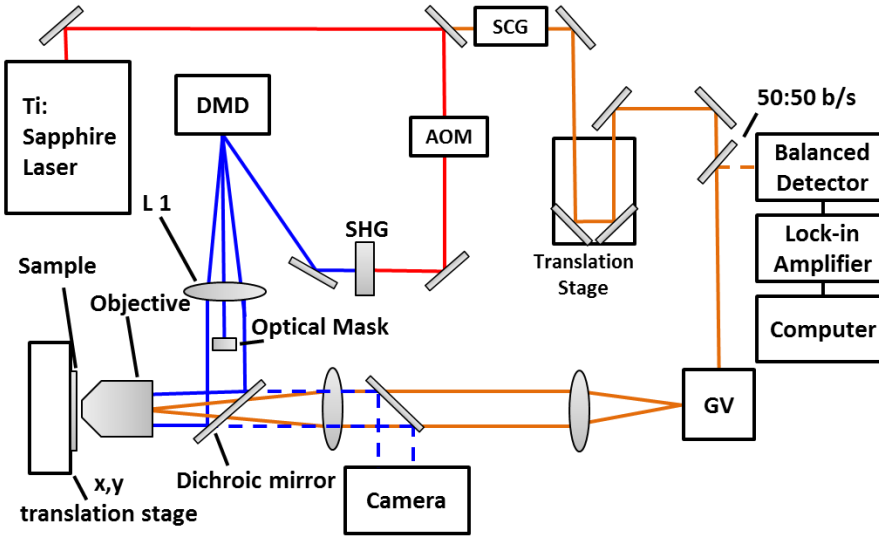

Figure 2.5. Schematic of DMD-based structured pump-probe microscope.

The sinusoidal pump intensity and phase utilized in order to collect additional high spatial frequency information is controlled by encoding a pattern on the DMD positioned at an image plane of the microscope. Panel A of Fig. 2.6 shows one such pattern, which is composed of a periodic array of 6 "on" and 6 "off" pixels. The corresponding pump intensity as recorded by a camera placed at a second image plane of the microscope is shown in panel B. Panel C shows a phase-shifted DMD pattern with $\varphi = \pi / 2$. In this case, the corresponding pump field intensity (panel D) is spatially shifted by π relative to that in panel

B. The factor of two difference stems from the coherent interference of the two counter-propagating pump fields.

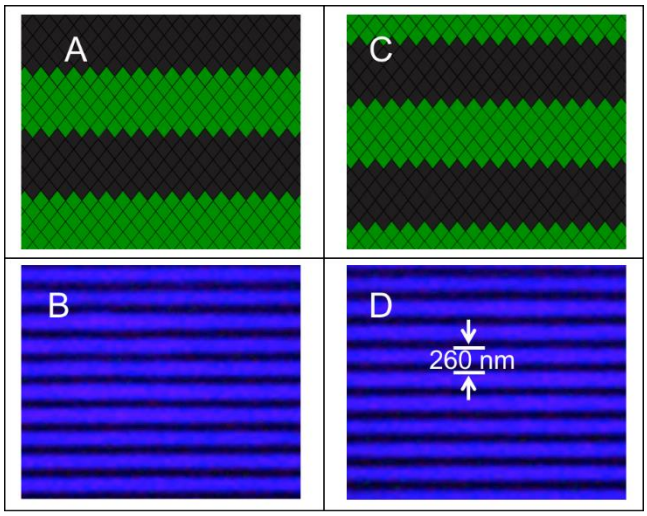

Figure 2.6. Phase variation of the DMD generated modulated pump pattern. (A, C) Mirror positions (green – "on" black – "off") encoded on the DMD to produce the pump intensity modulation. Panels A and C have a $\pi/2$ relative phase shift. (B) Camera image of the 0-phase offset modulation pattern. (D) Camera image of the $\pi/2$ phase shifted pattern. The camera images have a relative phase shift of π due to interference of the two 1st order diffractions.

To generate enhanced resolution images like panel C of Fig. 2.1 and 2.3, three structured pump-probe images are collected for three unique pump phases, $0 \le \varphi < \pi$. The phase shift of the pump pattern causes variation in the spatial profile of the pump-probe overlap region as the relative orientation of the focused probe beam and the modulated pump pattern changes. This effect is illustrated in Fig. 2.6, where structured pump-probe images at Δt = 0 ps are shown for DMD phases of $\varphi = 0$ (panel A) and $\varphi = \frac{\pi}{2}$ (panel B). In panel A, the minimum of the pump intensity is roughly centered in the probe spot, whereas a maximum is centered for panel B. Panel C of Fig. 2.6 shows profiles of the two

images in the locations indicated by the dashed lines. A full theoretical description of the image reconstruction technique is provided in Chapter 3.

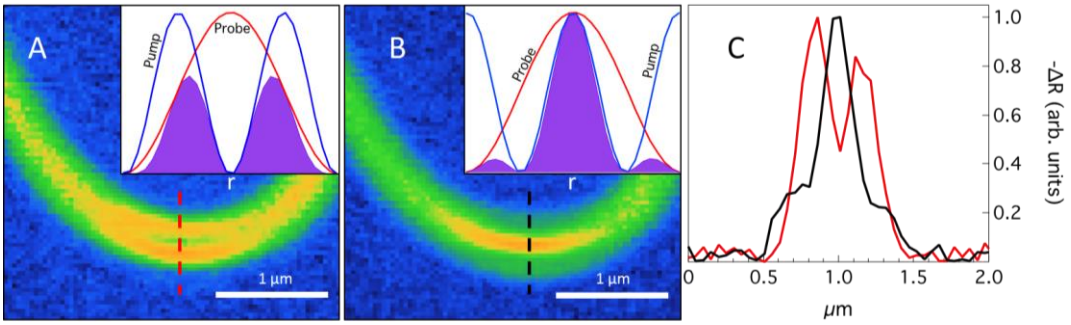

Figure 2.7. Spatially overlapped pump-probe images of silicon nanowires with structured pump excitation. (A) Probe spot centered on a minimum of the modulated pump pattern. (B) Probe spot centered over the top of an individual pump peak. The insets in panels A and B illustrate the effective excitation field in their respective panels. (C) Intensity profile of both images with slices taken at the red and black dashed lines in panels A and B, respectively.

2.4 Conclusion

In summary, this chapter demonstrates the development of far-field, sub-diffraction-limited pump probe microscopy utilizing a spatially structured pump excitation field. The point spread function of SPPM is smaller than the diffraction limit by nearly a factor of two. The enhanced spatial resolution achieved by the technique provides a facile approach for interrogating transient dynamics of interfaces, nanostructures, and nanoscale domains in complex materials with substantially greater precision. While imaging linewidths of 114 nm FWHM are reported here, a higher numerical aperture objective (NA 1.4) may enable further improved spatial resolution, substantially broadening the scope of far-field transient microscopy for characterizing complex materials and biological systems.

2.5 Acknowledgments

The authors would like to thank Prof. Jim Cahoon at the University of North Carolina Chapel Hill for providing nanowire samples. The authors gratefully acknowledge support from Montana State University and the Office of Basic Energy Sciences of the U.S. Department of Energy through Grant DE-SC0014128.

CHAPTER THREE

IMAGING THEORY OF STRUCTURED PUMP-PROBE MICROSCOPY

Contribution of Authors and Co-Authors

Manuscript in Chapter 3

Author: Eric S. Massaro

Contributions: Performed theoretical development of two-dimensional structured pump-probe microscopy. Generated figures and prepared the manuscript for submission.

Co-Author: Andrew H. Hill

Contributions: Aided in manuscript preparation.

Co-Author: Casey L. Kennedy

Contributions: Aided in manuscript preparation.

Co-Author: Erik M. Grumstrup

Contributions: Performed theoretical development of structured pump-probe microscopy and manuscript preparation.

Manuscript Information Page

Eric S. Massaro, Andrew H. Hill, Casey L. Kennedy, and Erik M. Grumstrup

Optics Express

Status of Manuscript:
____ Prepared for submission to a peer-reviewed journal
____ Officially submitted to a peer-review journal
____ Accepted by a peer-reviewed journal
_X_ Published in a peer-reviewed journal

Published by The Optical Society
Imaging Theory of Structured Pump-Probe Microscopy, *Optics Express* 2016, Vol. 24, No. 18, Pg. 20968-20880

IMAGING THEORY OF STRUCTURED PUMP-PROBE MICROSCOPY

The following (adapted) work has been published in Optics Express

*Eric S. Massaro[1], Andrew H. Hill[2], Casey L. Kennedy[1], and Erik M. Grumstrup[1, 2]**

1. Department of Chemistry and Biochemistry, Montana State University, Bozeman, Montana 59717, United States
2. Montana Materials Science Program, Montana State University, Bozeman, Montana 59717, United States

3.1 Introduction

The electronic structure of complex materials systems is often altered by a variety of localized defects, i.e. compositional and morphological variation, point defects, and grain boundaries [5]. Transient absorption and related nonlinear microscopies, which provide both high spatial and temporal resolution, are important tools for understanding how such heterogeneities impact bulk and nanoscale material functionalities, particularly for non-equilibrium processes like photogeneration, charge separation, carrier transport, and recombination [6-8]. To enable more precise structure-function correlations in complex materials systems, extensive technique development efforts have been directed toward surpassing the diffraction limit [14, 18, 19, 73, 88-91]. With a similar goal in mind, SPPM (experimentally described in Chapter 2) has been developed and is capable of probing material properties with a two-fold increase in spatial resolution over the diffraction limit.

Here, the imaging theory of SPPM is comprehensively described. The theoretical description provided in this chapter explores the technique parameters and the limitations

of SPPM to broaden the utility of the technique. The remainder of this chapter is organized as follows. In Section 3.2, the experimental design of two-dimensional SPPM is briefly discussed to connect the experimental description of SPPM in chapter two to the theoretical description within this chapter. Section 3.3 develops the imaging theory of both DL and structured pump-probe approaches. In Sections 3.4 and 3.5, the conjugate space reconstruction procedure used to achieve sub-diffraction limited imaging and collect transient kinetics is described. Finally, in Section 3.6 the modeling results including resolution enhancement, wavelength dependence, and image artifacts that can limit the performance of SPPM are described.

3.2 Experimental

While a more detailed discussion of the relevant experimental factors can be found in Chapter 2 [13], a condensed schematic of the experimental apparatus utilized for 2D SPPM is shown in Fig. 3.1. The key requirement to implement SPPM is sample photoexcitation by a structured excitation field. To achieve the structured field, four diffraction orders from a grating are overlapped at the sample position to create an interference fringe pattern with a well-defined spatial phase. While the interference pattern can be produced with actuator-mounted diffraction gratings placed at the image plane of the microscope objective [22], computer-controlled two-dimensional spatial light modulators (SLMs) are facile and accessible alternatives, particularly with the advent of low-cost DMDs [13]. The probe pulse is focused to a diffraction limited spot at the sample plane, and the sample is raster scanned with a piezoelectric translation stage. The schematic in panel A shows a

reflection-type detection geometry, however transmission detection is also possible with a second objective placed behind the sample.

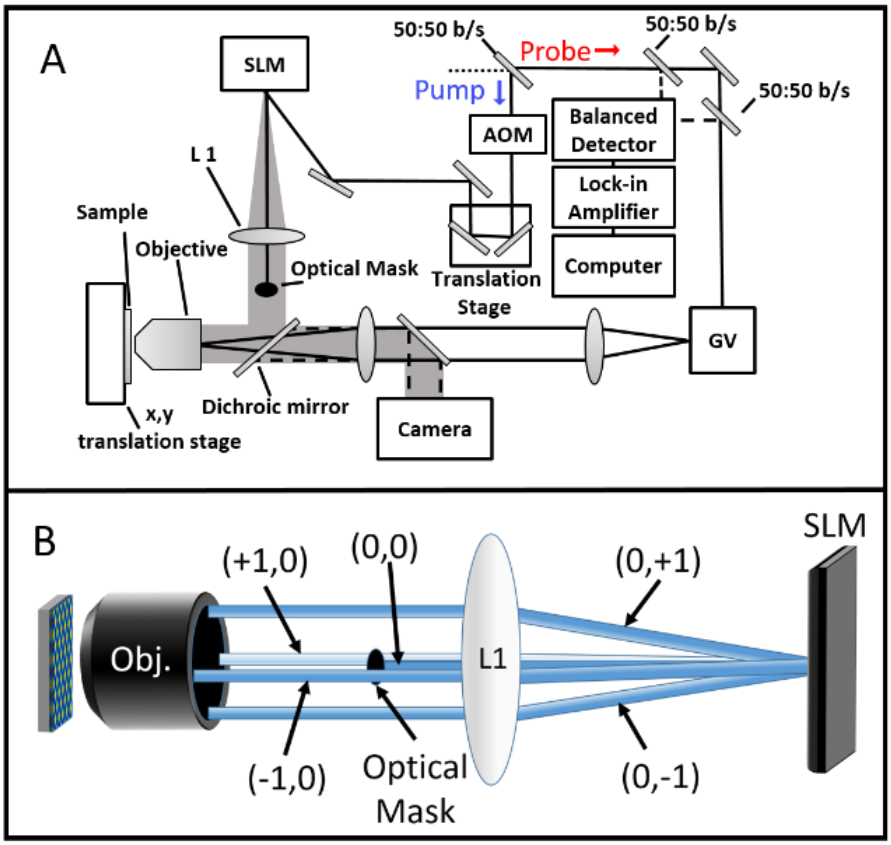

Figure 3.1. (A) Experimental schematic of two-dimensional SPPM. The dotted line represents the input pulse train derived from a suitable ultrafast laser source. After a beamsplitter, the probe pulse is directed to a set of GV mirrors and coupled through a 4-f lens system onto the back aperture of the objective. The GV mirrors provide a reliable method for spatially overlapping the pump and probe pulses. The pump path is directed through an AOM, a translating delay stage, and toward an SLM, which is programmed to display a two-dimensional grating pattern. The four 1st order diffractions are collected by a collimating lens (L1) in such a way that they are incident at the far outer edges of the objective aperture. (B) An expanded view of the optics needed to create a structured pump excitation field. The 5 diffraction orders from the SLM are labeled in the (x, y) directions where a value of one denotes the 1st order diffraction of the respective axes. The (0,0) diffraction order is blocked with a mask.

3.3 Imaging Theory

3.3.1 Diffraction Limited Imaging

In time-resolved PPM, an image is formed by recording the position-dependent, transient sample response after photoexcitation with a coherent, pulsed light source. The pump-probe image (I_N) can be described by:

$$I_N(r) = o(r) \otimes \left(E(r) \otimes h(r) \right) \tag{3.1}$$

where the object function ($o(r)$) contains both the spatial position and the third-order non-linear response of the sample, $E(r)$ is the electric field, and the imaging system PSF is given by $h(r)$. In PPM, the effective field $(E \otimes h)_{eff}$ is described by:

$$\left(E \otimes h \right)_{eff} = \left| E_1(r) \otimes h_1 \right|^2 \cdot \left| E_2(r) \otimes h_2 \right|^2 \tag{3.2}$$

where E_1 and E_2 are the pump and probe electric fields, each convolved with their respective PSFs (h_1, h_2) [86, 92]. Substitution of Eq. 3.2 into Eq. 3.1 yields the DL pump-probe image (I_{DL}):

$$\begin{aligned} I_{DL} &= o(r) \otimes \left| E_1(r) \otimes h_1 \right|^2 \cdot \left| E_2(r) \otimes h_2 \right|^2 \\ &= o(r) \otimes \left(\delta(r) \otimes h_1 \right)^2 \cdot \left(\delta(r) \otimes h_2 \right)^2 \\ &= o(r) \otimes \left(h_1^2 \cdot h_2^2 \right) \end{aligned} \tag{3.3}$$

In the second line of Eq. 3.3, the delta functions describe the pump and probe fields, overlapped at the same position in the image plane. The Fourier Transform (FT) of Eq. 3.3

yields the conjugate-space representation of the DL image, where capital letters and tildes are used to distinguish conjugate-space terms:

$$\tilde{I}_{DL}(k) = \tilde{O}(k) \cdot \left[\tilde{H}_1(k) \otimes \tilde{H}_1(k) \otimes \tilde{H}_2(k) \otimes \tilde{H}_2(k) \right] \tag{3.4}$$

In Eq. 3.4, $\tilde{O}(k)$ is the complete image spectrum, and the H_n are coherent optical transfer functions (OTFs) for the pump (n = 1) and probe (n = 2) assumed here to be real-valued. A coherent OTF acts as an ideal spatial frequency bandpass filter which transmits low frequency information unaltered and completely attenuates any information that lies outside the passband [93]. As illustrated in Fig. 3.2, the effective OTF, which resembles a Gaussian function for the DL imaging case, is formed from the triple convolution of the H_n. In DL pump-probe imaging, spatial resolution of the image, $I_{DL}(r)$, (the inverse Fourier transform of $\tilde{I}_{DL}(k)$) is determined by the extent to which the effective OTF attenuates high spatial frequency object information.

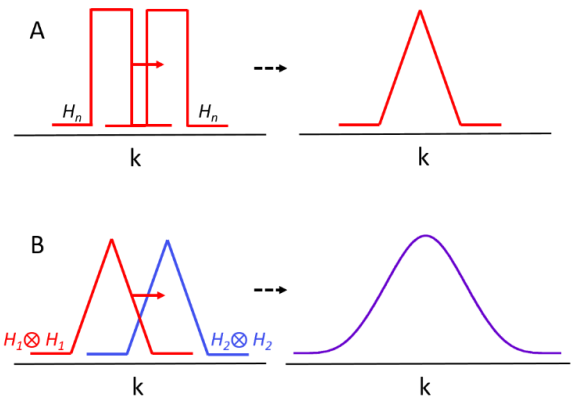

Figure 3.2. One-dimensional illustration of four component convolution in Eq. 3.4. (A) Coherent OTFs H_n are convolved, producing a triangle function for both pump (n = 1) and probe (n = 2). (B) Convolution of the pump and probe OTFs produced in step 1 resulting in the diffraction-limited effective OTF.

3.3.2 Structured Imaging

In contrast to the diffraction limited case, SPPM utilizes a structured pump electric field comprised of two perpendicularly propagating sinusoidal fields:

$$E_1(r) = \exp(ik^x r + \varphi^x) + \exp(-ik^x r - \varphi^x) + \exp(ik^y r + \varphi^y) + \exp(-ik^y r - \varphi^y) \quad (3.5)$$

while the probe field remains diffraction limited. In Eq. 3.5, k^x and k^y determine the period and φ^x and φ^y the phase of the fringe pattern along the *x* and *y* image axes. The structured pump field associated with SPPM is illustrated in Fig. 3.3. Panels A and B show the two sinusoidally-modulated fields produced by the interference of two counter-propagating ±1 diffraction orders in the y and x axes, respectively. When all four diffraction orders interfere at the sample plane, they produce the two-dimensional sinusoidally-modulated field shown in panel C of Fig. 3.3. The FT of the 2D excitation field is shown in panel D; it consists of nine distinct (spatial) frequency components of varying relative amplitudes. The component centered at the origin has a relative amplitude of 1, while the four components (green) located at $(+k^x, \pm k^y)$ and $(-k^x, \pm k^y)$ have relative amplitudes of 0.5, and the four components (yellow) located at $\pm 2k^x$ and $\pm 2k^y$ have relative amplitudes of 0.25.

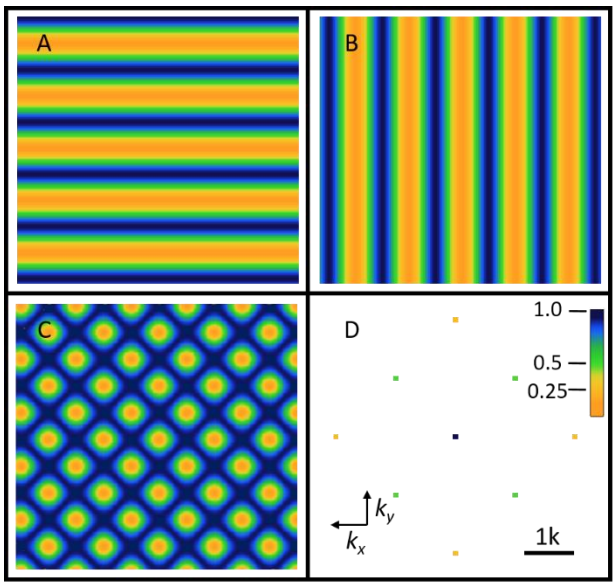

Figure 3.3. The structured excitation field employed in SPPM. (A, B) Sinusoidal fields propagating along the y- and x- axes, respectively, formed by the interference of two ±1st order diffractions. (C) Two-dimensional excitation field produced from the mutual interference of all four diffraction orders. (D) Fourier Transform of the 2D excitation field in panel C showing the nine shifted delta functions in the k_x-k_y plane. The amplitude of each component is normalized to the component centered at k_0.

Substitution of the structured pump field (Eq. 3.5) into Eq. 3.2 and Eq. 3.1 results in the structured pump-probe image (I_{Str}):

$$\begin{aligned} I_{Str}(r;\varphi^x,\varphi^y) &= o(r)\otimes\left|\begin{matrix}\exp(ik^x r+\varphi^x)+\exp(-ik^x r-\varphi^x)\\ +\exp(ik^y r+\varphi^y)+\exp(-ik^y r-\varphi^y)\end{matrix}\right|^2\cdot\left(\delta(r)\otimes h_2\right)^2 \\ &= o(r)\otimes\left|\begin{matrix}\exp(ik^x r+\varphi^x)+\exp(-ik^x r-\varphi^x)\\ +\exp(ik^y r+\varphi^y)+\exp(-ik^y r-\varphi^y)\end{matrix}\right|^2\cdot {h_2}^2 \end{aligned} \tag{3.6}$$

In Eq. 3.6, the pump PSFs vanish due to the necessary condition that the frequency components of the pump field are allowed to pass through the optical system ($k^{x,y}$ must lie within $\tilde{H}_1$). Expanding Eq. 3.6, performing the FT, and convolving the nine components

with the effective probe OTF ($\tilde{H}_2' = \tilde{H}_2 \otimes \tilde{H}_2$) the conjugate space representation of the structured image is obtained:

$$\tilde{I}_{Str}(k;\varphi^x,\varphi^y) = \tilde{O}(k)\cdot \begin{bmatrix} \left(\tilde{H}_2'(k)\right)_1 \\ +\left(\tfrac{1}{2}\tilde{H}_2'\left(k+k^x+k^y\right)e^{-i\varphi^x-i\varphi^y}\right)_2 \\ +\left(\tfrac{1}{2}\tilde{H}_2'\left(k-k^x-k^y\right)e^{+i\varphi^x+i\varphi^y}\right)_3 \\ +\left(\tfrac{1}{2}\tilde{H}_2'\left(k+k^x-k^y\right)e^{-i\varphi^x+i\varphi^y}\right)_4 \\ +\left(\tfrac{1}{2}\tilde{H}_2'\left(k-k^x+k^y\right)e^{+i\varphi^x-i\varphi^y}\right)_5 \\ +\left(\tfrac{1}{4}\tilde{H}_2'\left(k-2k^y\right)e^{+i2\varphi^y}\right)_6 + \left(\tfrac{1}{4}\tilde{H}_2'\left(k+2k^y\right)e^{-i2\varphi^y}\right)_7 \\ +\left(\tfrac{1}{4}\tilde{H}_2'\left(k-2k^x\right)e^{+i2\varphi^x}\right)_8 + \left(\tfrac{1}{4}\tilde{H}_2'\left(k+2k^x\right)e^{-i2\varphi^x}\right)_9 \end{bmatrix} \quad (3.7)$$

$$= \sum_{n=1}^{9} a_n \tilde{Y}_n \exp[\Phi_n]$$

In the first line of Eq. 3.7, the structured pump-probe image is comprised of nine components, each shifted to one of nine different positions in conjugate space. In the second line a compact notation that expresses the image as a sum over the nine terms, $\tilde{Y}_n$ is adopted. The a_n and Φ_n are the corresponding set of index-dependent amplitude and phase shifts, respectively.

3.4 SPPM Image Reconstruction

Attention is now turned to reconstructing an image with improved spatial resolution from a series of phase-shifted structured images, $I_{Str}(r)$. An ideal conjugate image with an expanded effective OTF can be written in a similar form as Eq. 3.7:

$$\tilde{I}_{ideal}(k)=\tilde{O}(k)\cdot\begin{bmatrix}\tilde{H}_2'(k)\\ +\tilde{H}_2'(k+k^x+k^y)\\ +\tilde{H}_2'(k-k^x-k^y)\\ +\tilde{H}_2'(k+k^x-k^y)\\ +\tilde{H}_2'(k-k^x+k^y)\\ +\tilde{H}_2'(k-2k^y)+\tilde{H}_2'(k+2k^y)\\ +\tilde{H}_2'(k-2k^x)+\tilde{H}_2'(k+2k^x)\end{bmatrix}$$
$$=\sum_{n=1}^{9}\tilde{Y}_n \qquad (3.8)$$

Comparison of Eq. 3.7 and Eq. 3.8 shows that the ideal conjugate image ($\tilde{I}_{ideal}(k)$) differs from the structured conjugate image ($\tilde{I}_{Str}(k;\varphi^x,\varphi^y)$) only by the relative amplitude and phase shift of each component, $\tilde{Y}_n$. It is therefore possible to reconstruct the ideal enhanced-resolution image by solving for each of the nine components present in $\tilde{I}_{Str}(k;\varphi^x,\varphi^y)$. To do so, nine structured images ($I_{str}^m(r)$, *m=1-9*) are collected, each with a uniquely phase shifted 2D pump excitation field. The FT of the nine images are arranged into a nine-component vector ($\tilde{I}_V$):

$$\tilde{I}_V=\begin{pmatrix}\tilde{I}_{Str}^1(k) & \tilde{I}_{Str}^2(k) & \cdots & \tilde{I}_{Str}^9(k)\end{pmatrix} \qquad (3.9)$$

Then a 9x9 matrix (*AP*) is constructed, which relates the amplitudes (a_n^m) and unique phase shifts (Φ_n^m), corresponding to each element of the nine structured images:

$$AP = \begin{pmatrix} a_1^1 \exp\left(\Phi_1^1\right) & \cdots & a_9^1 \exp\left(\Phi_9^1\right) \\ \vdots & \ddots & \vdots \\ a_1^9 \exp\left(\Phi_1^9\right) & \cdots & a_9^9 \exp\left(\Phi_9^9\right) \end{pmatrix} \tag{3.10}$$

The phase shifts $(\varphi^x, \varphi^y)^m$ are chosen so that *AP* is nonsingular. Then the solutions for the 9 components ($\tilde{Y}_n$) are found:

$$AP^{-1} \cdot \tilde{I}_V = \begin{pmatrix} \tilde{Y}_1 & \tilde{Y}_2 & \cdots & \tilde{Y}_9 \end{pmatrix} \tag{3.11}$$

which when summed, yield $\tilde{I}_{ideal}(k)$ (Eq. 3.8). As a final step, the conjugate image is normalized by the effective OTF:

$$OTF_{SPPM} = \begin{bmatrix} \tilde{H}_2'(k) \\ +\tilde{H}_2'(k+k^x+k^y) \\ +\tilde{H}_2'(k-k^x-k^y) \\ +\tilde{H}_2'(k+k^x-k^y) \\ +\tilde{H}_2'(k-k^x+k^y) \\ +\tilde{H}_2'(k-2k^y) \\ +\tilde{H}_2'(k+2k^y) \\ +\tilde{H}_2'(k-2k^x) \\ +\tilde{H}_2'(k+2k^x) \end{bmatrix} \tag{3.12}$$

Figure 3.4 shows a comparison of the DL, SPPM (Eq. 3.12), and final normalized OTFs. The additional high frequency information encompassed by the normalized (solid black)

and raw (black dashed) SPPM OTFs over the DL case (purple dots) is especially apparent at spatial frequencies greater than $\pm 2k^x$.

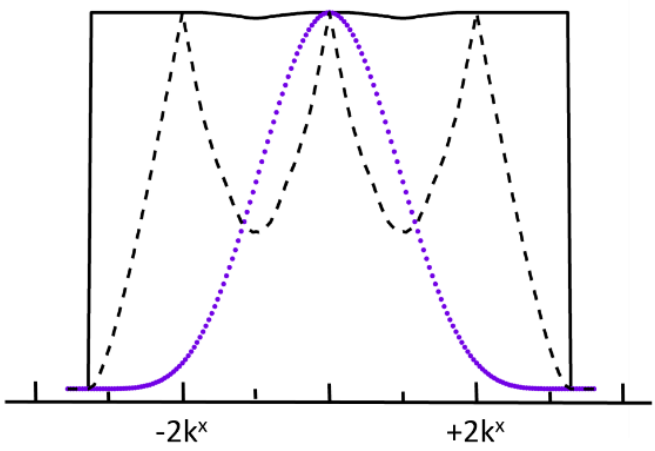

Figure 3.4. Comparison of SPPM and DL OTF profiles along the k_x axes. The diffraction-limited effective OTF (purple dots) is given by the triple convolution in Eq. 3.4. The effective SPPM OTF before normalization is shown as a black dashed line. The normalized effective OTF is shown by the solid black line.

The final SPPM image (I_{SPPM}), which contains additional high frequency information passed by the modified OTF, is obtained by Inverse FT of the summed, normalized $\tilde{Y}_n$:

$$I_{SPPM}(r) = \mathrm{Re}\left[FT^{-1}\left\{ \left(\sum_n \tilde{Y}_n \right) \div OTF_{SPPM} \right\} \right] \tag{3.13}$$

3.5 Time-Resolved SPPM

Analogously to the imaging modality, SPPM can also be utilized to collect time-resolved kinetics from a sub-diffraction limited probe volume [13]. For such a measurement, nine phase-dependent kinetics traces are collected. These traces, which measure the

decay of the sample response as a function of the pump-probe delay, Δt, are arranged into a vector equivalent to the image vector of Eq. (3.9):

$$\tilde{K}_V = \left(\tilde{K}_{Str}^1 \quad \tilde{K}_{Str}^2 \quad \cdots \quad \tilde{K}_{Str}^9 \right) \tag{3.14}$$

As before, the nine kinetics traces are collected with unique phase shifts of the pump field and a diffraction-limited probe field. Reconstruction of the kinetics data then follows the process described in Eqs. 3.10 - 3.13 with $\tilde{K}_v$ replacing $\tilde{I}_v$. Within this context, SPPM kinetics traces can be understood as a one-pixel image, collected at a series of pump-probe delays, Δt. Because the effective interrogation volume of the resultant kinetics is reduced with respect to the DL case, observables from neighboring sample domains can be more effectively deconvolved, providing a far-field approach for interrogating excited state dynamics of sub-wavelength material domains.

3.6 Results and Discussion

3.6.1 Imaging

Pump-probe measurements require two distinct laser pulses, separated by a well-defined delay, (pump and probe) to interact with the sample. Because the center wavelength of the pump and probe pulses will vary depending on the spectral response of the studied system and the photophysical process of interest, the width of the effective PSF will also necessarily vary. To understand how changes in pump and probe wavelength affect the effective PSF of SPPM, the DL and SPPM imaging linewidths of a single delta function

(Black profile in Fig. 3.5(A)) are compared while varying both pump and probe wavelengths between 400 and 800 nm. Note that for these and all subsequent results in this manuscript, a coordinate system that reproduces the imaging performance of the previously described experimental apparatus with a 0.90 NA objective has been imposed [13]. Monochromatic excitation fields have also been assumed. While ultrashort laser pulses used in pump-probe microscopy do have finite spectral bandwidth, the difference in spatial resolution between broadband and single wavelength fields is not expected to be significant [94]. Panel A of Fig. 3.5 shows examples of SPPM and DL PSFs with 400 nm pump and 540 nm probe wavelengths. For this combination of wavelengths, the PSF of SPPM has a fwhm (97 nm) that is 1.86-fold narrower than the DL case (180 nm). In Panel B, the ratio of the SPPM and DL PSFs is plotted versus the pump wavelength for a series of probe wavelengths. Overall, the SPPM PSF is narrowed by a factor of 1.69 to 1.92 over that achievable with DL imaging, suggesting significant improvements in spatial resolution can be achieved, regardless of pump or probe wavelengths. While the localization enhancement achieved by SPPM generally improves as the probe wavelength is decreased, the effective PSF narrowing is dependent on both the fringe spacing of the pump field and the width of the convolved probe OTFs. Shorter excitation wavelengths can support larger shifts in conjugate space of the of the image components ($\tilde{Y}_n$), in principle providing access to higher frequency information in the image spectrum. However, if the effective probe OTF ($\tilde{H}_2'$) is narrower than the spacing of the pump-field components, significant ringing is introduced into the reconstructed image and the PSF width can increase. Based on the 0.90 NA objective assumed in the model, the narrowest fwhm is achieved with pump and probe

wavelengths both equal to 400 nm. At these wavelengths, the SPPM PSF fwhm is 87 nm while the DL PSF fwhm is 165 nm.

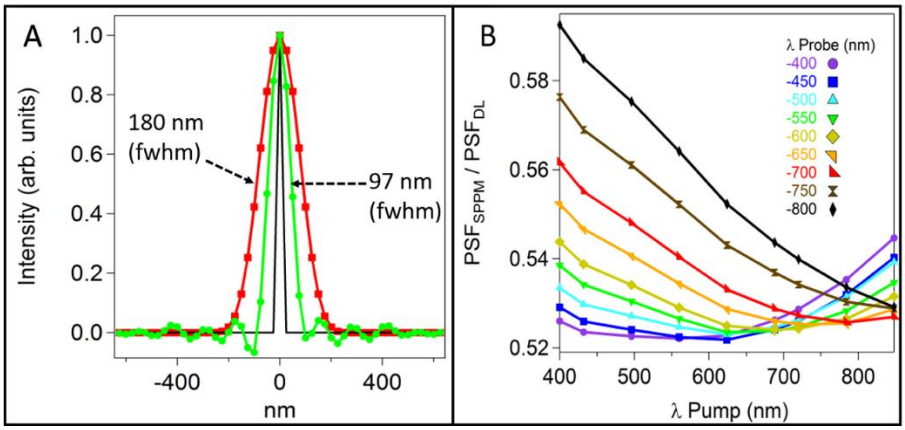

Figure 3.5. (A) Profile comparison of the simulated SPPM (green circles, 97 nm fwhm) and DL (red squares, 180 nm fwhm) effective PSFs with 400 nm pump and 540nm probe wavelengths. The black profile is the profile of the delta function used to determine the PSF of the imaging model. (B) Wavelength dependence of SPPM localization enhancement represented by the ratio of the SPPM PSF to the DL PSF at varying excitation and probe wavelengths through the visible spectrum.

Next the improvement in imaging performance is modeled by comparing DL and SPPM images of a modified 1951 USAF target shown in panel A of Fig. 3.6. The target is modified to include the group of four smallest elements oriented at 45° to study directional anisotropy in imaging performance (see below). Target imaging is modeled at two sets of pump and probe wavelengths, with a pump/probe wavelength ratio of 0.8.

Panels B and C of Fig. 3.6 show the image produced with DL and SPPM models, respectively, with 432 nm pump and 540 nm probe wavelengths. In contrast to DL imaging, the SPPM image in panel C clearly resolves even the smallest components on the target. Panel D compares the profiles from DL and SPPM methods to the ideal target profile along the red-dashed line in the magnified subsection of panel A. Along this profile the spatial

period of the target elements (~ 237 nm) is approximately a factor of two shorter than the structured pump fringe pattern period (~ 450 nm). Panels E, F show equivalent images when 784 nm pump and 980 nm probe wavelengths are utilized for both the DL and SPPM models. Again, the profiles in panel G are taken from the location indicated by the red-dashed line in Panel A. In this case, while neither DL or SPPM resolves the features as they are nearly a factor of three below the diffraction limit, the SPPM approach does improve the contrast of the group relative to background and produces relatively little image distortion.

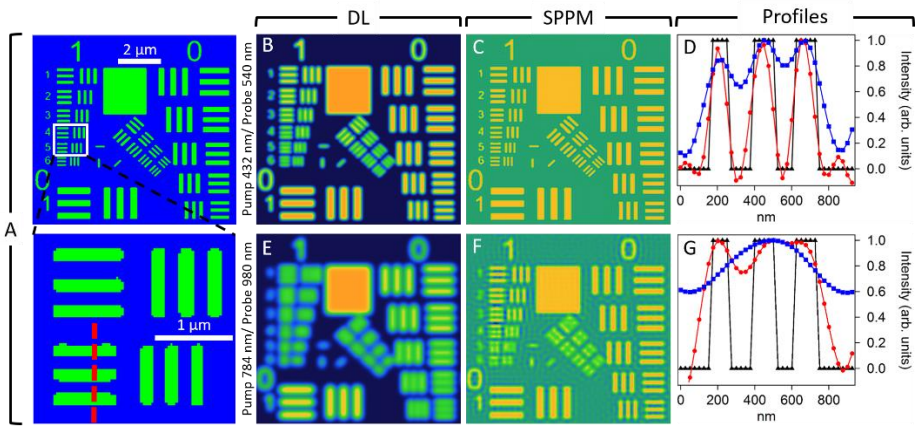

Figure 3.6. Comparison of simulated DL and SPPM imaging capabilities. (A) Shows the simulated test target (top) with a magnified region (bottom) designated by the white square. The remaining panels (B-G) are arranged so that the top and bottom rows correspond to the modeled wavelengths (labeled to the left of panels B and E). The three separate columns of panels B-G show DL (B, E), SPPM (C, F) imaging models and profile comparisons (D, G). Profile comparison are from location indicated by the red dashed line in the magnified region of panel A. The black (triangles) trace represents the original object while the blue (squares) and red (circles) traces are the DL and the SPPM models, respectively.

Although the width of the SPPM PSF is nearly half that of DL imaging regardless of pump and probe wavelength, imaging performance along the diagonal is reduced relative to along the x or y axes. This anisotropy stems from the shape of the SPPM OTF. Panel D in Fig. 3.3 shows that along the k_x and k_y axes, image components ($\tilde{Y}_n$) are shifted to $\pm 2k^x$ and $\pm 2k^y$, however the diagonal components are only shifted away from the center by $\pm\sqrt{2}k^{xy}$. Because the components are not shifted as far, the effective OTF is narrowed along the diagonal, resulting in lower image resolution. These effects are illustrated in Fig. 3.7, where panel A shows the target described in Fig. 3.6 imaged with the SPPM model at 560 nm pump and 800 nm probe wavelengths, and panel B shows the associated two-dimensional SPPM PSF.

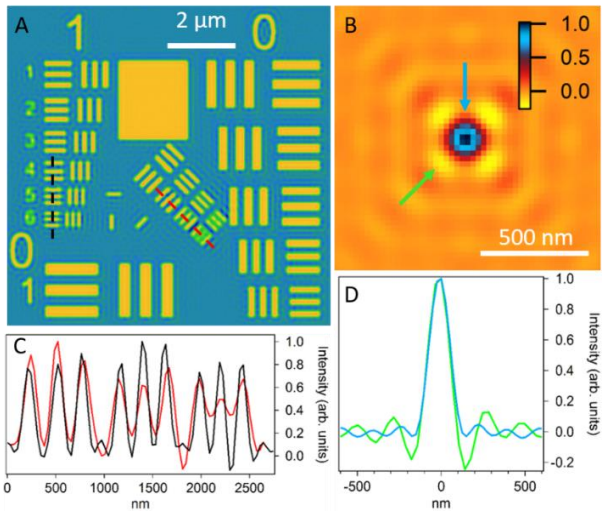

Figure 3.7. Evaluation of the vertical and diagonal features of the simulated SPPM OTF. (A) The object described in panel A of Fig. 6 imaged using the SPPM model (560 nm pump, 800 nm probe). (B) The resulting PSF generated by the SPPM model. (C) The black and red traces correspond to the red and black dashed lines in panel A. The nine components are identical in the original image. However, the nine components that produce the red trace in panel C have been rotated 45°. (D) Profile comparison of the SPPM PSF along directions of the blue and green arrows in panel B.

Panel D illustrates that the while the narrowing of the SPPM OTF along the diagonal does not significantly change the width of the PSF, it does increase the magnitude of ringing present. Such ringing can significantly impact imaging performance as highlighted in panel C. Here, profiles collected from the red and black dashed lines on panel A are compared. The nine components profiled by the red trace are identical to the nine components corresponding to the black trace but are rotated 45°. For the smallest group of three, the decrease in spatial resolution is especially clear, illustrating the importance of mitigating PSF ringing for both imaging and spectroscopic applications.

3.6.2 Sub-Diffraction Limited Spectroscopy

While SPPM can be employed exclusively for enhanced resolution imaging, it also provides the ability to perform ultrafast spectroscopy of sub-diffraction limited sample volumes [13]. Figure 3.8 models the time-resolved capabilities of SPPM as described in Section 3.5 and experimentally demonstrated in chapter 2. Here, the decay kinetics recovered using DL and SPPM approaches are compared from two single-pixel features (black profiles), one with a single exponential lifetime of 100 ps and the other with a longer lifetime of 200 ps. The left column of Fig. 3.8(A-C) shows $\Delta t = 0$ ps images while the right column shows the time-dependent kinetics obtained with DL (Panel A) and SPPM (panels B, C) models. In panel A, the DL approach does not resolve the two features and consequently recovers decay kinetics that are an average of the short and long-lived components. Panel B shows that the SPPM model spatially distinguishes the two objects and recovers decay dynamics that accurately reflect the distinct lifetimes of the objects. When the two objects

are spaced more closely (panel C, 125 nm) so that they are no longer resolved with SPPM, the recovered kinetics reflect an average of the fast and slow components as in the DL case.

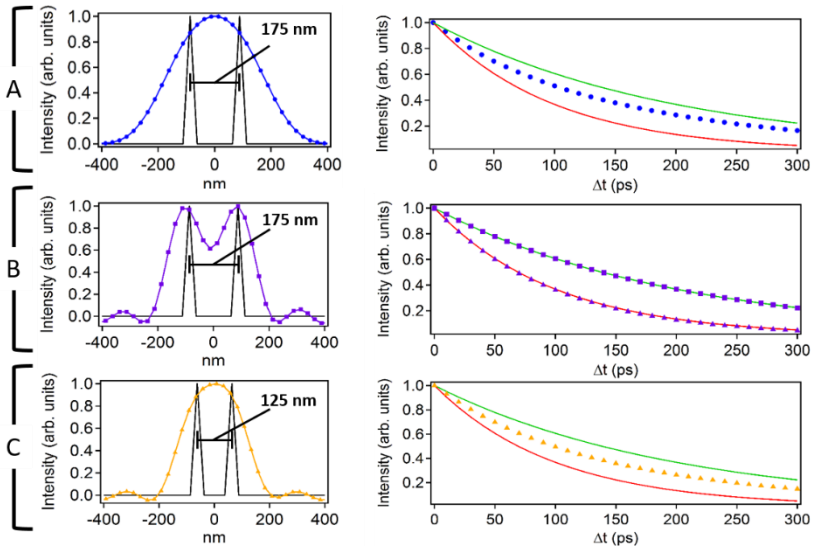

Figure 3.8. Comparison of Δt = 0 ps images (*left*) and time-resolved kinetics (*right*) of modeled single pixel features using simulated DL and SPPM approaches. Simulated pump wavelength is 560 nm and probe wavelength is 800 nm. The amplitude of the feature located to the left of the origin decays with a single exponential lifetime of 100 ps (red, solid line), whereas the feature to the right decays with a lifetime of 200 ps (green, solid line). (A) DL decay kinetics (blue circles) reflect an average of the fast and slow components with an object spacing of 175 nm. (B) The SPPM model recovers the distinct kinetics of the two objects (purple squares and triangles) when separated by 175 nm. (C) If the objects are unresolvable with SPPM, the recovered kinetics (orange triangles) reflect the average of fast and slow decays. For all panels, the kinetics are collected at the peak location(s) of the lineshape at Δt = 0 ps.

3.7 Summary

Chapters 2 and 3 demonstrate SPPM as a route for achieving far-field, label-free super resolution spectroscopies. The theoretical basis for achieving increased resolution has been provided and several limitations of the approach have been examined. While the structured

excitation field and diffraction limited probe field utilized in SPPM produces a nearly 2-fold enhancement over the diffraction limit, further improvements will require additional approaches. Possible routes toward far-field spatial resolution below 100 nm include utilizing higher-order nonlinear processes such as two photon absorption, implementing total internal reflection geometries, or saturation of the absorption process (described in chapter 4). This work was performed in the hope that sub-diffraction limited spectroscopies like SPPM will continue to enhance the current understanding of complex materials systems by distinguishing the contributions of nanoscale heterogeneities and improving characterization of emergent functionality.

3.8 Acknowledgements

This work was funded by the Division of Chemical Sciences, Geosciences, and Biosciences, Office of Basic Energy Sciences of the U.S. Department of Energy (DOE) (DE-SC0014128).

CHAPTER FOUR

LABEL-FREE SATURATED STRUCTURED EXCITATION MICROSCOPY

Contribution of Authors and Co-Authors

Manuscript in Chapter 4

Author: Eric S. Massaro

Contributions: Performed theoretical development of LF-SSEM. Generated figures and prepared the manuscript for submission.

Co-Author: Erik M. Grumstrup

Contributions: Performed theoretical development of LF-SSEM and co-wrote manuscript.

Manuscript Information Page

Eric S. Massaro, and Erik M. Grumstrup

Photonics

Status of Manuscript:
____ Prepared for submission to a peer-reviewed journal
____ Officially submitted to a peer-review journal
____ Accepted by a peer-reviewed journal
__X_ Published in a peer-reviewed journal

Published by the Multidisciplinary Digital Publishing Institute
Photonics 2017, Vol. 4, No. 36

LABEL-FREE SATURATED STRUCTURED EXCITATION MICROSCOPY

The following (adapted) work has been published in Photonics

Eric S. Massaro[1], and Erik M. Grumstrup[1, 2]

1. Department of Chemistry and Biochemistry, Montana State University, Bozeman, Montana 59717, United States
2. Montana Materials Science Program, Montana State University, Bozeman, Montana 59717, United States

4.1 Introduction

In previous chapters, the theoretical basis of Laterally Modulated Excitation Microscopy [6] was leveraged to develop SPPM, which provides a factor of two improvement in spatial resolution without relying on high-intensity saturation or de-excitation phenomena [11,12]. However, to achieve higher imaging resolution with a structured excitation field, it is necessary to invoke higher order nonlinear light-matter interactions [13,14]. Herein, the impact of saturated structured excitation on label-free coherent third-order nonlinear optical microscopy techniques including PPM and Stimulated Raman Microscopy (SRM) is described. Label-Free Saturated Structured Excitation Microscopy (LF-SSEM) exploits the nonlinear saturation of the excitation process in conjunction with a structured excitation field to collect high spatial frequency information that would otherwise not pass through the optical system. In the remainder of this chapter, the imaging theory of LF-SSEM is described and a factor of six improvement in resolution over the diffraction limit

is theoretically demonstrated, corresponding to a point spread function of ~33 nm with a 400-nm excitation wavelength.

4.2 Methods

4.2.1. Structured Excitation in One Dimension

Imaging with conventional nonlinear scanning microscopies utilizes point-focused excitation and probe beams at the sample plane [7-9, 91]. LF-SSEM replaces the DL excitation beam with a structured excitation field in the same way as SPPM [12, 13]. The structured excitation enables the collection of additional high spatial frequency information that would otherwise be attenuated by the optical system. In the case of one dimensional structured excitation, the field E_1 in Eq. 3.5. is given by a sinusoidally modulated excitation profile:

$$E_1(x) = \frac{1}{2}\left[\exp(ik^x x + i\varphi^x) + \exp(-ik^x x - i\varphi^x)\right] \tag{4.1}$$

where k^x and φ^x give the period and phase, respectively, of the excitation field propagating along the *x*-axis. Replacing the DL excitation pulse ($E_1(x)$) of Eq. 3.3 ($I_{DL} = o(x) \otimes \left|E_1(x) \otimes h_1\right|^2 \cdot \left|E_2(x) \otimes h_2\right|^2$) with the structured excitation field in Eq. 4.1 results in the collection of a structured image (I_{Str}):

$$I_{Str}(x;\varphi^x) = o(x) \otimes \left(\frac{1}{2}\left[\exp(ik^x x + i\varphi^x) + \exp(-ik^x x - i\varphi^x)\right]\right)^2 \cdot {h_2}^2 \tag{4.2}$$

that is dependent on the period and phase of the excitation profile. The excitation pulse PSF is eliminated from Eq. 4.2 due to the necessary condition that the spatial frequency of the excitation profile falls within the bounds of the optical transfer function of the imaging system. Under conditions where the excitation density scales linearly with the pump power (low fluence), a series of structured images collected using a structured excitation field as defined by Eq. 4.2 can be utilized to reconstruct an image with a factor of two improvement in spatial resolution over the diffraction limit (chapter 2, and 3) [11,12].

4.2.2 Saturated Excitation

To increase the resolution of SPPM beyond a two-fold improvement, a nonlinear excitation process must be exploited. One such nonlinear interaction is saturated excitation which can be expressed as:

$$Exc_{Sat} = 1 - exp\left[-n \cdot \left(E_1(x) \right)^2 \right] \tag{4.3}$$

where $E_1(x)$ is the structured excitation field in Eq. 4.1 and *n* is an effective scaling factor that determines the extent of nonlinearity in the excitation process [14]. As shown in Panel A of Fig. 4.1, linear excitation occurs for small values of *n* ($n << 1$), while for larger values of *n*, the excitation process becomes increasingly saturated. The black (circles), red (squares), green (triangles) and blue (diamonds) traces of Panel B in Fig. 4.1 show the excitation profiles for increasing values of *n.* To account for the nonlinear excitation profile in the structured image, Eq. 4.2 must be modified with the new field expression given by Eq. 4.3.

$$I_{Str}(x;\varphi^x) = o(x) \otimes Exc_{Sat} \cdot h_2^{\,2} \tag{4.4}$$

The expansion of Eq. 4.3 and truncation of the series after the fourth-order term gives:

$$\begin{aligned} Exc_{Sat} &= 1 - exp\left[-n \cdot \left(E_1(x)\right)^2\right] \\ &= 1 - \sum_k^{\infty} \frac{\left(-n \cdot \left(E_1(x)\right)^2\right)^k}{k!} \\ &\approx \left[n \cdot \left(E_1(x)\right)^2\right]_1 - \left[\frac{\left(-n \cdot \left(E_1(x)\right)^2\right)^2}{2}\right]_2 + \left[\frac{\left(n \cdot \left(E_1(x)\right)^2\right)^3}{6}\right]_3 - \left[\frac{\left(n \cdot \left(E_1(x)\right)^2\right)^4}{24}\right]_4 \end{aligned} \tag{4.5}$$

where each term in square brackets is labeled with an index indicating the order of the light-matter interaction. Fourier transform of each of the four terms in Eq. 4.5 produces frequency components located at increasing intervals of $\pm 2k^x$ in conjugate space. The first (linear) term is comprised of components at $k = \pm 2k^x$ (as well as at $k = 0$), while the second-order term has components at $k = \pm 4k^x$ (and $\pm 2k^x$, 0), etc. By truncating the series at the fourth-order term, the analysis is limited to Fourier components up to $k = \pm 8k^x$. Panel C of Fig. 4.1 shows the Fourier components of the excitation field up to $k = \pm 8k^x$ for $n = 1$. In Panel D of Fig. 4.1, the relative amplitudes of the linear and nonlinear Fourier components are shown as n is increased. While the nonlinear terms are weak relative to the linear terms, image formation that exploits higher order Fourier components will benefit from lock-in detection often utilized with third-order imaging techniques [15].

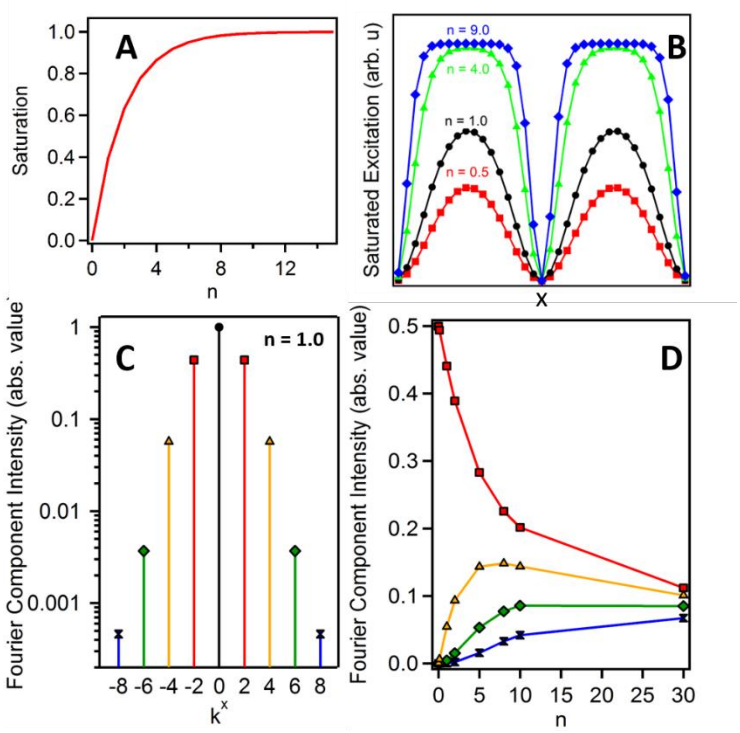

Figure 4.1. Label-free saturated structured excitation microscopy (LF-SSEM) saturation effects. (A) Nonlinear relationship of the excitation fluence (*n*) and saturation of the excitation process. (B) Effective excitation density at the sample plane as the extent of saturation is increased. (C) Normalized relative amplitude of nine Fourier components produced from an excitation profile given by the black (circle) trace in Panel B. (D) Relationship of Fourier component amplitude and effective excitation fluence. The colors and markers of Panel D correspond to the components of Panel C.

4.2.3 Image Reconstruction

As illustrated in Panel C of Fig. 4.1, the saturation of the excitation process increases the number of Fourier components that contribute to image formation. The key to reconstructing an image with increased spatial resolution is to collect a series of images in which the phase of the excitation field is shifted by a known interval at the sample plane. Work reported in chapters 2 and 3 described the process of image reconstruction under

linear excitation conditions [11,12]. Image reconstruction under nonlinear excitation conditions is entirely analogous to the linear case, with the exception that additional phase-shifted structured images must be collected to enable unique identification of the additional frequency components present in the collected images.

Once collected, the vector of *m* individual Fourier components, $\tilde{U}_m$ (analogous to $\tilde{Y}_n$ in Eq. 3.11), are determined by solving the linear system given by:

$$\tilde{M}^{-1} \cdot \tilde{I}_m = \tilde{U}_m \ . \tag{4.6}$$

Here, $\tilde{M}^{-1}$ is the inverted $m \times m$ matrix of amplitude and phase information encoded by the excitation field, and $\tilde{I}_m$ is the *m*-length vector of conjugate space structured images (see also Eqs. 3.10 – 3.13) collected under saturated excitation conditions [12]. Summing the *m* components of $\tilde{U}_m$ yields the total reconstructed conjugate space image.

Figure 4.2 presents the effective LF-SSEM OTF when utilizing Fourier components up to k = $\pm 2k^x$ (red; squares), $\pm 4k^x$ (blue; triangles), $\pm 6k^x$ (green; diamonds), and $\pm 8k^x$ (yellow; hourglass). The red dashed trace shows the raw reconstructed linear regime OTF before amplitude normalization by the ideal OTF [12]. As the OTF effectively acts as a low-pass (spatial) frequency filter, expanding it through LF-SSEM provides access to higher spatial frequency information than that which is transmitted in the DL case (black trace).

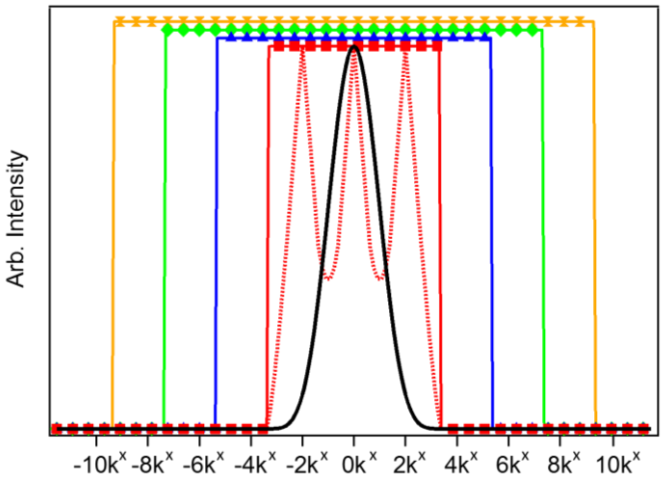

Figure 4.2. Comparison of simulated LF-SSEM optical transfer functions (OTFs) with utilization of higher order Fourier components. The black trace shows the diffraction-limited (DL) OTF. The red traces show the initial OTF (dashed) produced by image reconstruction and the final OTF (squares) trace after amplitude normalization when including only first-order (linear) Fourier components. Blue (triangles), green (diamonds) and yellow (hourglasses) traces represent the normalized OTFs when incorporating the $k = \pm 4k^x$, $\pm 6k^x$ and $\pm 8k^x$ components, respectively. Note that the higher order OTFs are renormalized to an amplitude larger than 1.0 for visibility.

4.3 Results

4.3.1 PSF Comparison

The improvement to the LF-SSEM PSF is summarized in Fig. 4.3, where the DL and LF-SSEM images of a single point source are compared. The coordinate system was defined to be consistent with chapters 2 and 3, corresponding to a 0.9 NA objective and pump/probe wavelength ratio of 0.87 [11]. Panel A of Fig. 4.3 compares the PSFs of the LF-SSEM model (red squares; green circles) to the DL case (black dashed) with the fwhm of the DL model normalized to 1. The PSF indicated by the red squares includes only the linear Fourier components (OTF defined by red squares in Fig. 4.2), whereas the green

circles indicate the resultant PSF if all Fourier components up to k = ±8k^x are included (yellow OTF in Fig. 4.2). Because the inclusion of higher order Fourier components in the construction of the image provides access to higher spatial frequency information in the conjugate image, the PSF is significantly narrower in the real-space image. Panel B summarizes this effect by plotting the fwhm of each PSF as increasingly higher order components are included in the image formation. The most significant reduction in width occurs after the inclusion of the linear components at k = ±2k^x, however, if all components up to the fourth-order term are included, the PSF can be reduced in width by more than a factor of six. As a best-case scenario with $\lambda_{excitation}$ = 400 nm and λ_{probe} = 400 nm, these results indicate that the PSF will have a width of only 33.4 nm. The LF-SSEM PSFs shown in Panel A of Fig. 4.3 exhibit ringing outward from the center peak. The oscillatory ringing results from the Fourier transform of the sharp-edged OTF functions are shown in Fig. 4.2. By smoothing the high-frequency edges of the OTF, the ringing can be mitigated, although at the cost of a wider PSF.

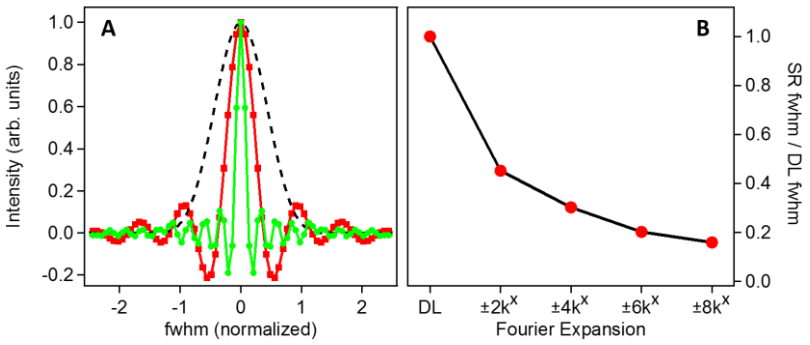

Figure 4.3. (A) Profile comparison of the simulated DL and LF-SSEM model point spread functions (PSFs). The black dashed trace is the DL model with the fwhm normalized to 1. The red (squares) and green (circles) traces show LF-SSEM PSFs including Fourier components up to k = ±2k^x and k = ±8k^x, respectively. (B) Reduction of the optical PSF fwhm with the inclusion of higher order Fourier components.

4.3.2 Imaging Capabilities

Next, the imaging capabilities of LF-SSEM are modeled using a simulated grating structure with line widths decreasing from 180 nm to 30 nm. The excitation and probe wavelengths were 784 nm and 900 nm, respectively, corresponding to a DL PSF fwhm of 432.2 nm. Panel A of Fig. 4.4 shows the simulated target and Panel B shows the image produced by the DL model. The LF-SSEM images in Panel C, which includes Fourier components up to $k = \pm 2k^x$, and Panel D, which includes Fourier components up to $k = \pm 8k^x$, have significantly improved resolutions relative to the DL case. The enhanced resolution can be seen more clearly in Panels F, G, and H, where the profiles of the images are compared. For the DL case (Panel F; red), even the largest features of the target image (black) remain unresolved. On the other hand, LF-SSEM models (Panel G and H) resolve components spaced far below the diffraction limit. If Fourier components up to the fourth-order are included (Panel H), LF-SSEM resolves features spaced only 60.2 nm apart, representing an approximate factor of six improvement in spatial resolution. Two artifacts of the LF-SSEM approach, both a consequence of the PSF ringing discussed above, can be seen in Panel H. The first is a negative offset that spans the image from approximately 0.5–5 μm. This offset arises from the negative amplitude ringing in the PSF (see Fig. 4.3-A), which constructively interferes for two neighboring object features. The second artifact takes the form of the low-amplitude peaks near 4.0 μm. Again, these peaks can be understood as interference of the neighboring grating features after convolution with the LF-SSEM PSF. In this case, because the relative spacing of the object features is larger, the ringing interferes differently, manifesting in the small specious peaks.

While LF-SSEM is modeled in one-dimension, multi-dimensional resolution enhancement can be approached in two ways. First, as has been demonstrated [14] in fluorescence imaging, full radial super-resolution can be achieved by collecting patterned images with a one-dimensional excitation pattern, rotated through a series of angles around the axis normal to the sample plane. Rotating the image in such a manner is straightforward using modern pulse shaping technologies such as spatial light modulators or digital micromirror devices. The second approach requires a two-dimensional structured excitation profile, which resembles a two-dimensional diffraction pattern [13]. While no pattern rotation is necessary in this case, each Fourier component must be isolated with a unique phase, a requirement that introduces additional experimental and image-processing difficulties. To provide perspective as to how rapidly the number of required images increases with increasing dimensionality and saturation, the use of a sequential one-dimensional structured excitation performed using pattern rotation steps of $\pi/6$ to reach full radial resolution enhancement is assumed. In order to produce a two-fold resolution in the linear excitation regime, 18 images would be needed to solve the system of linear equations during reconstruction. To produce a four-fold increase in resolution (corresponding to the nonlinear expansion of Fourier components up to $\pm 6k^x$), 42 images would be required. Note that the number of images described above can be reduced by approximately a factor of two as the Fourier components shifted to opposite signs (i.e., $\pm 6k^x$) contain redundant information (i.e., they are complex conjugates of one another), however, the imaging process is still experimentally demanding.

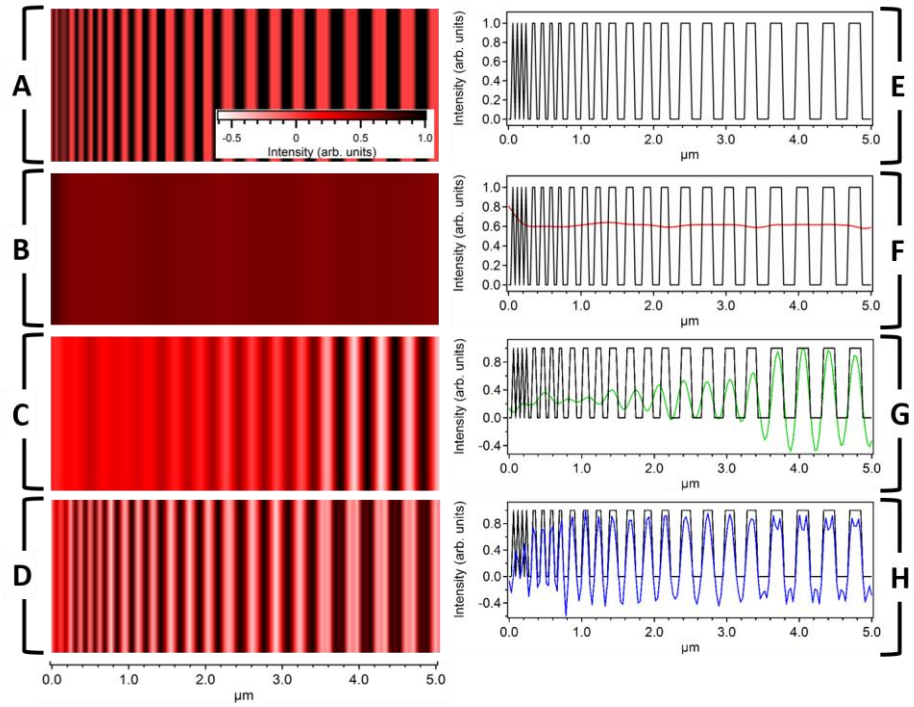

Figure 4.4. Imaging a one-dimensional grating using both DL and LF-SSEM simulation models. (A) Simulated target image with individual component dimensions ranging from 30 nm to 180 nm. (B–D) Images produced by using the DL model (B) and the LF-SSEM model (C, D). Panels C and D show images determined using the LF-SSEM model with Fourier expansions of $\pm 2k^x$ and $\pm 8k^x$, respectively. (E–H) Profile comparisons of the three separate images in Panels B (red), C (green), and D (blue). The length scale below Panel D applies to all images in the left column and corresponds to the individual truncated length scales in the right column. The color scale in Panel A corresponds to Panels A–D.

4.3.3 Signal-to-Noise Ratio Dependence

Thus far, the LF-SSEM approach is modeled assuming an ideal imaging system to produce resolution enhancement without regard to noise present in experimental applications. However, in practice, noise will prevent isolation of the low-amplitude, higher order Fourier components. In Fig. 4.5 modeled results are shown of the imaging process while including random noise with a uniform probability distribution. Panel A shows a profile comparison of the structured image spectrum at varying SNRs. Excitation fluence was held

constant at a level capable of producing a Fourier expansion up to $\pm 6k^x$. When the SNR is high (10,000:1), all seven Fourier components rise above the noise level. However, when the SNR is low (100:1 and 25:1), fewer Fourier components are distinguishable above the noise threshold. Panel B shows the profile comparison of the PSFs resulting from the corresponding SNR of Panel A. If the higher order Fourier component has a negligible amplitude relative to the noise level, the OTF expansion is limited during image reconstruction. At an SNR of 10,000:1 the OTF was expanded to $\pm 6k^x$, while SNRs of 100:1 and 25:1 only allowed for the OTF expansion of $\pm 4k^x$ and $\pm 2k^x$, respectively. In practice, both the high order Fourier component amplitudes and the SNR can be increased by increasing the pump fluence, provided the sample is robust to high excitation levels.

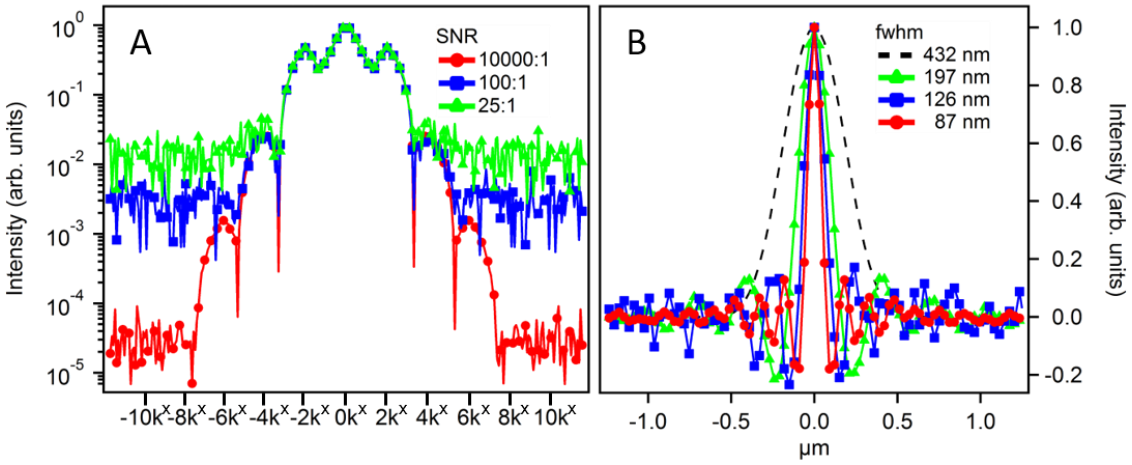

Figure 4.5. SNR-dependent LF-SSEM image reconstruction simulation using 784 nm excitation and 900 nm probe wavelengths. Panel A shows the profiles of three structured image spectra with varying SNRs given in the legend. Panel B shows the resulting PSF of the optical system after image reconstruction using Fourier components that exceeded the SNR. The DL model shows a FWHM of 432 nm. The green (triangles), blue (squares) and red (circles) show the PSF resulting from the use of $\pm 2k^x$, $\pm 4k^x$ and $\pm 6k^x$ Fourier expansions, respectively.

4.4 Conclusions

The resolution enhancement of LF-SSEM has been demonstrated when the saturation of the excitation process allows for the collection of higher order nonlinear spatial frequency components. The results presented here suggest that PSFs as narrow as ~33 nm can be achieved if Fourier components up to the fourth-order are included in the image formation. However, LF-SSEM is capable of achieving even greater resolution enhancement provided the optical configuration has a low noise threshold. The approach outlined for LF-SSEM can be readily applied to related nonlinear imaging techniques such as SRM and PPM, which share a common electric field and phase-matching dependence. Further advancements of LF-SSEM will seek to demonstrate experimental viability and determine which multidimensional approach is experimentally preferable. Further advancement will allow LF-SSEM and related far-field super-resolution microscopies to become viable alternatives to near-field characterization techniques for nanoscale materials systems.

4.5 Acknowledgments

This work was funded by the Division of Chemical Sciences, Geosciences, and Biosciences, Office of Basic Energy Sciences of the U.S. Department of Energy through Grant DE-SC0014128.

CHAPTER FIVE

EXCEPTIONALLY FAST NANOSCALE EXCITON DIFFUSION IN DONOR-ACCEPTOR POLYMER THIN FILMS

Contribution of Authors and Co-Authors

Manuscript in Chapter 5

Author: Eric S. Massaro

Contributions: Performed all experimental data collection of exciton diffusion in PCDTBT thin films, developed Monte Carlo simulations, and performed macroscopic alignment of polymer chains. Co-wrote the manuscript.

Co-Author: Erik M. Grumstrup

Contributions: Developed experimental design, co-developed Monte Carlo simulations, and co-wrote manuscript.

Manuscript Information Page

Eric S. Massaro and Erik M. Grumstrup

Status of Manuscript:
__X__ Prepared for submission to a peer-reviewed journal
____ Officially submitted to a peer-review journal
____ Accepted by a peer-reviewed journal
____ Published in a peer-reviewed journal

EXCEPTIONALLY FAST NANOSCALE EXCITON DIFFUSION IN PCDTBT THIN FILMS

*Eric S. Massaro[1] and Erik M. Grumstrup[1, 2]**

1. Department of Chemistry and Biochemistry, Montana State University, Bozeman, Montana 59717, United States
2. Montana Materials Science Program, Montana State University, Bozeman, Montana 59717, United States

5.1 Introduction

Organic semiconducting polymers (OSPs) are cost effective, solution processable materials that have proven to be useful in a variety of optoelectronic applications [25-27, 95]. However, the morphological heterogeneity of OSPs complicates the interpretation of bulk spectroscopic data with respect to structure-function relationships, inherent material properties, and potential routes for material improvement [96, 97]. Additionally, the excited state dynamics of OSPs differ from traditional inorganic semiconductors. Due to the low dielectric constant of OSPs ($\varepsilon \sim 3$), coulombically bound electron hole pairs, or excitons, are the primary species following photoexcitation [29, 33, 50, 55]. The neutral charge of the exciton makes energy conversion impossible without complete exciton dissociation. For dissociation to occur, the exciton must migrate from the initial point of photoexcitation to a donor-acceptor (DA) interface to efficiently dissociate into free carriers and contribute to the overall efficiency of OSP based photovoltaics [98]. In opposition, exciton diffusion

through polymer networks is believed to be efficient only over short (< 20 nm) length scales [33].

In an attempt to improve the transport and dissociation of self-localized states, a new collection of polymers has been developed utilizing donor and acceptor fragments within the repeat unit of the polymer [58]. This class of polymers, broadly termed push-pull copolymers, has demonstrated increased excited state transport rates compared to classical OSPs [99-101] and has enabled the development of polymer only organic photovoltaics (OPVs) [102, 103].

Specifically, the copolymer poly [N-9’’-hepta-decanyl-2,7-carbazole-alt-5,5-(4’,7’-di-2-thienyl-2’,1’,3’-benzothiadiazole)] (PCDTBT) has proven to be a cost-effective material for solution processed OPV devices with photoconversion efficiencies (PCEs) reaching 7.8%, operational lifetimes up to 6200 hours and theoretical operational lifetimes extending to 15 years [25, 27, 62, 98, 104]. Still, a complete understanding of exciton transport in PCDTBT remains clouded by complex morphological heterogeneity stemming from the amorphous nature of the polymer. For example, photoluminescent quenching (PLQ) experiments have reported exciton diffusivity on the order of 10^{-4} cm^2/s in PCDTBT. However, recent experimental and theoretical reports suggest that excited state diffusion is significantly faster at microscopic length scales due to increased energy of photo-generated states [105, 106], coherent migration [107-109], and macroscopic polymer alignment [100, 110-112].

In this chapter PPM is used as a microscopic probe to show that for some microscopic domains in bulk PCDTBT thin films, exceptionally high diffusion constants can be

observed [6, 7]. Exciton diffusivities averaging 2 – 3 orders of magnitude higher than previous bulk measurements are reported in this chapter [113]. Macroscopic alignment of PCDTBT polymer chains shows that the high diffusion constants are likely related to localized polymer ordering in the bulk film [112, 114]. Finally, a Monte Carlo (MC) simulation is developed to demonstrate the effects of polymer alignment, intra- vs interchain hopping rates and hopping distance that indicates excitons are highly delocalized along individual polymer chains and that the effective hopping distance and rate exceed what is predicted by Förster resonance energy transfer (FRET) theory. The experimental and theoretical results reported within this chapter will assist in the intelligent design of next generation OSPs and organic optoelectronics [28, 115].

5.2 Results and Discussion

5.2.1 Ground and Excited State Spectroscopy

PCDTBT thin films were photoexcited at 600 nm (generated using a photonic crystal fiber) corresponding to states ~ 45 nm redshifted from the maximum of the broad low energy absorption band that spans 530 - 580 nm. This resonance has been previously assigned to a partial charge transfer sate between the 2,7-di(thien-2-yl)carbazole and adjacent benzothiadiazole units [59]. Steady state absorption (solid) and emission (dashed) spectra of PCDTBT thin films are displayed in panel A of Fig. 5.1. Similar to a wide range of OSP systems, the small dielectric constant of PCDTBT implies that excitons are the dominant excited state species for pump-probe delay times greater than ~ 1 ps [50, 55]. To probe

exciton dynamics, the probe pulse is tuned to 850 nm, which is resonant with a broad transient band associated with exciton absorption [56].

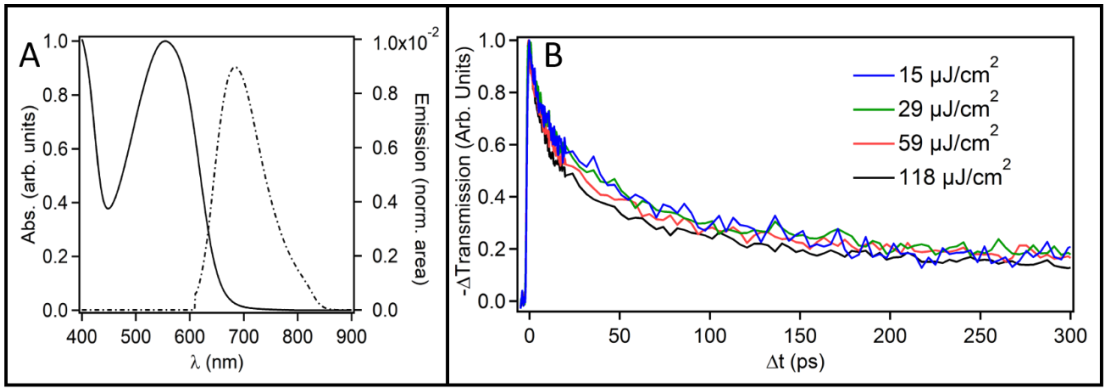

Figure. 5.1. Steady state characterization and excited state decay kinetics of PCDTBT thin films. (A) Absorption (solid) and emission (dashed) spectra of amorphous PCDTBT thin films. This data will be discussed further in Fig. 5.3. (B) Time dependent kinetics of exciton lifetime probed in a near diffraction limited volume of PCDTBT thin film following 600 nm excitation at fluences ranging one order of magnitude.

Transient decay kinetics were collected at 19 locations over two dropcast PCDTBT thin films. Panel B in Fig. 5.1 shows the typical kinetics of the photoinduced absorption (PIA) at λ_{probe} = 850 nm for a range of pump powers between 15 and 118 μJ/cm^2. Below 29 μJ/cm^2, the kinetics are invariant with respect to fluence, showing that nonlinear recombination (i.e. exciton-exciton annihilation) does not contribute to the time-varying optical response of the polymer thin film. The decay dynamics of the PIA scale linearly with pump power and show good qualitative agreement with previous ultrafast studies of PCDTBT thin films [55, 56]. At all locations, the transient kinetics can be well fit to a biexponential (plus offset) model. The fast component (τ_1 ~ 15 - 25 ps, A_1 ~ 0.4-0.5) and second slower component (τ_2 ~ 150 - 230 ps, A_2 ~ 0.4 - 0.5) are similar to values previously reported for

PCDTBT thin films [55, 59, 116]. These two rates of exciton relaxation represent contributions from both intra and interchain relaxation mechanisms while τ_2 most likely corresponds to exciton diffusion toward regions of increased polymer order [59]. The unresolved offset comprises ~ 10% of the overall signal. While kinetics collected at all locations are qualitatively similar, a range of lifetimes and amplitudes is reported because a direct comparison of kinetics collected at different sub-micron locations shows that significant variations in decay kinetics are present on the same film. These location-to-location differences in excited state lifetime strongly suggests that each film is comprised of microscopic domains that exhibit different excitonic dynamics, a result that is not observed when performing ensemble ultrafast measurements which only provide the spatially averaged film response. As will be discussed below, site-to-site variation is also observed in the transport properties of the films.

5.2.2 Exciton Transport in Amorphous PCDTBT Thin Films

To measure exciton transport in the polymer thin films, spatially separated PPM is used to directly image the spatial evolution of the excited state as a function of the pump-probe delay [7, 117]. Panels A and B of Fig. 5.2 show typical excited state distribution images at pump-probe delay times (Δt) of 1 ps and 200 ps, respectively, collected by spatially convolving the pump and probe pulses. By integrating the images in panels A and B (as well as images collected at other time points) along the y-axis, the one-dimensional distribution profile of the exciton density is found, whose increasing widths (with time) reflect exciton diffusion through the film. Each density profile can be fit with a Gaussian function whose time dependent full width at half maximum (fwhm), $\beta(t)$, is given by,

$$\beta(\Delta t) = \left[\beta(t_0)^2 + 16\ln(2) D_c \left(\Delta t - t_0 \right) \right]^{1/2} \tag{5.1}$$

Here $\beta(t_0)^2$ is the square of the fwhm when $\Delta t = t_0 =$ 1 ps and D_c is the local diffusion constant of the material [35, 36]. In the limit of diffusive motion, plotting $\beta(\Delta t)^2 - \beta(t_0)^2$ as a function of pump-probe delay time produces a linear relationship with a slope that is proportional to D_c as shown in panel C of Fig. 5.2. Because the diffusion constant is determined by the slope of the line in panel D of Fig. 5.2, the resolution of the instrument is not limited by the spot size of the pump and probe laser pulses, but rather by the minimum signal-to-noise level (minimum resolvable slope) of the instrument. The pump fluence must be kept low to ensure linear excitation and decay dynamics. As a result of the low excitation fluence and relatively short exciton lifetime, the signal-to-noise level is lower than one might encounter in an inorganic system [117, 118]. However, diffusion constants estimated as low as ~ 0.2 cm^2/s can be robustly measured in PCDTBT with current instrumentation.

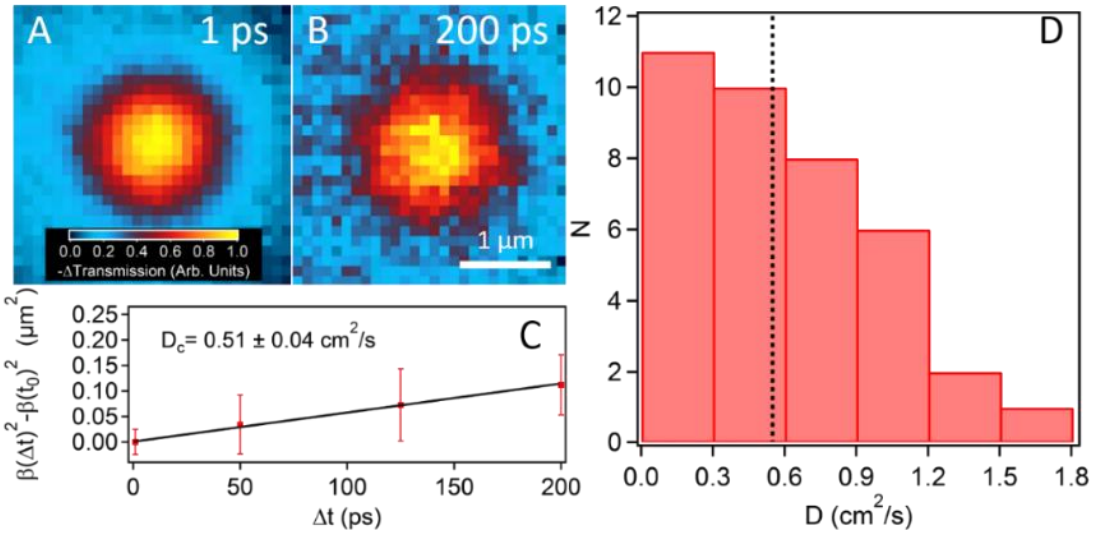

Figure. 5.2. Exciton transport data from diffraction limited volumes of PCDTBT thin films. (A and B) Spatially separated images of exciton density in PCDTBT collected at delay times of 1 ps and 200 ps, respectively. The color scale (A) and scale bar (B) apply to both panels A and B. (C) Plot of $\beta(\Delta t)^2 - \beta(t_0)^2$ vs. pump-probe delay time that shows exciton diffusion along the lateral axis to be 0.51± 0.04 cm^2/s. (C) Histogram of 38 exciton diffusivities in PCDTBT collected by PPM. The dashed line shows the average measured diffusivity of 0.55 cm^2/s.

Panel D in Fig. 5.2 shows exciton diffusivity along both the x- and y -axis measured at 19 individual locations. For 25% of the measurements, the exciton diffusion constant is below the resolution of the instrument. However, some locations exhibited markedly faster transport, with a maximum diffusion constant of 1.5 cm^2/s. On average, the local diffusivity of the films was 0.55 cm^2/s (dashed line). The average exciton diffusion constant observed in these sub-micron domains deviates significantly from generally accepted values for polymer films, which range between 10^{-6} and 10^{-2} cm^2/s depending on the specific electronic structure and morphology of the polymer as well as the technique used for characterization [33, 119]. For PCDTBT, an exciton diffusion constant of 1.1×10^{-4} cm^2/s was previously reported from photoluminescence quenching (PLQ) measurements [113].

The dramatic difference in diffusion coefficients measured by bulk and micro-scale characterization approaches indicates that local morphology may play a critical role in exciton transport. To test this hypothesis, thin films were prepared on substrates designed to macroscopically align the polymer backbones along a particular direction [100, 110, 111].

5.2.3 Macroscopic Alignment of PCDTBT Thin Films

Macroscopic alignment of polymer chains has been demonstrated to increase device scale charge carrier mobility in poly [4-(4,4- dihexadecyl-4H-cyclopenta [1,2-b:5,4-b'] dithiophen-2-yl)-alt-[1,2,5] thiadiazol [3,4-c] pyridine] (PCDTPT) by two orders of magnitude (16.3 cm^2/Vs) compared to randomly orientated PCDTPT polymer chains (0.7 cm^2/Vs) [110, 111]. Increased charge carrier mobility parallel to polymer chain alignment can be attributed to increased effective conjugation length of polymer chains that ranges from 5-10 repeat units, and a reduction in kinks known to act as trap sites [57, 120-122]. Intrachain transport rates reaching 10 cm^2/Vs are supported theoretically due to charge delocalization over extended sections of single polymer chains and faster hopping rates associated with intrachain transport [121, 123-126]. Morphological phenomena such as increased interchain connectivity, conjugation length persistence, and individual chain charge transport occur on length scales spectroscopically accessible only by high spatial resolution techniques such as PPM. However, inducing macroscopic alignment of polymer chains described here enhances these effects across increasingly long length scales.

A detailed description of MA PCDTBT thin film sample preparation can be found in the Methods section below. Briefly, by means of diamond nanoparticle lapping film, unidirectionally orientated nano-scale grooves are engraved on to a glass substrate. Panel

A in Fig. 5.3 shows an atomic force microscope (AFM) image of the structured substrate where the parallel axis denotes the orientation of the grooved substrate along which the polymers are expected to align themselves. Panel B shows a height profile of the AFM image taken from the black dashed line in panel A and shows that the grooves are on the appropriate length scale to allow preferential polymer alignment along the parallel axis.

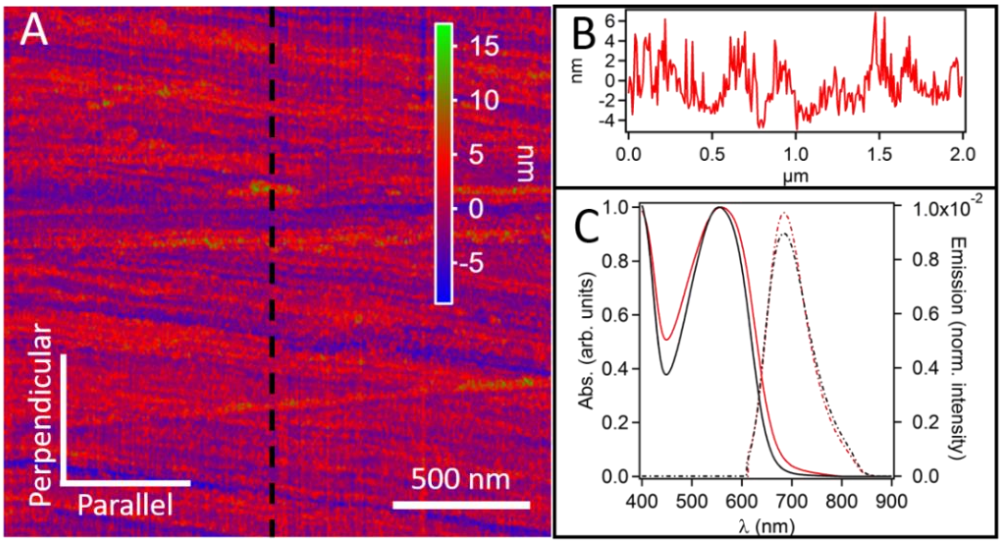

Figure. 5.3. Structured substrate preparation and steady state characterization of MA PCDTBT. (A) AFM height image of structured substrate made using 100 nm particle diamond lapping film. (B) Profile of the structured substrate height image taken from the location of the black dashed line in Panel A. (C) Steady state characterization of PCDTBT thin films. Absorption (solid: normalized to 1) and emission (dashed: normalized by area) spectra of amorphous and MA PCDTBT thin films (amorphous – black; MA – red).

Spectral evidence of polymer alignment is shown in Panel C of Fig. 5.3 by comparing absorption (solid) and emission (dashed) spectra of both amorphous (black) and MA (red) PCDTBT thin films (the amorphous thin film absorption and emission spectra are reproduced from Fig. 5.1-A). The MA PCDTBT shows a ~ 5 nm red shifted absorption profile. This red shift has been previously correlated to increased conjugation [57, 127] and/or an increased density of lower energy, higher order states within the polymer network

[59]. However, the emission spectrum remains relatively unchanged suggesting the lowest energy, higher order, states are present in both amorphous and MA PCDTBT thin films but that order may extend over longer distances in the latter [122, 128]. These lowest energy states correspond to sections of polymer chains with the longest effective conjugation, which can be 5-10 repeat units (10 – 20 nm for PCDTBT) in length [57].

Spatially separated imaging was then performed on the MA PCDTBT samples to determine how polymer orientation influences exciton diffusivity. Panel A of Fig. 5.4 shows an example of anisotropic exciton diffusion measured by PPM in macroscopically aligned PCDTBT thin films. The diffusivity perpendicular (black; $D_c = 1.1 \pm 0.1$ cm^2/s) and parallel (red; $D_c = 2.4 \pm 0.19$ cm^2/s) to the polymer alignment differs by 1.3 ± 0.2 cm^2/s indicating that exciton diffusivity may be increased due to favorable intrachain transport routes present in the MA PCDTBT thin films. Panel B of Fig. 5.4 compares the diffusion constants measured by PPM on both disordered (red circles) and MA (diamonds; parallel-filled blue, perpendicular-open green) PCDTBT thin films. The average diffusion values for the disordered polymer ($D_c = 0.55$ cm^2/s) as well as the perpendicular axis of the MA PCDTBT ($D_c = 0.67$ cm^2/s) closely agree and are shown by the corresponding horizontal lines in panel B of Fig. 5.4. However, macroscopic alignment of the polymer backbones increased the average exciton diffusivity along the polymer chain by a factor of ~6 ($D_c =$ 3.2 cm^2/s) compared to the disordered PCDTBT. This factor of ten enhancement is consistent with previous work that has shown a factor 5-10 (and greater) increase in mobility in devices that utilized substrate texturing to align polymer chains [110, 111].

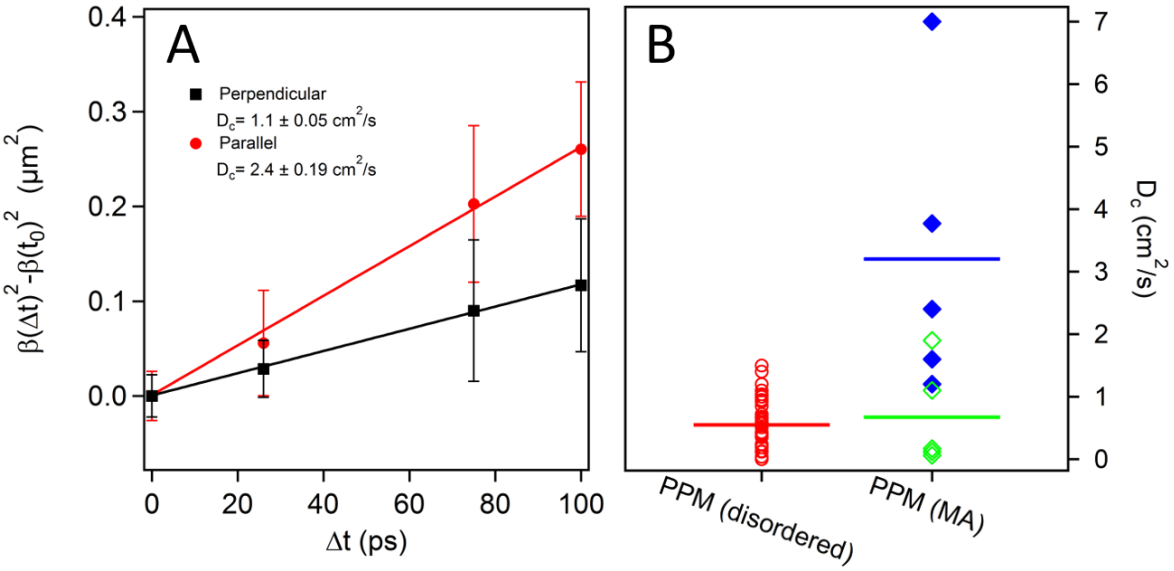

Figure. 5.4. Exciton diffusion in MA PCDTBT thin films. (A) Comparison of diffusion parallel (red) and perpendicular (black) with respect to the alignment of the polymer backbone. (B) Comparison of PCDTBT exciton diffusion collected by PPM (amorphous; red circles, MA; perpendicular: green diamonds, parallel: blue).

Accurate interpretation of exciton diffusion dynamics in complex polymeric networks is complicated by microscale spatial heterogeneity. While bulk characterization of PCDTBT (and other similar systems) provides a significant foothold for understanding the complexities of the microscale electronic environment, utilization of high spatial resolution spectroscopic techniques is necessary to determine accurate photophysical parameters. Broad distributions of photophysical parameters such as excited state diffusion or mobility and relaxation times are common for disordered OSP. For example, charge carrier (hole) mobility values reported in Poly (3-hexylthiophene) (P3HT) span 6 orders of magnitude and are dependent on material deposition, device fabrication, and characterization technique [119, 129, 130]. Similarly, the reported values of exciton diffusivity within this chap-

ter differ by 2-3 orders of magnitude compared to previously published results [113]. However, exciton diffusion values reported here correlate well with current theoretical and experimental literature that suggests the amorphous nature of PCDTBT thin films results in highly complex polymeric networks ranging from regions of well-ordered conjugation to regions of little to no long range ordering of the polymer backbones [125, 131]. Direct evidence of polymer chain alignment in amorphous PCDTBT thin films has been reported by time-resolved electron paramagnetic resonance studies which bolsters the hypothesis made here that microscale exciton diffusivity may be much faster than long range transport [114, 132]. Further, McGehee and co-workers have forwarded theoretical work that argued probing shorter length scales of disordered materials results in the observation of excited state transport rates increased by 2-5 orders of magnitude compared to bulk measurements [133]. Finally, the non-equilibrium state of the photogenerated exciton population (i.e. PPM experiments) may also enable transport rates to exceed that of equilibrated excited state populations such as electrically injected carriers (i.e. field effective transistor measurements) [106, 107]. Therefore, bulk spectroscopic techniques may inaccurately attribute the effects of material heterogeneity to the inherent exciton transport properties in PCDTBT, while utilizing PPM and other high spatial resolution spectroscopies, reduces the uncertainty of ensemble measurements [113, 134, 135].

Experimentally, recent work from the Huang and Ginsberg groups has found unexpectedly fast exciton diffusivity in disordered organic systems. Both groups have recently reported work toward the characterization of exciton transport properties from diffraction limited and sub-diffraction limited volumes, respectively, reporting faster exciton diffusion

than what has been observed by bulk spectroscopic method [16, 108]. Specifically, Huang's group has demonstrated that exciton diffusion in micron scale organic molecular aggregates reaches 3-6 cm^2/s, 3-5 times faster than theory suggests [108]. Ginsberg's research focuses on the development of methodology capable of deconvolving spatial heterogeneity with exciton diffusion [16]. Application of the methodology from Ginsberg's group may shed more light on the microscale exciton diffusivity observed here in PCDTBT thin films. Most recently, exciton diffusivity reaching 0.5 cm^2/s was reported as a result of microscale polymer chain alignment [112].

Considering the experimental results of this chapter and the supporting literature outlined above, the exciton diffusivity observed in PCDTBT thin films is proposed to be due largely to localized polymer self-alignment [114]. The long-range ordering presumably results in increased delocalization of the exciton, increased hopping distances, and increased hopping rates along and between polymer chain lengths. In order to evaluate this hypothesis a Monte Carlo simulation has been developed to correlate experimental results with photophysical parameters that are derived from FRET theory.

5.2.4 Morphology Dependent Förster Radius

The mechanism of exciton migration in molecular and polymeric organic systems has long been modeled by FRET [108, 122, 136-140], which parameterizes hopping transport in terms of the Förster radius, R_0. To correlate the morphology dependent exciton diffusivity reported in this manuscript with established FRET theory, the effective Förster Radius (R_0) is calculated from the steady state spectra shown in panel C of Fig. 5.3 by:

$$R_0 = 9.78 \times 10^2 \left(\frac{\kappa^2 Q_D J(\lambda)}{n^4} \right)^{1/6} \tag{5.2}$$

where κ is the orientation factor of the donor and acceptor dipoles ($\kappa^2 = 2/3$), Q_D is the quantum efficiency of the donor material ($Q_D = 0.309$), and n is the refractive index of the donor material ($n = 2$) [140]. The overlap integral,

$$J(\lambda) = \int_0^\infty F_D(\lambda) \varepsilon_A(\lambda) \lambda^4 \partial\lambda \tag{5.3}$$

is determined by the spectral overlap of the area-normalized emission spectrum ($F_D(\lambda)$) and absorption cross section ($\varepsilon_A(\lambda)$), where λ is in units of nanometers [33]. The maximum amplitude of the PCDTBT absorption cross section is 4 x 10^4 $M^{-1}cm^{-1}$ as previously reported in literature [141]. Resulting R_0 values of 2.7 nm and 3.1 nm for the amorphous and MA PCDTBT bulk thin films, respectively, are similar to R_0 values previously calculated in PCDTBT:Fullerene blends [113, 142]. The 0.4 nm increase in the MA PCDTBT R_0 value is due to increased overlap of the absorption and emission spectra as shown in panel C of Fig. 5.3.

In Förster theory, D_c is dependent on R_0 by:

$$D_c \sim \frac{{R_0}^6 N^{\frac{4}{3}}}{\tau_r} \tag{5.4}$$

where N (nm^{-3}) is the chromophore density and τ_r is the radiative lifetime of the exciton [137, 143]. The observed exciton lifetime measured by PPM represents the sum of the radiative and non-radiative exciton relaxation rates. Therefore, it is possible to calculate τ_r with the fluorescence quantum efficiency, Q_D by:

$$\tau_r = \frac{\tau_{obs}}{Q_D} \tag{5.5}$$

where τ_{obs} is the average exciton lifetime of a biexponential fitting function applied to excited state decay data from amorphous (τ_{obs} = 98 ps) and MA (τ_{obs} = 52 ps) PCDTBT thin films [144]. Assuming the quantum yield does not change between amorphous and MA thin films, τ_r is equal to 317 ps and 168 ps, respectively. The significant difference in lifetime is most likely due to enhanced interchain relaxation mechanisms in the case of the MA PCDTBT thin films that manifest as shorter lifetime components [59].

Figure 5.5 shows a plot of D_c as a function of τ_r described by Eq. 5.4, for both the amorphous (solid black) and MA (solid red) PCDTBT thin films R_0 values while N is held constant at 1 chromophore/nm^3 [145]. Also shown in Fig. 5.5 are the average exciton diffusion values found experimentally (MA Parallel Diffusion: red dashed, Amorphous: black dashed) and previously published (green dashed) [113]. The relationship plotted in Fig. 5.5 shows that if exciton diffusion constants in amorphous PCDTBT thin films were as low as previously reported (PLQ: 10^{-4} cm^2/s) [113], τ_r would need to be greater than 40 ns, while reported singlet exciton lifetimes in PCDTBT and other OSPs are typically below 5 ns [133, 144]. In the same way, the diffusion constants reported in this manuscript do not

accurately correspond to the radiative lifetime calculated from PPM data, and R_0 values calculated from steady state spectra. The discrepancy between reasonable singlet exciton radiative lifetimes in PCDTBT and observed exciton diffusivity may have two causes. First, PLQ does not characterize diffusivity in the absence of a quenching molecule, exclude effects caused by polymer/quencher aggregation, account for inconsistencies across multiple film preparations, or probe non-fluorescing excitons [16, 33, 146, 147]. Second, the simple FRET model traditionally applied to these systems, may fail when exciton delocalization along polymer chains extends significantly farther than nearest neighbor distances as is hypothesized in this chapter [139].

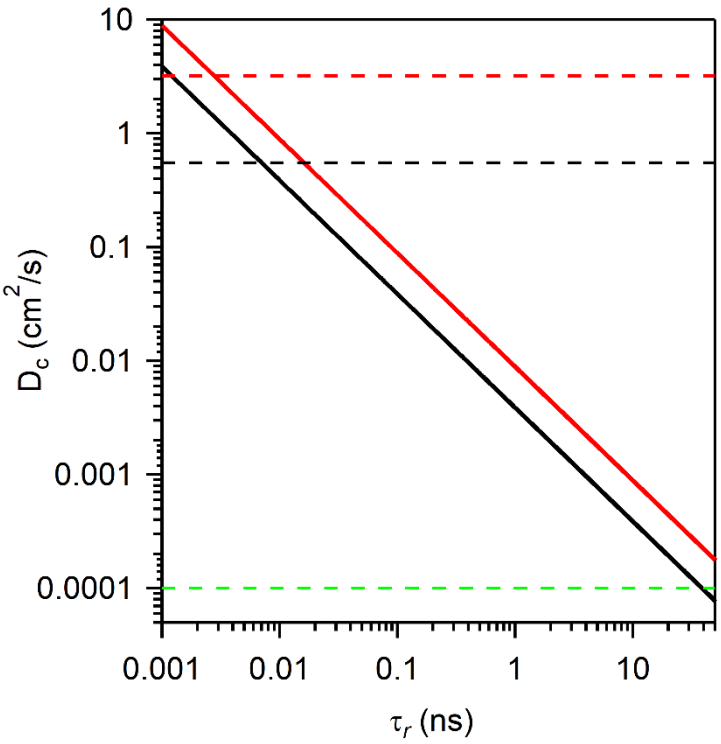

Figure. 5.5. Plot of exciton diffusion constant vs. exciton radiative lifetime described by Eq. 5.4. The solid black and red traces correspond to R_0 values corresponding to amorphous and MA PCDTBT, respectively (N = 1 nm^{-3}).

5.2.5 Monte Carlo Simulation

In an effort to explain the discrepancy between exciton diffusivity reported here and what is suggested by Förster theory, a course-grain MC simulation is developed to determine the influence of polymer alignment, hopping distance, and energy transfer rate. Two separate simulation scenarios are presented here, amorphous and MA PCDTBT, shown in panels A and B of Fig. 5.6, respectively. Within each polymer network, individual polymer chains are treated as rigid rods with a standard length of 94 nm determined by the average length of the experimental PCDTBT samples [145]. The use of rigid rod polymers reduces the parametric ambiguity arising from morphological trap concentration and chain flexibility and have also been used previously to model simple diffusive transport in polymer networks [121]. Within the limit of power independent relaxation dynamics, excitons do not interact with each other and therefore single exciton MC simulations can be executed sequentially until the simulation converges to a singular value for exciton diffusivity. The spatial polymer distribution is defined to be large enough that excitons do not interact with the simulation boundaries.

The MC simulation evaluates exciton migration through a series of intra- and interchain hopping events weighted by both the spatial location of the exciton and the relative transport mechanism rates. First, intrachain transport rates are held greater than or equal to interchain transport rates as proposed by previous theoretical work [125]. Second, interchain transport is given a nonzero probability if and only if a neighboring polymer is within the hopping range of the exciton. Interchain hopping is also restricted to transfer between the exciton location and the nearest neighboring polymer chain location. Third, excitons

are restricted to intrachain transport within the length of the polymer and the probability of interchain transport is not varied as a function of exciton location along the polymer chain. At the end of the simulation, the final location of the exciton is compared to the starting location. The separation distance which is equivalent to diffusion length (L_D) is used to calculate D_c as described elsewhere [33].

Panel C of Fig. 5.6 graphically depicts the hopping event options dependent on the position of the exciton. Panel C-1 and C-2 represent two separate situations where the exciton is either limited to intrachain hopping events (C-1) or spatially aligned with a nearby polymer allowing for interchain transport (C-2). Panel C-3 demonstrates the spatial restriction an exciton encounters at the end of a polymer chain.

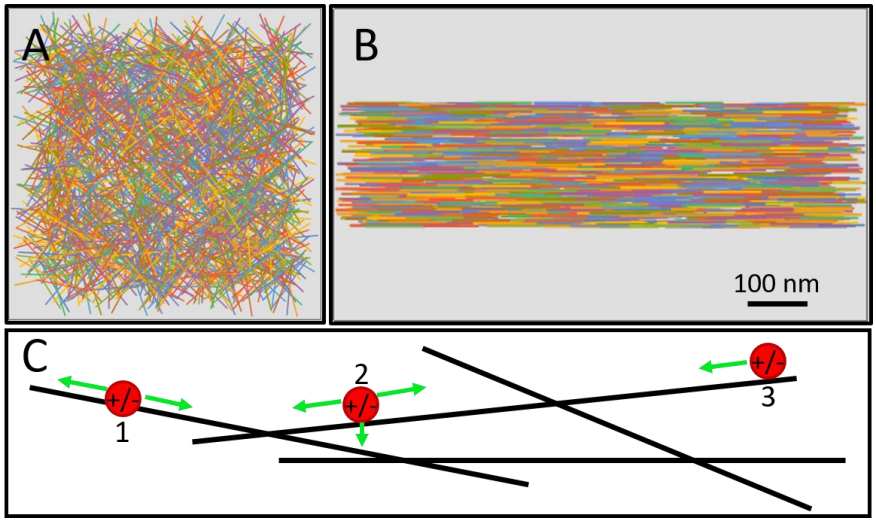

Figure. 5.6. Depiction of polymer morphology used in MC simulations. (A and B) Simulation of randomly orientated and MA polymer networks, respectively. The scale bar in panel B applies to both A and B. (C) Spatially dependent hopping transport mechanisms depicted within a sub portion of a simulated disordered polymer network. The green arrows of C1-3 denote optional hopping events determined by the spatial location of the exciton (red circles).

The MC simulation is dependent on only two variables other than morphology, hopping distance (σ) and rate (k_{hop}). These two parameters can be related to the exciton diffusivity in the MC simulation by:

$$D_c = \frac{\sigma^2 k_{hop}}{3} \tag{5.6}$$

where the right side is weighted by a coefficient of 1/3 when the three hopping possibilities (left or right intrachain, interchain) are of equal probability [33, 148]. Equation 5.6 holds for a morphologically unrestricted system (perfectly crystalline). However, in the limit that there are constraints (polymer networks), the transport will not reach this value.

The hopping distance σ can be related to R_0 (as calculated above: MA: 3.1 nm, Amorphous: 2.7 nm). Similarly, the hopping rate (k_{hop}) can be calculated using Förster theory by:

$$k_{hop} = \frac{1}{\tau_r}\left(\frac{R_0}{d}\right)^6 \tag{5.7}$$

where d (1 nm) is the distance between chromophores [149]. When applying the previously calculated values of R_0 and τ_r in this manuscript, the hopping rate is found to be 2.8 ps^{-1} and 3.1 ps^{-1} for amorphous and MA PCDTBT thin films, respectively. The increased transfer rate of the MA PCDTBT samples is a direct result of the increased spectral overlap between the steady state absorption and emission bands (Fig. 5.3). While R_0 is a valid starting parameter for σ, insertion into equation 5.6 along with the calculated values of

k_{hop} fails to estimate experimental values of exciton diffusivity. To account for the discrepancy, exciton diffusivities similar to the average values shown in Fig. 5.4 and the calculated values of k_{hop}, are used to calculate alternative values for σ using Eq. 5.6. Under these conditions, σ is found to be equal to 8 nm and 22 nm for amorphous (D_c = 0.55 cm^2/s, k_{hop}=2.7 ps^{-1}) and MA (D_c = 5.0 cm^2/s, k_{hop}=3.1 ps^{-1}) PCDTBT thin films, respectively. Although 8-22 nm hopping distances are significantly higher than the calculated values of R_0, they closely reflect polymer chain persistence lengths reported in the literature [57, 120].

Figure 5.7 summarizes the MC simulation results collected while varying the exciton hopping distance and the ratio of intrachain: interchain transport mechanism rates. The dashed lines in Fig. 5.7 denote the average experimental exciton diffusivities in amorphous (black: 0.55 cm^2/s) and MA (parallel; red: 3.2 cm^2/s) PCDTBT thin films as well as previously published exciton diffusion values (green: 10^{-4} cm^2/s) [113]. Simulation results shown with open markers assume k_{hop} is equal to 2.8 ps^{-1} and 3.1 ps^{-1} for amorphous (black) and MA (red), respectively. Like-colored traces are further distinguished by circle, square, or triangular markers that correspond to intrachain: interchain transport rate rations of 100:1, 10:1, and 1:1, respectively.

For both amorphous and MA polymer simulations, increasing σ results in exciton diffusivity approaching an asymptotic limit on the log scale when σ > 8 nm for the amorphous morphology and when σ > 15 for the MA morphology. While increasing the interchain transport rate delays the onset of the asymptotic limit, the simulation still does not

converge to the experimental values of exciton diffusivity for either polymer morphology. Notably, previously published exciton diffusivity (10^{-4} cm^2/s) is well reproduced when σ = 0.1 nm. The repeat unit of PCDTBT is roughly 2 nm meaning that if σ = 0.1 nm, excitons would not transfer to an adjacent repeat unit in a single hop [145].

The values of R_0 and k_{hop} initially used in the MC simulation are derived from bulk measurements. However, the site-to-site values may vary drastically due to morphological heterogeneity, and nonequilibrium transport [59, 114]. Due to the observation that increasing the hopping distance (8-22 nm) beyond what is predicted by Förster theory results in better agreement between experiment and theory, the logical next step is to evaluate the remaining variable from Eq. 5.6, k_{hop}. The traces indicated by the solid triangular markers in Fig. 5.7 demonstrate the effects of increasing k_{hop} by a factor of two relative to Förster theory (amorphous: 5.4 ps^{-1}, MA: 6.2 ps^{-1}) while the intrachain: interchain transport rate ratio is held at 1:1. Under the conditions of increased hopping distance and rate compared to what is predicted by FRET, results of the MC simulation begin to converge with experimental values.

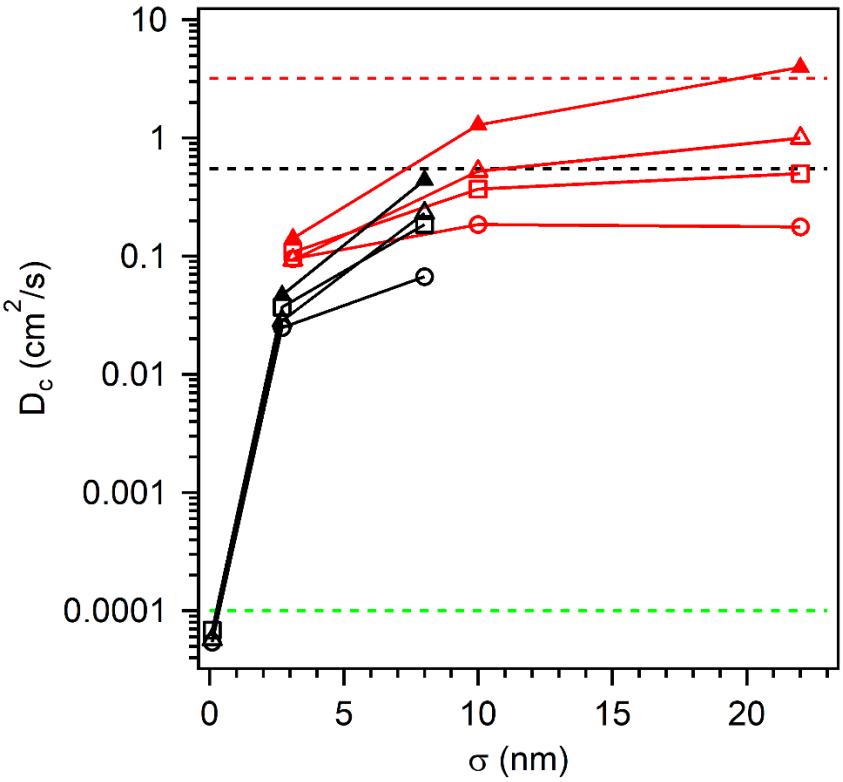

Figure. 5.7. MC simulation results. Dashed lines designate the exciton diffusivities published previously (green), and reported in this manuscript (Amorphous: black, MA: red). The solid black and red traces correspond to simulation results from amorphous and MA polymer morphology. The solid traces are further distinguished by the marker shape, and fill. Open markers represent simulations executed assuming the exciton hopping rate defined by Förster theory, while the filled markers represent a hopping rate two times greater. The shape of the marker represents the order of magnitude that the interchain transport is decreased relative to the intrachain transport rate (circle: 2, square: 1, triangle: 0).

While the simulations described above provides insight into the parameters that are relevant to transport in the polymer films, there are well known limitations with FRET theory, particularly in condensed phase samples. For example, it is well known that FRET theory fails as the point-dipole approximation breaks down, as is the case when the chromophore density and size increases [139]. Conjugated segments of PCDTBT polymer chains (treated as single chromophores) may extend 10-20 nm, possibly enabling exciton

delocalization across significant lengths scales [57, 120]. As a result, exciton transport would become a convolution of exciton delocalization and point to point hopping which may not be comprehensively explained by a simple Förster radius.

Increasing the sophistication of the MC simulation, to account for non-uniform effective conjugation (chromophore) length within individual polymer chains, energy dependent transport rates, and interchromophore dipole-dipole orientation may result in a more accurate understanding of exciton diffusivity in OSPs. However, the simple coarse grain MC model developed here provides insight into material transport parameters necessary to reproduce the experimental data. Specifically, using the MC simulation has determined that increased conjugation length, hopping distance/exciton delocalization, and transport rate are all likely to contribute to the spatially varying exciton diffusivity observed in amorphous and MA PCDTBT thin films.

To confirm the effects of spatially varying polymer chain morphology on exciton diffusivity in PCDTBT thin films, future experiments will seek to correlate spatially resolved emission spectra with localized exciton diffusivity. As suggested in bulk steady state emission spectra, a red shift in spatially resolved emission should accurately map on to increased local exciton diffusivity. A second possible experimental direction is to vary the excitation energy (pump wavelength). Probing the exciton dynamics under the conditions of increased, or decreased photoexcitation energy may prove to elucidate effects of non-equilibrium excited state dynamics on localized exciton diffusivity.

5.3 Conclusion

In this chapter direct observation of exciton diffusion in disordered PCDTBT thin films by PPM is reported, averaging 0.55 cm^2/s in amorphous thin films and increasing by 10-fold along polymer chains that are macroscopically aligned. MC simulations are also utilized to evaluate the effects polymer self-organization have on localized exciton diffusion with respect to hopping distance, exciton delocalization, and hopping rates. Exciton diffusivity in disordered OSPs has been thought to be 2-4 orders of magnitude lower than most classical crystalline semiconductors. However, the highly-localized polymer orientation dependent exciton diffusivity reported in this chapter presents a promising handle to increase the utilization of low cost polymer based organic optoelectronic components in place of the current inorganic semiconductor technologies. The effects of polymer orientation reported in this chapter also suggest that OPV PCEs may increase beyond the current values by leveraging polymer alignment across macroscopic length scales.

5.4 Methods

5.4.1 PCDTBT Thin Film Preparation

A 3.6 mg/ml solution of PCDTBT (M_w = 20 - 45 KDa; Solaris Inc.) in chlorobenzene or dichlorobenzene was stirred at room temperature for 22 hours before being drop cast onto a glass microscope slide under a N_2 atmosphere. The sample was then allowed to dry completely before being covered with a microscope coverslip and sealed using an epoxy.

5.4.2 Structured Substrate Preparation and MA PCDTBT Deposition

Macroscopic alignment of polymer chains was achieved by microscopically structuring the sample substrate. To structure the glass substrate, diamond lapping film (particle size 100 nm) was used as part of a homebuilt substrate scratching apparatus shown in Fig. 5.8. The microscope slide is mounted on the underside of part A while the diamond lapping film is adhered to the top of part B. Part B is mounted on a dovetail rail system allowing it to be manually translated across the stationary microscope slide and produce nanoscale grooves as shown in Fig. 5.3. A drop of deionized water was deposited between the glass substrate and the diamond lapping film, and the films were passed over the substrate roughly 2.5 meters. The substrate was then cleaned using acetone to remove any debris. In order to encourage the preferential orientation of the polymer backbones along the structured axis, directional evaporation of the drop cast polymers is performed while the substrate is also angled (13°) during the drop casting procedure [111].

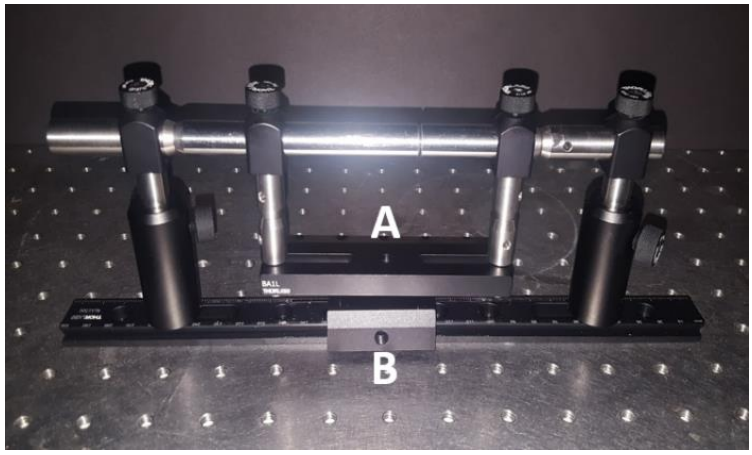

Figure 5.8. Image of home-built substrate scratcher. The microscope slide is mounted on the underside of part A and the diamond lapping film is adhered to the top of part B. Part B is able to unidirectionally translate to engrave nanoscale grooves on the surface of the microscope slide.

5.5 Acknowledgements

This work was funded by the Division of Chemical Sciences, Geosciences, and Biosciences, Office of Basic Energy Sciences of the U.S. Department of Energy through Grant DE-SC0014128.

CHAPTER SIX

TOWARD DIRECT IMAGING OF SUB-10 NM CARRIER DIFFUSION LENGTHS BY DIFFERENTIAL DETECTION PUMP-PROBE MICROSCOPY

Contribution of Authors and Co-Authors

Manuscript in Chapter 6

Author: Eric S. Massaro

Contributions: Performed all experimental data collection of differential detection data. Prepared the manuscript for submission.

Co-Author: Erik M. Grumstrup

Contributions: Developed the theoretical groundwork for differential detection pump-probe microscopy and co-wrote the manuscript.

Manuscript Information Page

Eric S. Massaro and Erik M. Grumstrup

Status of Manuscript:
__X__ Prepared for submission to a peer-reviewed journal
____ Officially submitted to a peer-review journal
____ Accepted by a peer-reviewed journal
____ Published in a peer-reviewed journal

TOWARD DIRECT IMAGING OF SUB-10 NM CARRIER DIFFUSION LENGTHS BY DIFFERENTIAL DETECTION PUMP-PROBE MICROSCOPY

Eric S. Massaro[1] and Erik M. Grumstrup[1, 2]

1. Department of Chemistry and Biochemistry, Montana State University, Bozeman, Montana 59717, United States
2. Montana Materials Science Program, Montana State University, Bozeman, Montana 59717, United States

6.1 Introduction

Utilizing pump-probe microscopy (PPM) enables the characterization of microscale excited state diffusivity with diffraction limited spatial resolution, the results of which contribute substantially to an understanding of transport at sub-micron length scales. However, phenomena such as early time nonequilibrium diffusion and diffusion across regions of spatially varying materials such as OSPs can obscure the accurate characterization by traditional methodology. Additionally, solution processed disordered semiconducting materials often have diffusion constants ≤ 1 cm^2/s, far lower than their inorganic single crystalline counterparts [1, 2, 23, 24, 117, 118]. While disordered semiconducting materials have a significant advantage over traditional single crystal materials with respect to their low cost of fabrication and reduced environmental impact, in extreme cases, accurate characterization of low diffusivity excited states, or spatially and temporally varying diffusion, will inevitably require measurements of carrier diffusion on sub-10 nm length scales. Therefore, developing spectroscopic tools that can accurately

characterize excited state transport on sub-10 nm length scales is important to maximize the potential of disordered semiconductors in optoelectronic and photocatalytic applications [4, 29, 150, 151].

Previous chapters demonstrated that, by using PPM, the rate of excited state diffusion can be determined with diffraction limited spatial resolution [6-8]. However, when attempting to detect excited state diffusion on sub picosecond time scales or sub-10 nm length scales, deconvolving instrument noise and excited state diffusion becomes increasingly difficult. The remainder of this chapter will outline the experimental design of differential detection pump probe microscopy (DDPPM). DDPPM is a novel spectroscopic approach designed to characterize excited state diffusion in complex materials systems on length scales inaccessible by current methodology. Here, the experimental viability of DDPPM is tested on a single crystal Silicon wafer, while the sensitivity of DDPPM to diffusive motion is theoretically evaluated. Finally, the limitations of DDPPM and future directions for technique development are discussed.

6.2 Results and Discussion

6.2.1 Excited State Diffusion

The diffusion of photoexcited species in semiconducting materials can be described by:

$$\frac{dN}{dt} = D_c \nabla^2 N - \frac{N}{\tau} \tag{6.1}$$

where N is the concentration of excited states, D_c is the material diffusion constant, ∇ is the Laplace operator, and τ is the excited state lifetime [33]. Diffusive motion results in the transport of carriers from regions of high concentration to regions of lower concentration. Utilizing PPM, the diffusive motion of excited state species is measured by directly imaging the time dependent spatial evolution of the excited state population [7, 117, 118]. This process has been described in detail within chapters 1 and 5. The diffusion length $\left(L_D\right)$ of excited states during an interval, τ, can be expressed in terms of the diffusion constant via,

$$L_D = \sqrt{2ZD_c\tau} \tag{6.2}$$

where Z is a dimensionality coefficient equal to 1, 2, or 3 corresponding to 1, 2 or 3-dimensional diffusion [33]. The relationship between diffusivity and diffusion length is shown in Fig. 6.1 for $Z = 2$. The four traces represent the carrier diffusion length as a function of time following photoexcitation while the diffusivity is varied over 4 orders of magnitude (red: 10 cm^2/s, orange: 1.0 cm^2/s, green: 0.1 cm^2/s, blue: 0.01 cm^2/s). Figure 6.1 shows that under the conditions of low diffusivity and/or short time delays, determining the excited state diffusion length by optical methods such as PPM is challenging due to the diffraction limit of light (~200 nm) [37].

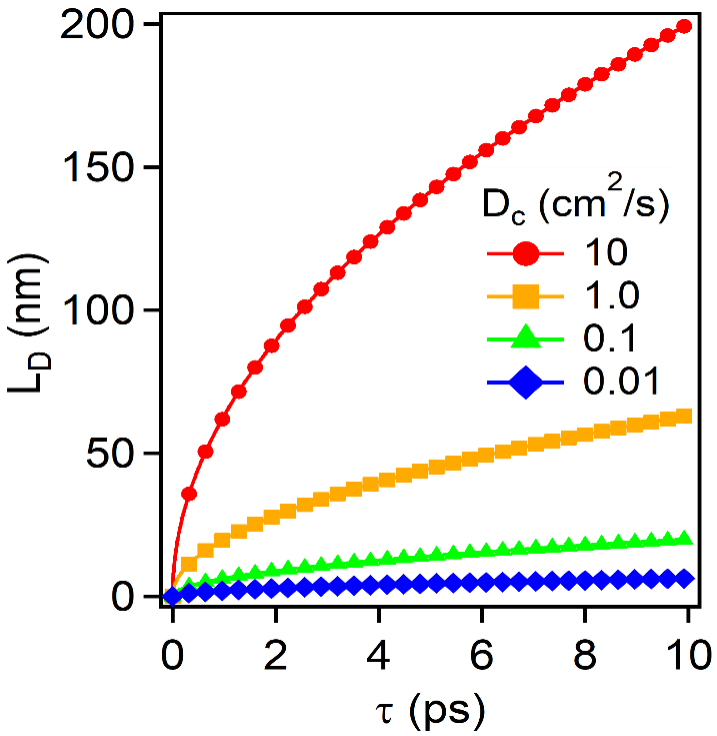

Figure. 6.1. Excited state carrier diffusion length as a function of time (τ) and diffusivity as described by Eq. 6.2. The four colored traces range 4 orders of magnitude in carrier diffusivity as described by the legend.

Here, the development of DDPPM demonstrates progress toward the detection of excited state diffusion with sensitivity to diffusive motion far below the diffraction limit and improved signal-to-noise ratios (SNRs) compared to traditional PPM. Using multiple probe pulses to cancel the spectroscopic contributions of excited states that have not exited the excitation volume is a novel experimental design and presents potential methodology to use for accurate characterization of excited state diffusivity.

6.2.2 Experimental Development of DDPPM

Figure 6.2 depicts the experimental requirements of DDPPM. Panel A shows the experimental schematic where each of the two probe arms are modulated by an AOM. The

two AOMs are electronically coupled to simultaneously reduce the 80 MHz repetition rate of the Ti:Sapphire oscillator to 8 MHz and chop the pulse train at 98 KHz. The two probe pulses are further differentiated from one another by an inverter logic chip that creates a 180° phase offset between the two probe pulse trains. The timing of the probe pulses is shown in panel C of Fig. 6.2 by the green and orange pulses. One probe arm (green) is directed onto a delay stage to allow temporal separation ($\Delta\tau_{p-p}$) between the two probe pulses. A 50:50 beamsplitter is then used to recombine the two probe arms (green and orange) before being directed toward a set of galvanometer mirrors for spatial variation of the probe pulse on the sample surface. The pump arm shown in panel A (blue) is directed to an AOM that reduces the repetition rate of the laser to 8 MHz and simultaneously operates on a 50% duty cycle (1.4 MHz). A second translation stage in the path of the pump arm controls the temporal separation between the pump and both probe pulses (Δt) as shown in the top portion of panel B. The pump and probe arms are recombined, colinearly directed to a microscope objective (100X, 0.9 NA), and focused to diffraction limited spot sizes on the sample surface.

Spatially separated imaging (as described in chapters 1 and 5) is performed using one probe, or both, to obtain time dependent distribution or differential distribution images of the photoexcited population. In DDPPM, the two temporally separated pump-probe interactions serve to reduce uncertainty of the observed diffusive motion by canceling the signal from any excited states that have not diffused away from the initial point of excitation over the time period of $\Delta\tau_{p-p}$. The signal cancellation is depicted in the bottom portion of panel B where $I(\Delta t+\Delta\tau_{p-p})$ is the charge distribution of carriers prior to

diffusive motion and is 180° out of phase with the charge distribution, $I(\Delta t)$, that has diffused over the time period of $\Delta\tau_{p-p}$. The red trace in panel B of Fig. 6.2 depicts the detected differential distribution signal (ΔI) whose amplitude and width are proportional to carriers that have diffused beyond the initial excitation volume over the time period of $\Delta\tau_{p-p}$.

Detection of this differential signal is accomplished by first, an optical homodyne of the probe pulses using an amplified photodiode. However, since there are two probe pulse trains it is necessary to distinguish the individual contributions. By electronically mixing the detected signal frequency from the photodetector with the frequency of the pump modulation as the local oscillator (1.4 MHz), the transient signal is shifted to the low frequency modulation of the probe pulse train (98 KHz) [152]. The 180° phase offset of the two probe pulse trains results in the lock in amplification of the two pump-probe signals with opposing signs (positive or negative). The opposing values allow for selective spectroscopic cancelation of the excited states within the initial excitation volume [152].

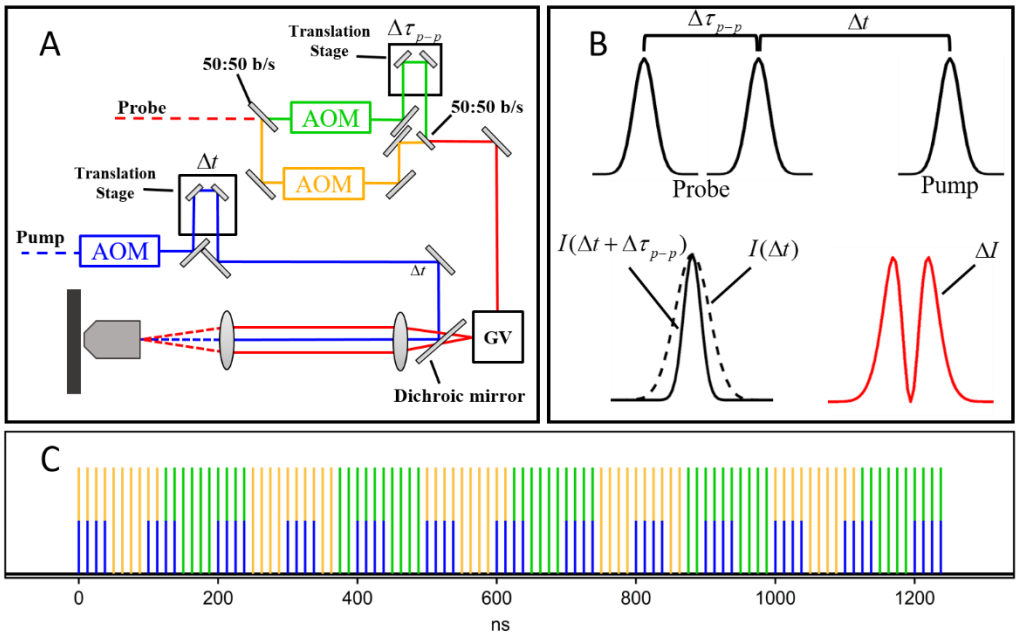

Figure 6.2. Experimental design of DDPPM. (A) Instrument Schematic. The pump and probe arms are generated from a Ti:Sapphire oscillator. The pump arm is modulated to 8 MHz and chopped at 1.4 MHz by an AOM before being directed onto a translation stage to control the pump-probe delay time. The probe arm is divided to produce the necessary two probe pulses. Both probes are modulated to 8 MHz and chopped at 98 KHz using a Boolean logic circuit. The two probe beams are recombined and directed onto a set of Galvanometer mirrors in order to spatially separate the pump and probes. (B) Depiction of pulse timing and differential detection of diffused carriers. (C) Pulse modulation scheme. The green and orange pulses represent the two probe beams at an 8 MHz repetition rate modulated out of phase from on another at 98 KHz. The blue pulses represent the pump beam which was modulated at 8MHz and chopped at 1.4 MHz.

6.2.3 DDPPM Data Analysis

To test the versatility of DDPPM, the diffusion of free carriers in a single crystal Silicon wafer is measured where $D_c \leq 18\,\mathrm{cm}^2/\mathrm{s}$ [153]. First, using PPM to measure the excited state diffusion by the conventional method of spatially separated imaging as described in chapters 1 and 5 and then by DDPPM [117, 118]. The data in Fig. 6.3 was collected using 550 nm (super continuum generation using photonic crystal fiber) excitation and 800

nm (fundamental wavelength) probe wavelengths. The results of the standard PPM measurements are shown in panels A and B of Fig. 6.3. Panel A shows carrier density distributions at varying pump-probe delay times, while panel B shows the average diffusivity (solid black: 10.7 cm^2/s) of 10 measurements (5 locations in both the x and y dimensions). The dashed lines show the values one standard deviation away from the average value. Even though the data presented in panel B was collected on a single crystal Si wafer, the diffusivity values vary significantly. This variability demonstrates the uncertainty of traditional PPM methodology despite the material uniformity.

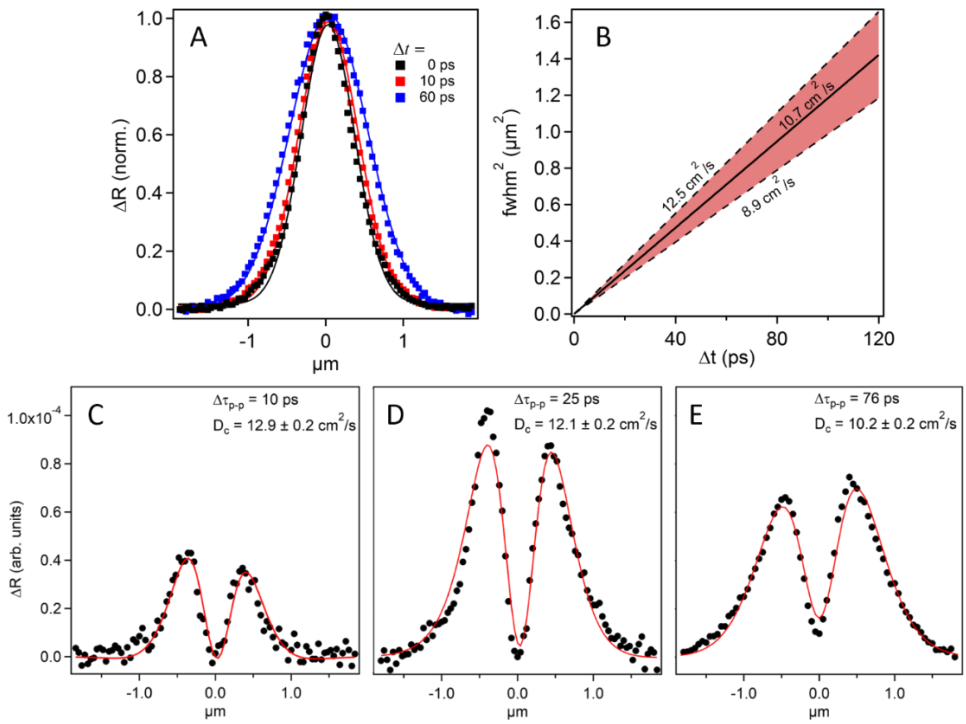

Figure 6.3. Comparison of PPM and DDPPM data. (A) Example of charge carrier distribution profiles collected at pump-probe delay times of 0, 10 and 60 ps. (B) The average diffusivity measured in a single crystal silicon wafer at 5 locations in both the x and y dimensions (N=10). The dashed lines indicate ± 1 standard deviation. (C, D, E) Differential detection profiles (black circles) collected with increasing delay times between the two probe pulses. The red traces indicate the differential fitting function used to extract the material diffusion constant as described below.

PPM data is processed by first fitting multiple time dependent excited state distributions with Gaussian functions (Fig. 6.3, panel A) and then using a linear fit to determine the rate of diffusion (Fig. 6.3, panel B) [87, 117, 118]. DDPPM does not require the collection of multiple time dependent spatially separated images. Instead, one differential profile is needed which is encoded with temporal information because of the time delay between the two probe pulses. The only other data required is the spatial distribution profiles of both pump-probe signals when Δt and $\Delta t + \Delta\tau_{p-p}$ are equal to 0 ps. These two distributions are used as starting parameters for the fitting process. Here, each starting parameter distribution profile is fit by the product of Gaussian and Lorentzian functions ($[L \cdot G]$) . The full differential signal can then be fit by:

$$Differential_{Model} = \left([L \cdot G]_1 \otimes \Delta[D, x, t] \right) - [L \cdot G]_2 \tag{6.3}$$

where $[L \cdot G]_1$ and $[L \cdot G]_2$ are the initial carrier distributions when Δt = 0 and $\Delta t + \Delta\tau_{p-p}$ = 0, respectively. The solution to the diffusion equation ($\Delta[D, x, t]$) is modeled by:

$$\Delta[D_c, x, t] = \frac{A}{\sqrt{4\pi D_c t}} \cdot Exp\left[\frac{-x^2}{4\pi D_c t} \right]. \tag{6.4}$$

Here A is a normalization factor that accounts for decay in the signal amplitude of $[L \cdot G]_1$ over the time duration of $\Delta\tau_{p-p}$. The convolution in Eq. 6.3 of $[L \cdot G]_1$ and $\Delta[D_c, x, t]$ produces the distribution profile equivalent to $I(\Delta t)$ in panel B of Fig. 6.2, while the excited state distibution fit by $[L \cdot G]_2$ is equivalent to $I(\Delta t + \Delta\tau_{p-p})$. The elegance of this fitting technique is that the initial distributions can be fit with an arbitrary fitting function

to precisely match the optical systems point spread function. In the case of spatially separated imaging that results in perfectly Gaussian charge distributions, Eq. 6.3 simplifies to the difference between two gaussian distributions while accounting for the diffusive expansion of the first term.

Using the fitting method outlined above, three example profiles collected with DDPPM are shown in panels C, D, and E of Fig. 6.3 while $\Delta\tau_{p-p}$ is equal to 10 ps, 25 ps, and 76 ps, respectively. Across these three examples, the extracted diffusivity averages 11.7cm^2/s while the error of each measurement is only ~2%. In comparison, the error in the standard PPM measurements is ~17%. This direct comparison of the two methods demonstrates the potential of DDPPM to provide significantly more accurate characterization of excited state diffusivity.

Close examination of the differential data in panels C, D, and E of Fig. 6.3 reveals the nonlinear relationship of the maximum signal amplitude of the differential signal with respect to $\Delta\tau_{p-p}$. This nonlinearity is a result of competing factors affecting the amplitude and/or width of the differential signal. At short time delays ($\Delta\tau_{p-p} \leq 10$ ps) the differential signal is primarily due to the small fraction of photoexcited carriers that have diffused away from the localized excitation while having relatively little time to relax to the ground state (panel C). At later times ($20 \leq \Delta\tau_{p-p} \leq 50$ ps, panel D), the differential signal amplitude increases as more excited states diffuse away from the localized excitation. The differential signal amplitude continues to increase as long as diffusive motion outweighs the effects of excited state relaxation. Panel E in Fig. 6.3 shows that at long delay times ($\Delta\tau_{p-p} \geq 50$ ps)

the differential signal amplitude decreases. Both the spatial expansion of the profile due to diffusion, and relaxation of excited states results in the decreasing amplitude of the differential signal.

6.3 Theoretical Investigation of DDPPM Sensitivity

Results shown in Fig. 6.3 confirm the effectiveness of DDPPM as a novel method for quantifying excited state diffusivity. However, a more important goal of DDPPM is to provide a spectroscopic technique with increased sensitivity to sub-10 nm diffusion lengths in complex disordered semiconducting materials. The minimum diffusion length that can be measured with DDPPM is limited by the signal-to-noise ratio (SNR) of the instrument. For the data presented in Fig. 6.3 (which reflects noise levels that are typical of experimental data), that level is estimated to be on the order of 5:1. A SNR of 5:1 will herein be assumed as the minimal acceptable limit in order to collect resolvable DDPPM data. This section describes simulations performed to quantify the minimum resolvable diffusion length given practical detection limits of DDPPM.

The simulations are carried out using Eq. 6.3, where an initial excited state distribution profile ($[L \cdot G]_1$) is generated with a single exponential decay lifetime of 100 ps. The diffusion of the profile is described by the convolution of $[L \cdot G]_1$ and Eq. 6.4. The amplitude of a second excited state distribution, equivalent to $[L \cdot G]_2$, is set to precisely cancel the transient signal of $[L \cdot G]_1$ with respect to $\Delta\tau_{p-p}$. Figure 6.4 summarizes simulation results by plotting the SNR of the simulated differential signal profiles as a

function of L_D, which is correlated to the $\Delta\tau_{p-p}$ with respect to the modeled diffusivity. The panels are distinguished by the modeled excited state diffusivity (A: 10 cm^2/s, B: 1.0 cm^2/s, and C: 0.1 cm^2/s), and the traces within each panel correspond to the initial SNR of the simulated $[L \cdot G]_1$ (circles: 1000:1, squares: 100:1, and triangles: 10:1).

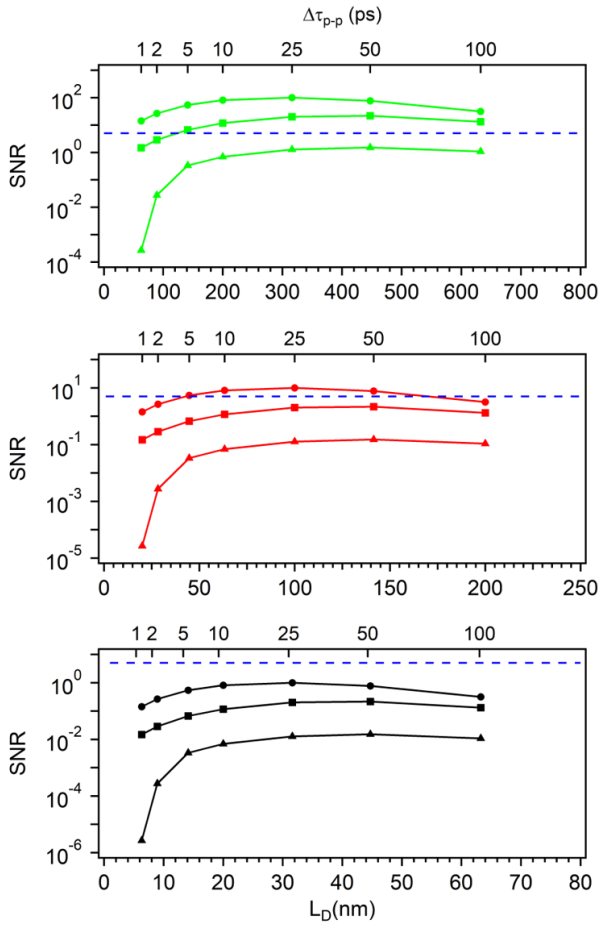

Figure 6.4. Differential signal SNR simulation results. (A, B, C) The SNR of the differential signal is plotted as a function of diffusion length on the bottom axis and $\Delta\tau_{p-p}$ on the top axis. The triangle, square, and circle traces in each individual panel represent the initial $[L \cdot G]_1$ SNRs of 10:1, 100:1, and 1000:1, respectively. The excited state diffusivity is varied in each panel as (A) D_c = 10 cm^2/s, (B) D_c = 1.0 cm^2/s, and (C) D_c = 0.1 cm^2/s. The blue dashed line in each panel denotes the assumed minimal resolvable SNR of 5:1.

The results of the simulation presented in Fig. 6.4 show that the experimental viability of DDPPM is intrinsically coupled to the SNR threshold and the temporal resolution of the optical system. Given the rates of diffusion in panels A, B, and C, the average diffusion length of an excited state is 10 nm at delay times of 0.025 ps, 0.25 ps, and 2.5 ps, respectively. Only in the case of panel A, where carrier diffusivity is 10 cm^2/s, does the differential signal rise above the SNR threshold (5:1), which is denoted by the blue dashed lines in all panels. When the carrier diffusivity is decreased to 1 cm^2/s as shown in panel B, the differential signal fails to rise above the SNR threshold unless the initial amplitude of the transient response SNR is raised to 1000:1, an experimentally unlikely level. Panel C shows that in the case of still lower carrier diffusivity (0.1 cm^2/s), the differential signal amplitude falls 2-5 orders of magnitude below the SNR threshold.

The results of this modeling indicate several avenues that can be pursued to enable detection of sub-10 nm excited state diffusion lengths. Primarily, increasing the SNR of the current instrumentation would enable the application of DDPPM to the measurement of sub-10 nm diffusive motion. Reducing the noise level of the instrumentation may be achieved through modified detection techniques or by implementing more complex pulse modulation schemes [154]. Second, increasing the temporal resolution of the current experimental design will also allow for detection of increasingly shorter diffusion lengths. While the pulse width of the current instrumentation is ~100 fs, it is possible to utilize pulse compression techniques to obtain pulse widths of ~10 fs [155]. The combination of these two experimental modifications may push the capabilities of DDPPM past the SNR restrictions described above.

6.4 Conclusion

The results reported in this chapter demonstrate that DDPPM can detect diffusive motion of photoexcited species in semiconducting materials with improved accuracy and sensitivity compared to traditional PPM. However, the results of simulations suggest that the differential signal amplitudes of DDPPM are below the resolvable detection limit in the case of sub-10 nm diffusive motion. Still, the technique shows promise toward the detection of excited state diffusivity well below the diffraction limit of light. Further development of DDPPM promises to yield a novel material characterization technique that uncovers photophysical properties of disordered semiconducting materials, photocatalytic thin films, and nanoscale optoelectronic devices previously hidden by ensemble averaging in bulk spectroscopic characterization methods.

6.5 Acknowledgements

This work was funded by the Division of Chemical Sciences, Geosciences, and Biosciences, Office of Basic Energy Sciences of the U.S. Department of Energy through Grant DE-SC0014128.

CHAPTER SEVEN

CONCLUSIONS AND FUTURE DIRECTIONS

7.1 Summary

The common goal throughout this dissertation is to provide accurate understanding of, and to develop novel spectroscopic techniques to study the photophysics of heterogenous materials. Chapters 2-4 provide a detailed description of the experimental and theoretical efforts toward the development of novel spectroscopic techniques that are uniquely able to both surpass the diffraction limit and obtain time resolved spectroscopic data from a sub-diffraction limited volume of the material. SPPM and LF-SSEM represent feasible methods for surpassing the diffraction limit of light by a factor of two (~100 nm, SPPM) and theoretically as much as seven-fold (~ 30 nm, LF-SSEM). Similarly, chapter 6 demonstrates the development and effectiveness of a novel technique (DDPPM) that has the potential to measure excited state diffusion lengths below ~10 nm with increased sensitivity compared to PPM. The combination of SPPM, LF-SSEM, and DDPPM shows the capability of utilizing far-field optical techniques to characterize both the spatial evolution of carriers with sub diffraction limited sensitivity and the relaxation dynamics of excited states from sub diffraction limited volumes.

Chapter 5 focuses on the material characterization of PCDTBT, which constitutes the active layer of many high efficiency OPVs and other organic optoelectronic devices. The microscale exciton diffusivity reported in this thesis of 0.55 cm^2/s (in amorphous thin films) changes the fundamental understanding of exciton diffusion in OSPs. Further, the

demonstration of polymer chain alignment to increase exciton diffusivity to ~3.2 cm^2/s and the development of a coarse grain MC simulation serve to disentangle the effects of photophysical parameters in OSP systems. Leveraging the effects of microscale polymer alignment will enable increased exciton transport and dissociation, improving the efficacy of OSPs in nanoscale optoelectronic devices and photovoltaic applications.

In summary, this dissertation, and the resulting publications contribute significantly to the nanoscale research community. Specifically, three spectroscopic techniques have been developed, SPPM, LF-SSEM, and DDPPM, that provide unique characterization methodology to study complex materials systems. Further, the data reported on microscale exciton diffusivity in PCDTBT demonstrates the importance of basic scientific research leading toward improved OSP applications. The remainder of this chapter will describe the opportunities for continuing development of superresolution techniques and the continuing investigation of PCDTBT photophysics.

7.2 Future Directions

7.2.1 High Spatial Resolution Spectroscopic Method Development

SPPM and LF-SSEM represent first iterations of techniques with significant potential for use in nanoscale materials characterization. While fluorescence base superresolution techniques have become highly marketable products, label-free sub-diffraction limit spectroscopic techniques remain comparatively undeveloped. Specific to the further development of SPPM, is the application of a two-dimensionally structured excitation profile. The theoretical modeling of two-dimensional resolution enhancement was discussed in

chapter 3, but these theoretical predictions have yet to be experimentally realized. Further, higher numerical aperture objectives, exploitation of saturated absorption, and higher order nonlinear processes will lead to an even greater increase in experimental spatial resolution.

Similarly, DDPPM shows the potential to produce novel findings related to the mechanisms of excited state transport in disordered materials with relatively slow excited state diffusivity. However, utilization of DDPPM is limited by the signal-to-noise threshold of current optical instrumentation. Therefore, further development of DDPPM will require advanced methods of detection which could include modified pulse modulation schemes or the development of higher sensitivity detection techniques.

7.2.2 Characterization of PCDTBT Devices

PCDTBT is a promising candidate for use in nanoscale optoelectronic devices. Therefore, it is necessary to characterize the carrier mobility in PCDTBT in the presence of an external electric field. Important questions that remain to be answered include if free carriers behave in a similar fashion to excitons across nanometer length scales and the difference between microscale electron and hole mobility in PCDTBT under the presence of an external electric field.

In order to study carrier transport under the influence of an external electric field, it is necessary to develop microscale polymer devices designed with a basic transistor geometry [134]. Figure 7.1 shows an illustration of the transistor geometry where gold contacts act as the source and drain so that an electric field can be driven across a 35 μm channel of polymer thin film. The external electric field applied to the polymer will result

in dissociation of the photoexcited exciton into free carriers. Utilizing PPM, it will be possible to track those carriers using diffraction limited spatial resolution and femtosecond temporal resolution. Therefore, the spatial evolution of both electrons and holes will be observed in counter-propagating directions with respect to the externally applied electric field.

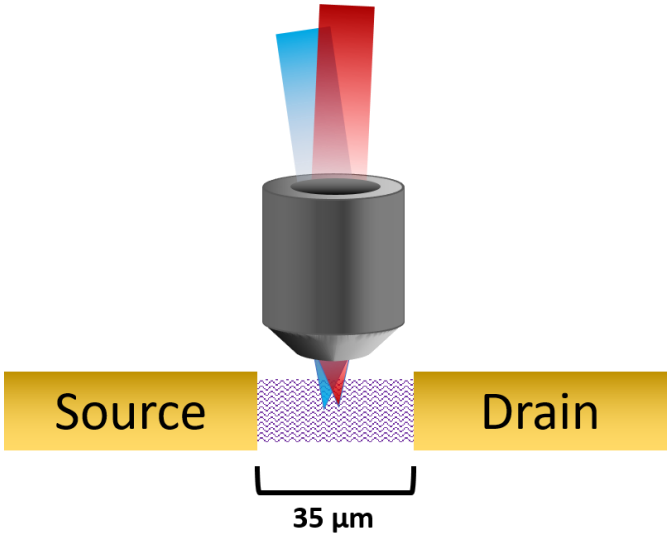

Figure 7.1. Basic geometry of PCDTBT transistor devices. The source and drain are thermally deposited gold, structured using an in house designed shadow mask.

Characterization of PCDTBT in device structures utilizing PPM is a necessary next step in understanding how local heterogeneity influences excited state dynamics of complex polymeric systems. Applying device geometries to the varying film morphologies discussed in chapter 5 will further determine the effects of polymer alignment in nanoscale regions of OSP thin films.

REFERENCES CITED

1. T. Saga, "Advances in crystalline silicon solar cell technology for industrial mass production," NPG Asia Materials **2**, 96-102 (2010).

2. S. B. Darling and F. You, "The case for organic photovoltaics," Royal Society of Chemistry Advances **3**, 17633 (2013).

3. Y. Deng, E. Peng, Y. Shao, Z. Xiao, Q. Dong, and J. Huang, "Scalable fabrication of efficient organolead trihalide perovskite solar cells with doctor-bladed active layers," Energy Environ. Sci. **8**, 1544-1550 (2015).

4. K. Nakata and A. Fujishima, "TiO2 photocatalysis: Design and applications," Journal of Photochemistry and Photobiology C: Photochemistry Reviews **13**, 169-189 (2012).

5. S. Mahajan, "Defects in semiconductors and their effects on devices," Acta Materialia **48**, 137-149 (1999).

6. D. y. Davydova, A. de la Cadena, D. Akimov, and B. Dietzek, "Transient absorption microscopy: advances in chemical imaging of photoinduced dynamics," Laser & Photonics Reviews **10**, 62-81 (2016).

7. E. M. Grumstrup, M. M. Gabriel, E. E. M. Cating, E. M. Van Goethem, and J. M. Papanikolas, "Pump–probe microscopy: Visualization and spectroscopy of ultrafast dynamics at the nanoscale," Chemical Physics **458**, 30-40 (2015).

8. L. Huang and J.-X. Cheng, "Nonlinear Optical Microscopy of Single Nanostructures," Annual Review of Materials Research **43**, 213-236 (2013).

9. T. Ye, D. Fu, and W. S. Warren, "Nonlinear Absorption Microscopy," Photochemistry and Photobiology **85**, 631-645 (2008).

10. E. Massaro and E. Grumstrup, "Label-Free Saturated Structured Excitation Microscopy," Photonics **4**, 36 (2017).

11. W. R. Silva, C. T. Graefe, and R. R. Frontiera, "Toward Label-Free Super-Resolution Microscopy," ACS Photonics **3**, 79-86 (2016).

12. E. S. Massaro, A. H. Hill, C. L. Kennedy, and E. M. Grumstrup, "Imaging theory of structured pump-probe microscopy," Optics Express **24**, 20868 (2016).

13. E. S. Massaro, A. H. Hill, and E. M. Grumstrup, "Super-Resolution Structured Pump–Probe Microscopy," ACS Photonics **3**, 501-506 (2016).

14. P. Wang, M. N. Slipchenko, J. Mitchell, C. Yang, E. O. Potma, X. Xu, and J. X. Cheng, "Far-field Imaging of Non-fluorescent Species with Sub-diffraction Resolution," Nature Photonics **7**, 449-453 (2013).

15. K. M. Hajek, B. Littleton, D. Turk, Timothy J. McIntyre, and H. Rubinsztein-Dunlop, "A method for achieving super-resolved widefield CARS microscopy," Optics Express **18**, 9 (2010).

16. S. B. Penwell, L. D. S. Ginsberg, R. Noriega, and N. S. Ginsberg, "Resolving ultrafast exciton migration in organic solids at the nanoscale," Nat Mater **16**, 1136-1141 (2017).

17. E. Rittweger, K. Y. Han, S. E. Irvine, C. Eggeling, and S. W. Hell, "STED microscopy reveals crystal colour centres with nanometric resolution," Nature Photonics **3**, 144-147 (2009).

18. M. J. Rust, M. Bates, and X. Zhuang, "Sub-diffraction-limit imaging by stochastic optical reconstruction microscopy (STORM)," Nature Methods **3**, 793-795 (2006).

19. E. Betzig, G. H. Patterson, R. Sougrat, O. W. Lindwasser, S. Olenych, J. S. Bonifacino, J. L.-S. Michael W. Davidson, and H. F. Hess, "Imaging Intracellular Fluorescent Proteins at Nanometer Resolution," Science **313**, 1642-1645 (2006).

20. M. G. Gustafsson, "Nonlinear structured-illumination microscopy: wide-field fluorescence imaging with theoretically unlimited resolution," Proceedings of the National Acadademy of Science U S A **102**, 13081-13086 (2005).

21. R. Heintzmann, "Saturated patterned excitation microscopy with two-dimensional excitation patterns," Micron **34**, 283-291 (2003).

22. R. Heintzmann and C. Cremer, "Laterally Modulated Excitation Microscopy-Improvement of resolution by using a diffraction grating.," Optical Biopsies and Microscopic Techniques III **3568**, 185-196 (1999).

23. M. A. Green, Y. Hishikawa, W. Warta, E. D. Dunlop, D. H. Levi, J. Hohl-Ebinger, and A. W. H. Ho-Baillie, "Solar cell efficiency tables (version 50)," Progress in Photovoltaics: Research and Applications **25**, 668-676 (2017).

24. A. Polman, M. Knight, E. C. Garnett, B. Ehrler, and W. C. Sinke, "Photovoltaic materials: Present efficiencies and future challenges," Science **352**, aad4424 (2016).

25. Y. Zhang, E. Bovill, J. Kingsley, A. R. Buckley, H. Yi, A. Iraqi, T. Wang, and D. G. Lidzey, "PCDTBT based solar cells: one year of operation under real-world conditions," Scientific Reports **6**, 21632 (2016).

26. F. Lombeck, D. Di, L. Yang, L. Meraldi, S. Athanasopoulos, D. Credgington, M. Sommer, and R. H. Friend, "PCDTBT: From Polymer Photovoltaics to Light-Emitting Diodes by Side-Chain-Controlled Luminescence," Macromolecules **49**, 9382-9387 (2016).

27. S. Beaupré and M. Leclerc, "PCDTBT: en route for low cost plastic solar cells," Journal of Materials Chemistry A **1**, 11097 (2013).

28. H. K. H. Lee, Z. Li, J. R. Durrant, and W. C. Tsoi, "Is organic photovoltaics promising for indoor applications?," Applied Physics Letters **108**, 253301 (2016).

29. A. J. Heeger, "25th anniversary article: Bulk heterojunction solar cells: understanding the mechanism of operation," Advanced Materials **26**, 10-27 (2014).

30. S. Mukamel, *Principles of nonlinear optical spectroscopy*, Oxford series in optical and imaging sciences (Oxford University Press, New York, 1995), pp. xviii, 543 p.

31. G. Grancini, D. Polli, D. Fazzi, J. Cabanillas-Gonzalez, G. Cerullo, and G. Lanzani, "Transient Absorption Imaging of P3HT:PCBM Photovoltaic Blend: Evidence For Interfacial Charge Transfer State," The Journal of Physical Chemistry Letters **2**, 1099-1105 (2011).

32. P.-T. Dong and J.-X. Cheng, "Pump–Probe Microscopy: Theory, Instrumentation, and Applications," Spectroscopy Online **32**(2017).

33. O. V. Mikhnenko, P. W. M. Blom, and T.-Q. Nguyen, "Exciton diffusion in organic semiconductors," Energy Environ. Sci. **8**, 1867-1888 (2015).

34. E. M. Grumstrup, M. M. Gabriel, E. M. Cating, C. W. Pinion, J. D. Christesen, J. R. Kirschbrown, E. L. Vallorz, J. F. Cahoon, and J. M. Papanikolas, "Ultrafast Carrier Dynamics in Individual Silicon Nanowires: Characterization of Diameter-Dependent Carrier Lifetime and Surface Recombination with Pump–Probe Microscopy," The Journal of Physical Chemistry C **118**, 8634-8640 (2014).

35. R. Wang, B. A. Ruzicka, N. Kumar, M. Z. Bellus, H.-Y. Chiu, and H. Zhao, "Ultrafast and spatially resolved studies of charge carriers in atomically thin molybdenum disulfide," Physical Review B **86**(2012).

36. E. M. Grumstrup, M. M. Gabriel, C. W. Pinion, J. K. Parker, J. F. Cahoon, and J. M. Papanikolas, "Reversible strain-induced electron-hole recombination in silicon nanowires observed with femtosecond pump-probe microscopy," Nano Letters **14**, 6287-6292 (2014).

37. H. Köhler, "On Abbe's Theory of Image Formation in the Microscope," Optica Acta: International Journal of Optics **28**, 1691-1701 (1981).

38. A. J. d. Dekker and A. v. d. Bos, "Resolution: a survey," The Journal of The Optical Society of America A **14**, 547-557 (1997).

39. M. G. L. Gustafsson, D. A. Agard, and J. W. Sedat, "Doubling the lateral resolution of wide-field fluorescence microscopy using structured illumination.," Three-Dimensional and Multidimensional Microscopy: Image Acquisition Processing VII, **3919**, 141-150 (2000).

40. L. Schermelleh, R. Heintzmann, and H. Leonhardt, "A guide to super-resolution fluorescence microscopy," The Journal of Cell Biology **190**, 165-175 (2010).

41. R. F. Laine, G. S. Kaminski Schierle, S. van de Linde, and C. F. Kaminski, "From single-molecule spectroscopy to super-resolution imaging of the neuron: a review," Methods Appl Fluoresc **4**, 022004 (2016).

42. S. Cho, J. H. Seo, S. H. Park, S. Beaupre, M. Leclerc, and A. J. Heeger, "A thermally stable semiconducting polymer," Materials Views **22**, 1253-1257 (2010).

43. N. A. Cooling, E. F. Barnes, F. Almyahi, K. Feron, M. F. Al-Mudhaffer, A. Al-Ahmad, B. Vaughan, T. R. Andersen, M. J. Griffith, A. S. Hart, A. G. Lyons, W. J. Belcher, and P. C. Dastoor, "A low-cost mixed fullerene acceptor blend for printed electronics," Journal of Materials Chemistry A **4**, 10274-10281 (2016).

44. Heliatek, "Heliatek sets new Organic Photovoltaic world record efficiency of 13.2%," (2016).

45. G. D. Scholes and G. Rumbles, "Excitons in nanoscale systems," Nature Materials **5**, 683-696 (2006).

46. O. G. Reid, R. D. Pensack, Y. Song, G. D. Scholes, and G. Rumbles, "Charge Photogeneration in Neat Conjugated Polymers," Chemistry of Materials **26**, 561-575 (2014).

47. K. J. T. Hamam, "Organic Solar Cells Based on High Dielectric Constant Materials: An Approach to Increase Efficiency," (Western Michigan University, 2013).

48. B. A. Ruzicka, L. K. Werake, H. Samassekou, and H. Zhao, "Ambipolar diffusion of photoexcited carriers in bulk GaAs," Applied Physics Letters **97**, 262119 (2010).

49. M. M. Gabriel, J. R. Kirschbrown, J. D. Christesen, C. W. Pinion, D. F. Zigler, E. M. Grumstrup, B. P. Mehl, E. E. Cating, J. F. Cahoon, and J. M. Papanikolas, "Direct imaging of free carrier and trap carrier motion in silicon nanowires by

spatially-separated femtosecond pump-probe microscopy," Nano Lett **13**, 1336-1340 (2013).

50. X.-Y. Zhu, Q. Yang, and M. Muntwiler, "Charge-Transfer Excitons at Organic Semiconductor Surfaces and Interfaces," Accounts of Chemical Research **42**, 1779-1787 (2008).

51. L. E. Brus, "A simple model for the ionization potential, electron affinity, and aqueous redox potentials of small semiconductor crystallites," The Journal of Chemical Physics **79**, 5566 (1983).

52. Y. Lin, X. Ling, L. Yu, S. Huang, A. L. Hsu, Y. H. Lee, J. Kong, M. S. Dresselhaus, and T. Palacios, "Dielectric screening of excitons and trions in single-layer MoS2," Nano Lett **14**, 5569-5576 (2014).

53. N. S. Sariciftci, L. Smilowitz, A. J. Heeger, and F. Wudl, "Photoinduced Electron Transfer from a Conducting Polymer to Buckminsterfullerene," Science **258**, 1474-1476 (1992).

54. H. Benten, D. Mori, H. Ohkita, and S. Ito, "Recent research progress of polymer donor/polymer acceptor blend solar cells," Journal of Materials Chemistry A **4**, 5340-5365 (2016).

55. N. Banerji, S. Cowan, M. Leclerc, E. Vauthey, and A. J. Heeger, "Exciton Formation, Relaxation, and Decay in PCDTBT," Journal of the America Chemical Society **132**, 17459-17470 (2010).

56. M. Tong, N. E. Coates, D. Moses, A. J. Heeger, S. Beaupré, and M. Leclerc, "Charge carrier photogeneration and decay dynamics in the poly(2,7-carbazole) copolymer PCDTBT and in bulk heterojunction composites with PC70BM," Physical Review B **81**(2010).

57. B. 5Shao and D. A. Vanden Bout, "Probing the molecular weight dependent intramolecular interactions in single molecules of PCDTBT," J. Mater. Chem. C **5**, 9786-9791 (2017).

58. L. Pandey, C. Risko, J. E. Norton, and J.-L. Brédas, "Donor–Acceptor Copolymers of Relevance for Organic Photovoltaics: A Theoretical Investigation

of the Impact of Chemical Structure Modifications on the Electronic and Optical Properties," Macromolecules **45**, 6405-6414 (2012).

59. B. Gieseking, B. Jaeck, E. Preis, S. Jung, M. Forster, U. Scherf, C. Deibel, and V. Dyakonov, "Excitation Dynamics in Low Band Gap Donor–Acceptor Copolymers and Blends," Advanced Energy Materials **2**, 1477-1482 (2012).

60. G. Li, R. Zhu, and Y. Yang, "Polymer solar cells," Nature Photonics **6**, 153-161 (2012).

61. N. Banerji, S. Cowan, E. Vauthey, and A. J. Heeger, "Ultrafast Relaxation of the Poly(3-hexylthiophene) Emission Spectrum," The Journal of Physical Chemistry C **115**, 9726-9739 (2011).

62. Y. Xiao, H. Wang, S. Zhou, K. Yan, W. Xie, Z. Guan, S.-W. Tsang, and J.-B. Xu, "Efficient ternary bulk heterojunction solar cells with PCDTBT as hole-cascade material," Nano Energy **19**, 476-485 (2016).

63. M. A. van Dijk, M. Lippitz, and M. Orrit, "Detection of Acoustic Oscillations of Single Gold Nanospheres by Time-Resolved Interferometry," Physical Review Letters **95**(2005).

64. H. Staleva and G. V. Hartland, "Vibrational Dynamics of Silver Nanocubes and Nanowires Studied by Single-Particle Transient Absorption Spectroscopy," Advanced Functional Materials **18**, 3809-3817 (2008).

65. B. P. Mehl, J. R. Kirschbrown, R. L. House, and J. M. Papanikolas, "The End Is Different than The Middle: Spatially Dependent Dynamics in ZnO Rods Observed by Femtosecond Pump–Probe Microscopy," The Journal of Physical Chemistry Letters **2**, 1777-1781 (2011).

66. M. A. Seo, J. Yoo, S. A. Dayeh, S. T. Picraux, A. J. Taylor, and R. P. Prasankumar, "Mapping carrier diffusion in single silicon core-shell nanowires with ultrafast optical microscopy," Nano Lett **12**, 6334-6338 (2012).

67. M. M. Gabriel, E. M. Grumstrup, J. R. Kirschbrown, C. W. Pinion, J. D. Christesen, D. F. Zigler, E. E. Cating, J. F. Cahoon, and J. M. Papanikolas,

"Imaging charge separation and carrier recombination in nanowire p-i-n junctions using ultrafast microscopy," Nano Lett **14**, 3079-3087 (2014).

68. S. S. Lo, H. Y. Shi, L. Huang, and G. V. Hartland, "Imaging the extent of plasmon excitation in Au nanowires using pump-probe microscopy," Optics Letters **38**, 1265-1267 (2013).

69. C. T. O. Wong, S. S. Lo, and L. Huang, "Ultrafast Spatial Imaging of Charge Dynamics in Heterogeneous Polymer Blends," The Journal of Physical Chemistry Letters **3**, 879-884 (2012).

70. G. Grancini, M. Maiuri, D. Fazzi, A. Petrozza, H. J. Egelhaaf, D. Brida, G. Cerullo, and G. Lanzani, "Hot exciton dissociation in polymer solar cells," Nature Materials **12**, 29-33 (2012).

71. C. Y. Wong, S. B. Penwell, B. L. Cotts, R. Noriega, H. Wu, and N. S. Ginsberg, "Revealing Exciton Dynamics in a Small-Molecule Organic Semiconducting Film with Subdomain Transient Absorption Microscopy," The Journal of Physical Chemistry C **117**, 22111-22122 (2013).

72. C. Y. Wong, B. L. Cotts, H. Wu, and N. S. Ginsberg, "Exciton dynamics reveal aggregates with intermolecular order at hidden interfaces in solution-cast organic semiconducting films," Nat Commun **6**, 5946 (2015).

73. S. W. Hell and J. Wichmann, "Breaking the diffraction resolution limit by stimulated emission- stimulated-emission-depletion fluorescence microscopy.," Optics Letters **19**, 780-782 (1994).

74. D. Wildanger, R. Medda, L. Kastrup, and S. W. Hell, "A compact STED microscope providing 3D nanoscale resolution," J Microsc **236**, 35-43 (2009).

75. R. Heintzmann and C. Cremer, "Laterally Modulated Excitation Microscopy-Improvement of resolution by using a diffraction grating.," Optical Biopsies and Microscopic Techniques III, 185-196 (1999).

76. M. G. L. Gustafsson, D. A. Agard, and J. W. Sedat, "Doubling the lateral resolution of wide-field fluorescence microscopy using structured illumination.,"

Three-Dimensional and Multidimensional Microscopy: Image Acquisition Processing VII, , 141-150 (2000).

77. B. Littleton, K. Lai, D. Longstaff, V. Sarafis, P. Munroe, N. Heckenberg, and H. Rubinsztein-Dunlop, "Coherent super-resolution microscopy via laterally structured illumination," Micron **38**, 150-157 (2007).

78. M. J. Rust, M. Bates, and X. Zhuang, "Sub-diffraction-limit imaging by stochastic optical reconstruction microscopy (STORM)," Nat Methods **3**, 793-795 (2006).

79. R. F. Egerton, *Physical principles of electron microscopy : an introduction to TEM, SEM, and AEM* (Springer, New York, NY, 2005), pp. xii, 202 p.

80. A. Engel and D. J. Müller, "Observing single biomolecules at work with the atomic force microscope," Nature Structural Biology **7**, 715-718 (2000).

81. H. A. Bechtel, E. A. Muller, R. L. Olmon, M. C. Martin, and M. B. Raschke, "Ultrabroadband infrared nanospectroscopic imaging," Proc Natl Acad Sci U S A **111**, 7191-7196 (2014).

82. E. A. Muller, B. Pollard, and M. B. Raschke, "Infrared Chemical Nano-Imaging: Accessing Structure, Coupling, and Dynamics on Molecular Length Scales," J Phys Chem Lett **6**, 1275-1284 (2015).

83. E. S. Barnard, E. T. Hoke, S. T. Connor, J. R. Groves, T. Kuykendall, Z. Yan, E. C. Samulon, E. D. Bourret-Courchesne, S. Aloni, P. J. Schuck, C. H. Peters, and B. E. Hardin, "Probing carrier lifetimes in photovoltaic materials using subsurface two-photon microscopy," Sci Rep **3**, 2098 (2013).

84. P. Wang, M. N. Slipchenko, J. Mitchell, C. Yang, E. O. Potma, X. Xu, and J. X. Cheng, "Far-field Imaging of Non-fluorescent Species with Sub-diffraction Resolution," Nat Photonics **7**, 449-453 (2013).

85. N. Liu, M. Kumbham, I. Pita, Y. Guo, P. Bianchini, A. Diaspro, S. A. M. Tofail, A. Peremans, and C. Silien, "Far-Field Subdiffraction Imaging of Semiconductors Using Nonlinear Transient Absorption Differential Microscopy," ACS Photonics (2016).

86. J. H. Park, S. W. Lee, E. S. Lee, and J. Y. Lee, "A method for super-resolved CARS microscopy with structured illumination in two dimensions," Optics Express **22**, 9854-9870 (2014).

87. E. M. Grumstrup, E. M. Cating, M. M. Gabriel, C. W. Pinion, J. D. Christesen, J. R. Kirschbrown, E. L. Vallorz, J. F. Cahoon, and J. M. Papanikolas, "Ultrafast Carrier Dynamics of Silicon Nanowire Ensembles: The Impact of Geometrical Heterogeneity on Charge Carrier Lifetime," The Journal of Physical Chemistry C **118**, 8626-8633 (2014).

88. F. d. Lange, A. Cambi, R. Huijbens, B. d. Bakker, W. Rensen, M. Garcia-Parajo, N. v. Hulst, and C. G. Figdor, "Cell biology beyond the diffraction limit- near-field scanning optical microscopy," Journal of Cell Science **114**, 4153-4160 (2001).

89. A. Jost and R. Heintzmann, "Superresolution Multidimensional Imaging with Structured Illumination Microscopy," Annual Review of Materials Research **43**, 261-282 (2013).

90. E. A. Muller, B. Pollard, and M. B. Raschke, "Infrared Chemical Nano-Imaging: Accessing Structure, Coupling, and Dynamics on Molecular Length Scales," The Journal of Physical Chemistry Letters **6**, 1275-1284 (2015).

91. H. A. Bechtel, E. A. Muller, R. L. Olmon, M. C. Martin, and M. B. Raschke, "Ultrabroadband infrared nanospectroscopic imaging," Proceedings of the National Acadademy of Science U S A **111**, 7191-7196 (2014).

92. C.-Y. Chung, J. Hsu, S. Mukamel, and E. O. Potma, "Controlling stimulated coherent spectroscopy and microscopy by a position-dependent phase," Physical Review A **87**(2013).

93. J. Goodman, *Introduction to Fourier Optics* (Roberts and Company, Greenwood Village, CO, 2004), Vol. 1.

94. M. Gu, *Advanced optical imaging theory*, Springer series in optical sciences, (Springer, Berlin ; Heidelberg, 2000), pp. xii, 214 s.

95. Q. Zafar and K. Sulaiman, "Utility of PCDTBT polymer for the superior sensing parameters of electrical response based relative humidity sensor," Reactive and Functional Polymers **105**, 45-51 (2016).

96. A. Armin, G. Juska, M. Ullah, M. Velusamy, P. L. Burn, P. Meredith, and A. Pivrikas, "Balanced Carrier Mobilities: Not a Necessary Condition for High-Efficiency Thin Organic Solar Cells as Determined by MIS-CELIV," Advanced Energy Materials **4**, 1300954 (2014).

97. J. R. Hauser, "Extraction of Experimental Mobility Data for MOS Llevices," IEEE Transactions on Electron Devices **43**, 1981-1988 (1996).

98. S. H. Park, A. Roy, S. Beaupré, S. Cho, N. Coates, J. S. Moon, D. Moses, M. Leclerc, K. Lee, and A. J. Heeger, "Bulk heterojunction solar cells with internal quantum efficiency approaching 100%," Nature Photonics **3**, 297-302 (2009).

99. Y. Yamashita, F. Hinkel, T. Marszalek, W. Zajaczkowski, W. Pisula, M. Baumgarten, H. Matsui, K. Müllen, and J. Takeya, "Mobility Exceeding 10 cm2/(V·s) in Donor–Acceptor Polymer Transistors with Band-like Charge Transport," Chemistry of Materials **28**, 420-424 (2016).

100. B. H. Lee, B. B. Y. Hsu, C. Luo, M. Wang, G. C. Bazan, and A. J. Heeger, "Semiconducting Polymers with Mobility Approaching One Hundred Square Centimeters Per Volt Per Second," (2017).

101. J. Li, Y. Zhao, H. S. Tan, Y. Guo, C. A. Di, G. Yu, Y. Liu, M. Lin, S. H. Lim, Y. Zhou, H. Su, and B. S. Ong, "A stable solution-processed polymer semiconductor with record high-mobility for printed transistors," Scientific Reports **2**, 754 (2012).

102. C. Guo, Y. H. Lin, M. D. Witman, K. A. Smith, C. Wang, A. Hexemer, J. Strzalka, E. D. Gomez, and R. Verduzco, "Conjugated block copolymer photovoltaics with near 3% efficiency through microphase separation," Nano Letters **13**, 2957-2963 (2013).

103. F. Lombeck, A. Sepe, R. Thomann, R. H. Friend, and M. Sommer, "Compatibilization of All-Conjugated Polymer Blends for Organic Photovoltaics," ACS Nano **10**, 8087-8096 (2016).

104. W. R. Mateker, I. T. Sachs-Quintana, G. F. Burkhard, R. Cheacharoen, and M. D. McGehee, "Minimal Long-Term Intrinsic Degradation Observed in a Polymer Solar Cell Illuminated in an Oxygen-Free Environment," Chemistry of Materials **27**, 404-407 (2015).

105. A. Melianas, F. Etzold, T. J. Savenije, F. Laquai, O. Inganas, and M. Kemerink, "Photo-generated carriers lose energy during extraction from polymer-fullerene solar cells," Nat Commun **6**, 8778 (2015).

106. A. Melianas, V. Pranculis, Y. Xia, N. Felekidis, O. Inganäs, V. Gulbinas, and M. Kemerink, "Photogenerated Carrier Mobility Significantly Exceeds Injected Carrier Mobility in Organic Solar Cells," Advanced Energy Materials **7**, 1602143 (2017).

107. M. Bednarz, J. Lapin, R. McGillicuddy, K. M. Pelzer, G. S. Engel, and G. B. Griffin, "Modeling Ultrafast Exciton Migration within the Electron Donor Domains of Bulk Heterojunction Organic Photovoltaics," The Journal of Physical Chemistry C **121**, 5467-5479 (2017).

108. T. Zhu, Y. Wan, and L. Huang, "Direct Imaging of Frenkel Exciton Transport by Ultrafast Microscopy," Accounts of Chemical Research (2017).

109. R. Binder, D. Lauvergnat, and I. Burghardt, "Conformational Dynamics Guides Coherent Exciton Migration in Conjugated Polymer Materials: A First-Principles Quantum Dynamical Study," arXiv.org (2017).

110. H. R. Tseng, L. Ying, B. B. Hsu, L. A. Perez, C. J. Takacs, G. C. Bazan, and A. J. Heeger, "High Mobility Field Effect Transistors Based on Macroscopically Oriented Regioregular Copolymers," Nano Letters **12**, 6353-6357 (2012).

111. H. R. Tseng, H. Phan, C. Luo, M. Wang, L. A. Perez, S. N. Patel, L. Ying, E. J. Kramer, T. Q. Nguyen, G. C. Bazan, and A. J. Heeger, "High-mobility field-effect transistors fabricated with macroscopic aligned semiconducting polymers," Advanced Materials **26**, 2993-2998 (2014).

112. X.-H. Jin, M. B. Price, J. R. Finnegan, C. E. Boott, J. M. Richter, A. Rao, S. M. Menke, R. H. Friend, G. R.Whittell, and I. Manners, "Long-range exciton transport in conjugated polymer nanofibers prepared by seeded growth," Science **360**, 897-900 (2018).

113. A. J. Ward, A. Ruseckas, and I. D. W. Samuel, "A Shift from Diffusion Assisted to Energy Transfer Controlled Fluorescence Quenching in Polymer–Fullerene Photovoltaic Blends," The Journal of Physical Chemistry C **116**, 23931-23937 (2012).

114. T. Biskup, M. Sommer, S. Rein, D. L. Meyer, M. Kohlstadt, U. Wurfel, and S. Weber, "Ordering of PCDTBT revealed by time-resolved electron paramagnetic resonance spectroscopy of its triplet excitons," Angew Chemie International Edition in English **54**, 7707-7710 (2015).

115. Y. Olivier, D. Niedzialek, V. Lemaur, W. Pisula, K. Mullen, U. Koldemir, J. R. Reynolds, R. Lazzaroni, J. Cornil, and D. Beljonne, "25th anniversary article: high-mobility hole and electron transport conjugated polymers: how structure defines function," Advanced Materials **26**, 2119-2136 (2014).

116. F. Etzold, I. A. Howard, R. Mauer, M. Meister, T. D. Kim, K. S. Lee, N. S. Baek, and F. Laquai, "Ultrafast exciton dissociation followed by nongeminate charge recombination in PCDTBT:PCBM photovoltaic blends," Journal of the America Chemical Society **133**, 9469-9479 (2011).

117. A. H. Hill, K. E. Smyser, C. L. Kennedy, E. S. Massaro, and E. M. Grumstrup, "Screened Charge Carrier Transport in Methylammonium Lead Iodide Perovskite Thin Films," The Journal of Physical Chemistry Letters **8**, 948-953 (2017).

118. C. L. Kennedy, A. H. Hill, E. S. Massaro, and E. M. Grumstrup, "Ultrafast Excited-State Transport and Decay Dynamics in Cesium Lead Mixed Halide Perovskites," ACS Energy Letters, 1501-1506 (2017).

119. N. Persson, M. McBride, M. Grover, and E. Reichmanis, "Silicon Valley meets the ivory tower: Searchable data repositories for experimental nanomaterials research," Current Opinion in Solid State and Materials Science **20**, 338-343 (2016).

120. C. Zhou, Y. Liang, F. Liu, C. Sun, X. Huang, Z. Xie, F. Huang, J. Roncali, T. P. Russell, and Y. Cao, "Chain Length Dependence of the Photovoltaic Properties of Monodisperse Donor-Acceptor Oligomers as Model Compounds of Polydisperse Low Band Gap Polymers," Advanced Functional Materials **24**, 7538-7547 (2014).

121. P. Carbone and A. Troisi, "Charge Diffusion in Semiconducting Polymers: Analytical Relation between Polymer Rigidity and Time Scales for Intrachain and Interchain Hopping," J Phys Chem Lett **5**, 2637-2641 (2014).

122. I. Hwang and G. D. Scholes, "Electronic Energy Transfer and Quantum-Coherence in π-Conjugated Polymers†," Chemistry of Materials **23**, 610-620 (2011).

123. J. E. Northrup, "Mobility enhancement in polymer organic semiconductors arising from increased interconnectivity at the level of polymer segments," Applied Physics Letters **106**(2015).

124. D. Venkateshvaran, M. Nikolka, A. Sadhanala, V. Lemaur, M. Zelazny, M. Kepa, M. Hurhangee, A. J. Kronemeijer, V. Pecunia, I. Nasrallah, I. Romanov, K. Broch, I. McCulloch, D. Emin, Y. Olivier, J. Cornil, D. Beljonne, and H. Sirringhaus, "Approaching disorder-free transport in high-mobility conjugated polymers," Nature **515**, 384-388 (2014).

125. Y.-K. Lan and C.-I. Huang, "Charge Mobility and Transport Behavior in the Ordered and Disordered States of the Regioregular Poly(3-hexylthiophene)," The Journal of Physical Chemistry B **113**, 14555-14564 (2009).

126. R. J. O. M. Hoofman, Matthijs P. de Haas, L. D. A. Siebbeles, and J. M.Warman, "Highly mobile electrons and holes on isolated chains of the semiconducting polymer poly(phenylene vinylene)," Nature **392**, 54-56 (1998).

127. A. Kaewprajak, P. Kumnorkaew, and T. Sagawa, "Improvement of photovoltaic performance of polymer and fullerene based bulk heterojunction solar cells prepared by the combination of directional solidification and convective deposition techniques," Organic Electronics **56**, 16-26 (2018).

128. Z. Yang, M. Moffa, Y. Liu, H. Li, L. Persano, A. Camposeo, R. Saija, M. A. Iatì, O. M. Maragò, D. Pisignano, C.-Y. Nam, E. Zussman, and M. Rafailovich, "Electrospun Conjugated Polymer/Fullerene Hybrid Fibers: Photoactive Blends, Conductivity through Tunneling-AFM, Light Scattering, and Perspective for Their Use in Bulk-Heterojunction Organic Solar Cells," The Journal of Physical Chemistry C (2018).

129. P. E. Shaw, A. Ruseckas, and I. D. W. Samuel, "Exciton Diffusion Measurements in Poly(3-hexylthiophene)," Advanced Materials **20**, 3516-3520 (2008).

130. Y. Yasutani, A. Saeki, T. Fukumatsu, Y. Koizumi, and S. Seki, "Unprecedented High Local Charge-carrier Mobility in P3HT Revealed by Direct and Alternating Current Methods," Chemistry Letters **42**, 19-21 (2013).

131. S. A. Mollinger, B. A. Krajina, R. Noriega, A. Salleo, and A. J. Spakowitz, "Percolation, Tie-Molecules, and the Microstructural Determinants of Charge Transport in Semicrystalline Conjugated Polymers," ACS Macro Letters, 708-712 (2015).

132. C. Matt, D. L. Meyer, F. Lombeck, M. Sommer, and T. Biskup, "TBT Entirely Dominates the Electronic Structure of the Conjugated Copolymer PCDTBT: Insights from Time-Resolved Electron Paramagnetic Resonance Spectroscopy," Macromolecules **51**, 4341-4349 (2018).

133. T. M. Burke and M. D. McGehee, "How high local charge carrier mobility and an energy cascade in a three-phase bulk heterojunction enable >90% quantum efficiency," Materials Views **26**, 1923-1928 (2014).

134. Z. Ahmad, S. M. Abdullah, D. Taguchi, K. Sulaiman, T. Manaka, and M. Iwamoto, "Investigation of carrier transit motion in PCDTBT by optical SHG technique," Laser Physics **24**, 105701 (2014).

135. T. M. Clarke, J. Peet, A. Nattestad, N. Drolet, G. Dennler, C. Lungenschmied, M. Leclerc, and A. J. Mozer, "Charge carrier mobility, bimolecular recombination and trapping in polycarbazole copolymer:fullerene (PCDTBT:PCBM) bulk heterojunction solar cells," Organic Electronics **13**, 2639-2646 (2012).

136. G. D. Scholes, "Long-range resonance energy transfer in molecular systems," Annu Rev Phys Chem **54**, 57-87 (2003).

137. K. Feron, W. J. Belcher, C. J. Fell, and P. C. Dastoor, "Organic solar cells: understanding the role of Forster resonance energy transfer," Int J Mol Sci **13**, 17019-17047 (2012).

138. S. Westenhoff, C. Daniel, R. H. Friend, C. Silva, V. Sundstrom, and A. Yartsev, "Exciton migration in a polythiophene: probing the spatial and energy domain by line-dipole Forster-type energy transfer," J Chem Phys **122**, 094903 (2005).

139. Y. R. Khan, T. E. Dykstra, and G. D. Scholes, "Exploring the Förster limit in a small FRET pair," Chemical Physics Letters **461**, 305-309 (2008).

140. V. Gupta, V. Bharti, M. Kumar, S. Chand, and A. J. Heeger, "Polymer-Polymer Forster Resonance Energy Transfer Significantly Boosts the Power Conversion Efficiency of Bulk-Heterojunction Solar Cells," Adv Mater (2015).

141. A. A. B. Alghamdi, D. C. Watters, H. Yi, S. Al-Faifi, M. S. Almeataq, D. Coles, J. Kingsley, D. G. Lidzey, and A. Iraqi, "Selenophene vs. thiophene in benzothiadiazole-based low energy gap donor–acceptor polymers for photovoltaic applications," Journal of Materials Chemistry A **1**, 5165 (2013).

142. I. A. Howard, F. Etzold, F. Laquai, and M. Kemerink, "Nonequilibrium Charge Dynamics in Organic Solar Cells," Advanced Energy Materials **4**, 1301743 (2014).

143. S. Athanasopoulos, E. V. Emelianova, A. B. Walker, and D. Beljonne, "Exciton diffusion in energetically disordered organic materials," Physical Review B **80**(2009).

144. S. Dimitrov, B. Schroeder, C. Nielsen, H. Bronstein, Z. Fei, I. McCulloch, M. Heeney, and J. Durrant, "Singlet Exciton Lifetimes in Conjugated Polymer Films for Organic Solar Cells," Polymers **8**, 14 (2016).

145. X. Lu, H. Hlaing, D. S. Germack, J. Peet, W. H. Jo, D. Andrienko, K. Kremer, and B. M. Ocko, "Bilayer order in a polycarbazole-conjugated polymer," Nat Commun **3**, 795 (2012).

146. D. Wang, K. Nakajima, F. Liu, S. Shi, and T. P. Russell, "Nanomechanical Imaging of the Diffusion of Fullerene into Conjugated Polymer," ACS Nano (2017).

147. A. J. Clulow, E. P. Gilbert, P. Wolfer, P. L. Burn, and I. R. Gentle, "Clustering of High Molecular Weight PCDTBT in Bulk-Heterojunction Casting Solutions," Macromolecules **48**, 8331-8336 (2015).

148. M. Kac, "Random Walk and the Theory of Browninan Motion," The American Mathematical Monthly **54**, 369-391 (1947).

149. S. M. Menke, W. A. Luhman, and R. J. Holmes, "Tailored exciton diffusion in organic photovoltaic cells for enhanced power conversion efficiency," Nat Mater **12**, 152-157 (2013).

150. C. Adán, J. Marugán, E. Sánchez, C. Pablos, and R. van Grieken, "Understanding the effect of morphology on the photocatalytic activity of TiO 2 nanotube array electrodes," Electrochimica Acta **191**, 521-529 (2016).

151. Y. Tamaki, A. Furube, M. Murai, K. Hara, R. Katoh, and M. Tachiya, "Dynamics of efficient electron-hole separation in TiO2 nanoparticles revealed by femtosecond transient absorption spectroscopy under the weak-excitation condition," Phys Chem Chem Phys **9**, 1453-1460 (2007).

152. S. V. Frolov and Z. V. Vardeny, "Double-modulation electro-optic sampling for pump-and-probe ultrafast correlation measurements," Review of Scientific Instruments **69**, 1257 (1998).

153. S. M. Sze and K. K. Ng, *Physics of semiconductor devices*, 3rd ed. (Wiley-Interscience, Hoboken, N.J., 2007), pp. x, 815 p.

154. M. C. Fischer, J. W. Wilson, F. E. Robles, and W. S. Warren, "Invited Review Article: Pump-probe microscopy," Rev Sci Instrum **87**, 031101 (2016).

155. D. H. Sutter, G. Steinmeyer, L. Gallmann, N. Matuschek, F. Morier-Genoud, and U. Keller, "Semiconductor saturable-absorber mirror–assisted Kerr-lens mode-locked Ti_sapphire laser producing pulses in the two-cycle regime," Optics Letters **24**, 631-633 (1999).